Optical System for High-Speed Atomic Force Microscope

by

Kwang Yong Lim

B.App.Sc., Mechanical Engineering (2002)
University of Toronto

Submitted to the Department of Mechanical Engineering
in partial fulfillment of the requirements for the degree of

Master of Science in Mechanical Engineering

at the

MASSACHUSETTS INSTITUTE OF TECHNOLOGY

June 2010

Author .....
Department of Mechanical Engineering
May 7, 2010

Certified by .....
Kamal Youcef-Toumi
Professor of Mechanical Engineering
Thesis Supervisor

Accepted by .....
David E. Hardt
Chairman, Department Committee on Graduate Students

Optical System for High-Speed Atomic Force Microscope

by

Kwang Yong Lim

Submitted to the Department of Mechanical Engineering
on May 7, 2010, in partial fulfillment of the
requirements for the degree of
Master of Science in Mechanical Engineering

Abstract

This thesis presents the design and development of an optical cantilever deflection sensor for a high speed Atomic Force Microscope (AFM). This optical sensing system is able to track a small cantilever while the X-Y scanner moves in the X-Y plane at 1KHz over a large range of 50x50 microns.

To achieve these requirements, we evaluated a number of design concepts among which the lever method and the fiber collimator method were selected.

Experiments were performed to characterize the performance of the integrated AFM and to show that the cantilever tracking while the scanner is in operation was accomplished. A triangular grating was imaged with the lever method optical subassembly integrated with the scanner to demonstrate the effectiveness of the approach.

Thesis Supervisor: Kamal Youcef-Toumi
Title: Professor of Mechanical Engineering

Acknowledgements

First and foremost, I would like to thank Professor Youcef-Toumi for allowing me to work on this Atomic Force Microscope project.

I would like to thank Dr. Vijay Shilpiekundula, Dr. Dan Burns and Assistant Professor Georg Ernest Fantner for introducing me to the practical aspects of my thesis work.

I would also like to thank Iman Soltani Bozchalooi and Andres Schuh for helping me conduct all the experiments on the optical setup. I wish them success in their research work.

I would like to thank Leslie Regan, Laura Kampas and Louis Graziano for their strong support.

I would also like to thank UROP students, Benjamin Williams, Bruno Piazzarolo and Reuben Aronson, for their hard work on the construction of the prototypes.

I would also like to thank Samsung Electronics for their sponsorship.

Contents

List of Figures

List of Tables

Chapter 1

Introduction

This thesis presents a novel method of mechanically tracking the tip of a cantilever mounted on a high-speed atomic force microscope (AFM). The cantilever is moving with the AFM scanner at a high speed (i.e. 1kHz) while the cantilever (including the cantilever tip) is oscillating at an amplitude that is to be captured by our proposed optics system. As an introduction, this chapter discusses the basic operation of the atomic force microscope (AFM) with emphasis on current optical Z-deflection sensing methods for the AFM.

1.1 Atomic Force Microscope Basics

The entire AFM system consists of essentially the microscope, analog controller and computer. Figure 1-1 illustrates these main components and their connections. The user begins imaging using the computer and this computer sends commands to the analog controller which in turn converts the imaging commands into analog driving signals for the AFM scanner (i.e. X,Y,Z and tapping signals for the piezo actuators in the microscope.) The microscope receives commands from the analog controller, interacts with the sample and send cantilever deflection signals back to the analog controller. This analog controller then sends all the data captured and processed

with analog electronics to the computer for further processing and display. Since this thesis is on a new optical detection system the tracks the cantilever in an AFM, we will focus on the microscope and how the optical system fit in as a sensor in the controls of the AFM.

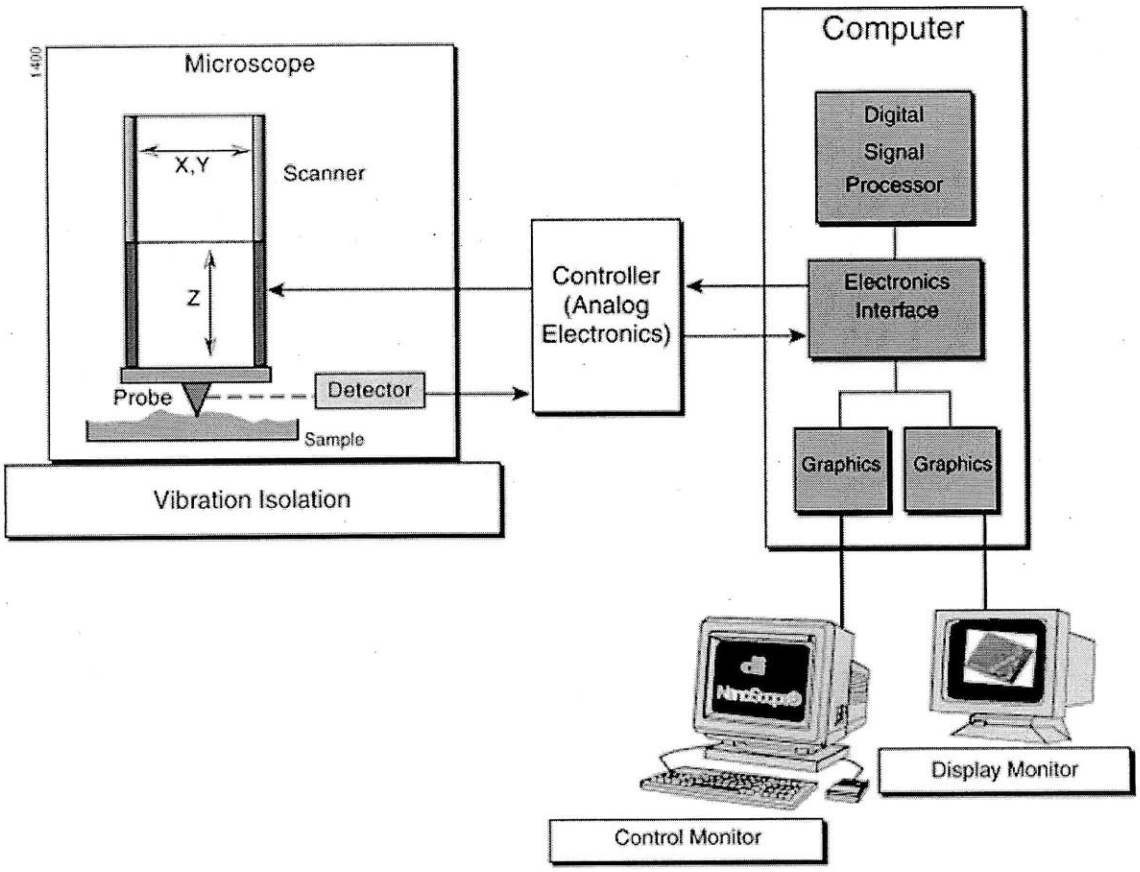

Figure 1-1: Diagram of the key components of an AFM.[1]

The microscope in turn consists of the scanner, probe (also known as a cantilever) and detector. The scanner receives analog commands from the analog controller and actuate the scanner in the X, Y and Z axis. The probe interacts with the sample and deflects due to contact or non-contact forces, depending on the operating mode of the AFM. These contact or non-contact forces cause the cantilever to deflect and this deflection is captured by the detector and a deflection signal is sent back to the

analog controller and finally to the computer to produce an image.

AFMs can operate in different modes. These are:

Contact mode	Constant cantilever deflection with no tapping/dither piezo
Tapping mode	Constant oscillation amplitude with a tapping piezo
Non-contact mode	Constant oscillation amplitude or frequency

Figure 1-2 shows the feedback to the controller electronics required for different operating modes of the AFM.

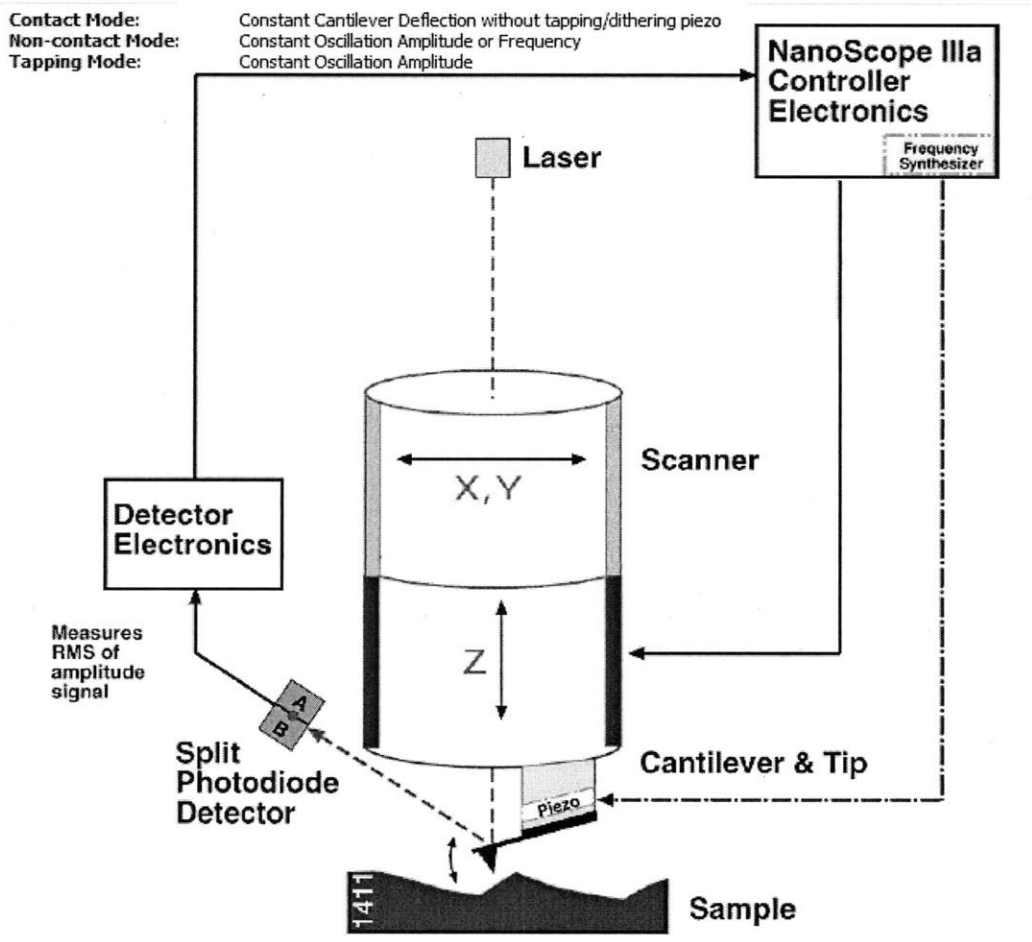

Figure 1-2: Feedback of different modes.[1]

The focus of this thesis is on the optical system of the AFM. We will discuss the details of the optics system in conventional AFMs in the next section.

1.2 Optical Z-Deflection Sensing Techniques

The detector part of the microscope consists of a solid state laser diode, focusing lens, a mirror, a quadrant photodiode detector and top minus bottom amplifier circuit for the photodiode detector. Figure 1-3 shows a diagram with the laser beam path from the solid state laser diode to the quadrant photodetector. The solid state laser diode can be adjusted in fine steps to move in the X and Y direction so that the laser spot can be made to fall on the tip of the cantilever. Fine adjustment of the laser spot is necessary whenever a new cantilever is mounted. This is further discussed in the section 1.3. The focusing lens is used to focus the laser spot to a spot that has a diameter smaller than the width of the back of the cantilever. Figure 1-4 illustrate this requirement so that there is minimal stray laser beam that falls outside the back of the cantilever reflected from the sample.

The laser beam that is reflected off the back of the cantilever, is redirected by a tilted mirror to a quadrant photodiode detector. This detector output the intensity of the top 2 quadrants, the bottom 2 quadrants and the difference in intensity of the top 2 quadrants and the bottom 2 quadrants.

The cantilever is normally tilted at 11° from the horizontal plane as is shown in figure 1-3.

To provide a spatial perspective of the placement of the components in the optical system of an actual AFM head, figure 1-5 is shown below[1]. There is another set of screws labeled as mirror adjustment screws. These screws are necessary to direct the laser beam to fall at the center of the photodiode detector so that the output of the difference between the top 2 quadrants and the bottom 2 quadrants is near zero

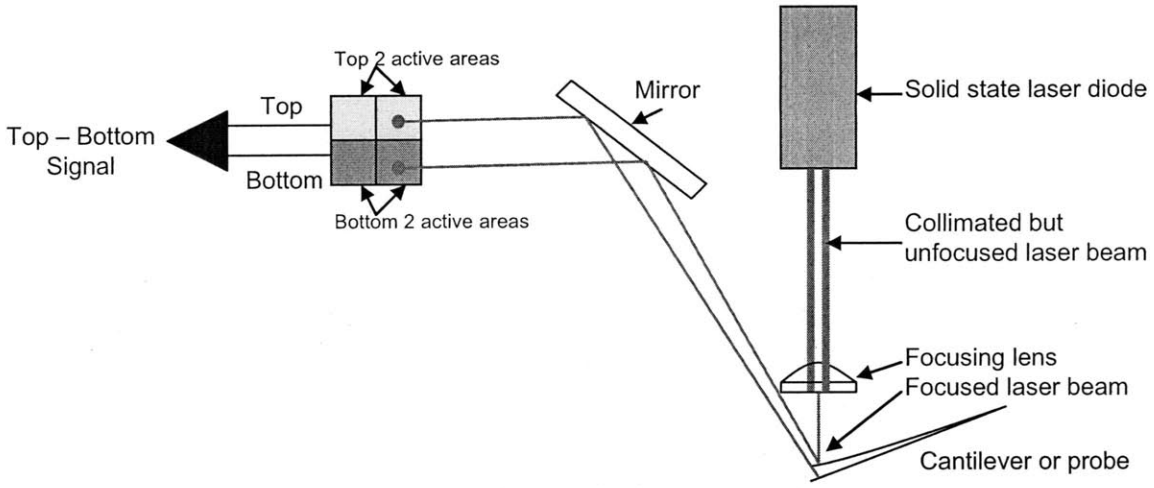

Figure 1-3: Diagram of key components of optical Z-deflection sensing.[1]

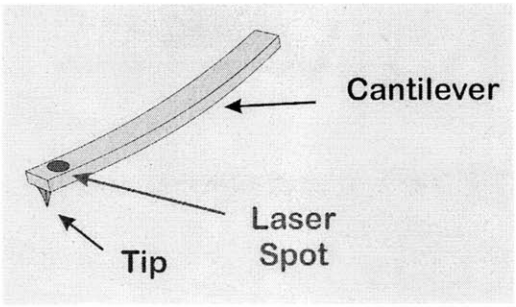

Figure 1-4: Red laser spot with a diameter smaller than the width of the tip of a cantilever.[2]

when the cantilever is stationary. The laser reflection window shown in figure 1-5 is to help the AFM user center the laser spot onto the center region of the photodiode detector.

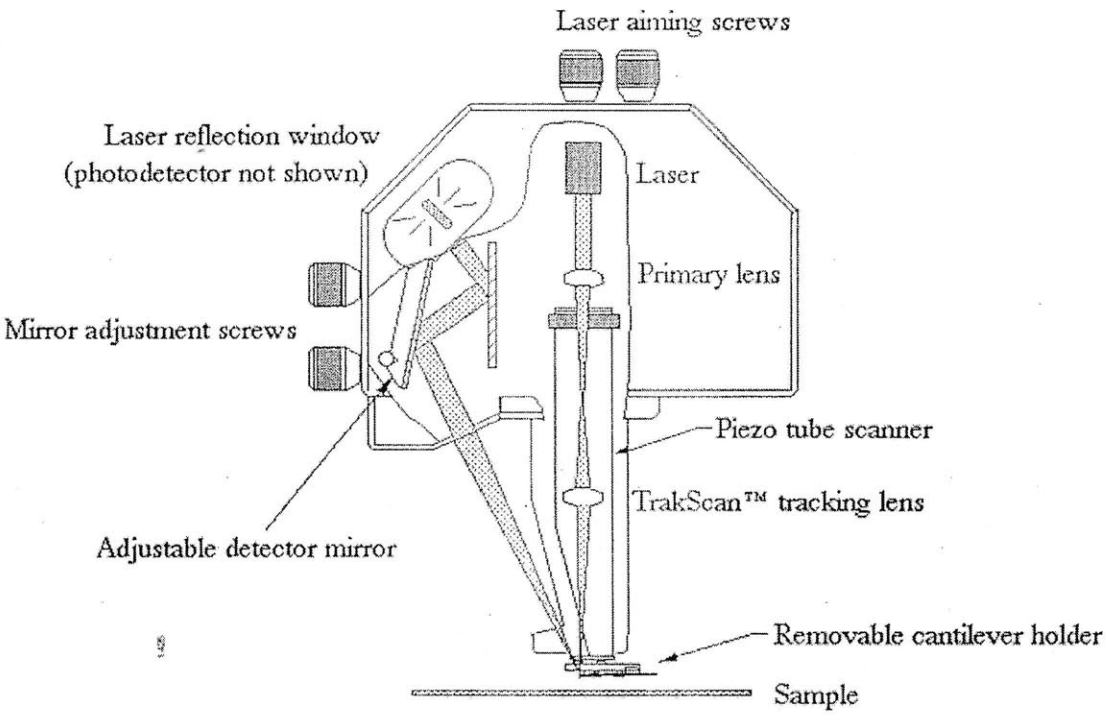

Figure 1-5: Optical path of a conventional AFM.[1]

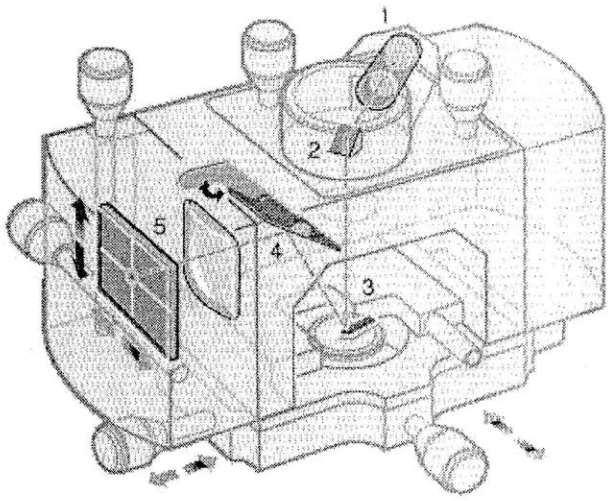

Labels:

1. Laser
2. Mirror
3. Cantilever
4. Tilt mirror
5. Photodetector

Figure 1-6: Optical path of a conventional AFM in 3D.[1]

The actual placement of the optical components in 3 dimensional is shown in figure 1-6.

1.3 Fine Adjustment Of Laser Spot during Initial Setup

This section is important as it presents the steps taken whenever an AFM is setup for imaging and our optics design has to consider and accommodate a facility for fine adjustment of laser spot location. Fine adjustment of the laser spot position is necessary whenever the cantilever is changed. Cantilevers are changed when a different tip is required for imaging different samples or when the cantilever tip is broken. This section explains in detail the steps to accurately align the laser spot onto the cantilever tip.

Figure 1-7 shows the 6 steps that is necessary to align the laser stop. Assuming the laser spot is off the back of the cantilever further up in the X direction. The first step is to use the X axis laser aiming screw (fine pitch) shown in figure 1-5 to move the laser spot toward the back of the cantilever. Continue in the same direction so that the laser spot exceeds the back of the cantilever as shown in step 2. This can be observed when the intensity of the laser spot that get reflected from the back of the cantilever is significantly reduced (as the sum signal of the quadrant photodiode detector decreases significantly).

As shown in step 3, move the laser spot back to the cantilever while observing the sum output signal of the quadrant photodiode detector. Steps 4-6 is to ensure that the laser spot is at the back of the cantilever. This is accomplished by using the Y axis laser aiming screw (fine pitch) shown in figure 1-6 so that the laser spot exceeds the pointed end of the cantilever and moving the laser spot back slowly to the desired

location(i.e. right at the pointed end of the cantilever).

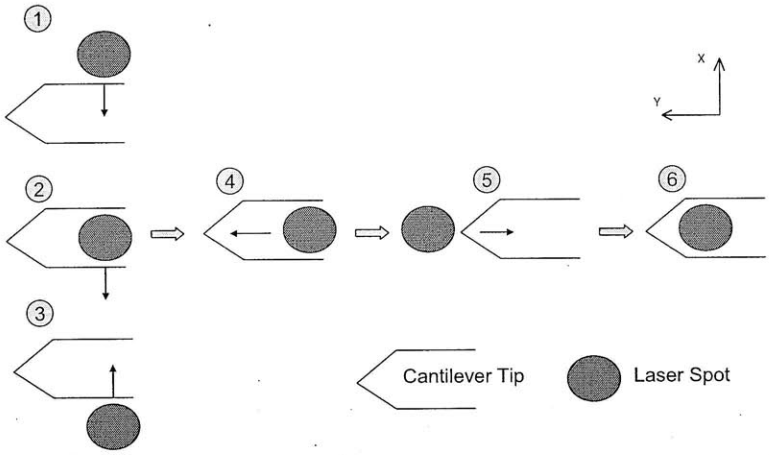

Figure 1-7: 6 steps to align laser spot onto cantilever tip.

1.4 Role of Optics System and Quadrant Photodiode Detector in AFM Controls

Figure 1-8 shows the complete feedback control of the AFM system. We use a tapping mode AFM as an example. A constant deflection or oscillation amplitude is set as a reference to the control system of the AFM. As the cantilever oscillates or continues tapping, the tip of the cantilever and the surface that is to be imaged interacts and the interaction causes the cantilever to deflect. This cantilever deflection is captured by the photodiode detector and a top minus bottom signal is sent to the analog controller and then to the computer.

The deflection signal from the quadrant photodiode detector is compared to the set reference oscillation amplitude and an error signal is generated. This error is compensated by the computer and analog controller to maintain a constant oscillation amplitude of the cantilever. The different heights thus recorded (i.e. by maintaining

a constant oscillation of the cantilever tip) is matched to the X and Y coordinates where the height is taken and an image can be generated.

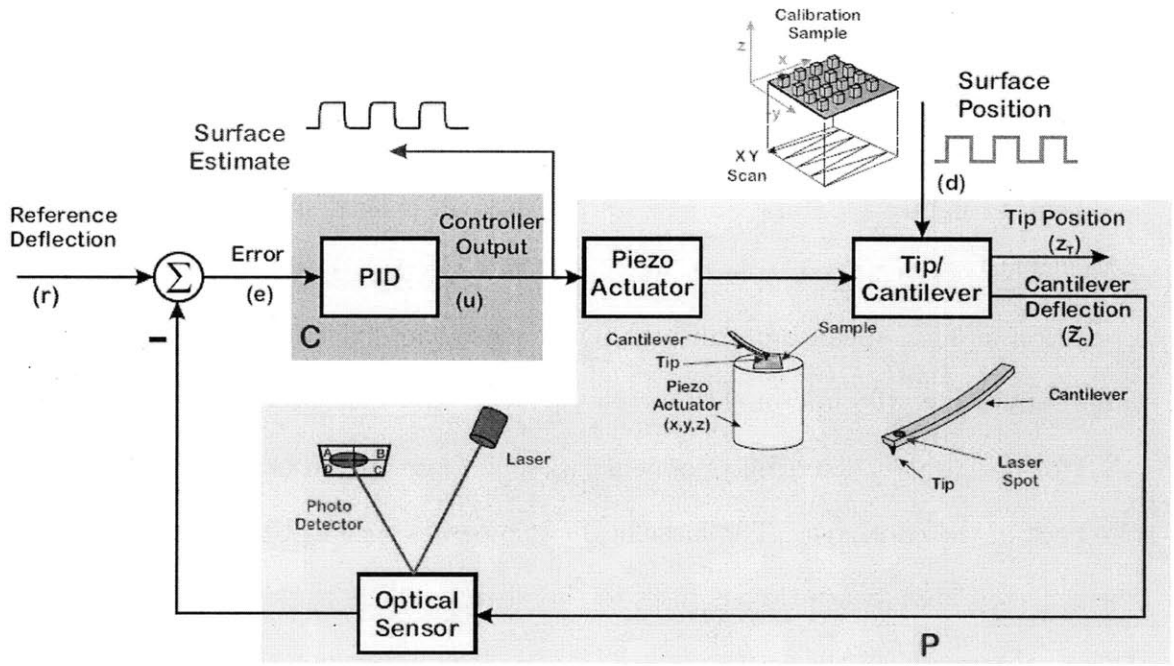

Figure 1-8: Feedback control of the AFM.[2]

1.5 Optical Systems for High Speed Large Range AFM

There are numerous patents and papers published that involves the development of optical system for high speed or large range AFM. We will discuss 2 designs that that have the most complete design and most stringent specifications. The next 2 paragraphs will describe these patents on optical systems for high speed and large range AFM respectively.

Veeco Instruments Inc. has a patent that describes a design for an optical system for a high speed AFM [4]. The patent claims that the optical system is able to sense

the deflection of the cantilever when the scanner is in operation at 1000 lines/second. However, the range of their AFM design is only 20 microns.

This patent uses an objective lens with adjustment mechanisms built into the optical subassembly. The optical path is similar to our objective lens method and this method is described in chapter 3.

Another patent by Hung and Fu [5] presents an optical system for a large range AFM. This design is not able to sense cantilever deflection when the scanner is in operation at high speed but will be able to sense the deflection of the cantilever at large ranges (i.e. 100 microns).

This design uses a central prism that directs a laser beam from the laser diode to the back of the cantilever. The laser beam also passes throught an objective lens and the reflected laser beam travels back to the objective lens as described in chapter 3. Due to the weight of the setup, the optical subassembly is not able to track the back of the cantilever when the scanner is operating at high speed.

There is also another patent by IBM that uses a fiber optic cable to guide the laser beam into the central stage of the X-Y scanner [6]. The use of fiber optic cable as a laser source is similar to our fiber collimator design described in chapter 8.

1.6 Thesis Outline

The rest of this document will be organized as follows. Chapter 2 will discuss the problem statement. The critical challenges of tracking a cantilever are elaborated. Chapter 3 will discuss about the use of an objective lens to focus the laser beam onto the back of the cantilever. Chapter 4 will discuss the lever method for tracking the cantilever. Chapter 5 will present the kinematics of the lever method and the errors that it will introduce. Chapter 6 will discuss the dynamics of the lever method. Chapter 7 will present design and fabrication of the mechanical assembly for the

lever method. Chapter 8 will present the fiber collimator method design. Chapter 9 contains the design and fabrication of the quadrant diode photodetector circuit. Chapter 10 is the results of the lever method. Chapter 11 is the conclusion.

Chapter 2

Cantilever Tracking Problem and Different Designs

2.1 Introduction

This chapter will present the challenges that are faced when tracking the cantilever tip that is moving in the X and Y direction at 1kHz. In addition, our scanner range is large (i.e. 50x50 microns) and we are using small cantilevers. Furthermore, we also need to incorporate an adjustment mechanism to the optics subassembly so that we can focus the laser spot onto the back of the cantilever whenever a new cantilever is mounted. Other methods for tackling the aforementioned challenges are suggested and their tradeoffs summarized.

2.2 Challenges of High Speed AFM Cantilever Tracking

There are several challenges to overcome when tracking the cantilever that is moving at 1kHz in both the X and Y direction, such as keeping the laser spot on the back

of the cantilever while the cantilever is moving (i.e. with a small cantilever with a width of only 10 microns) and incorporating facility for initial adjustment when a new cantilever is mounted (described in detail in section 1.3) and the error that is generated as the cantilever scans the image when the optical system is tracking the cantilever. In addition, due to the small size of the cantilever, we need to make sure that the size of the laser spot is smaller than the width of the cantilever (for the small cantilever, the width is about 10 microns). This section will describe various ideas proposed and provide a summary of their trade-offs.

The fundamental requirements of this design are:

- Mechanism to allow optics to follow the movement of the scanner (i.e. tracking the cantilever when the cantilever is imaging at high speed and large range)
- Optics to focus the laser spot of a diameter smaller than 10 micron onto a 10 micron cantilever width due to the use of small cantilever
- Facility to incorporate fine adjustment mechanism to position the laser spot onto the tip when a new cantilever is mounted.

To understand the difficulty in tracking the cantilever at high speed (i.e. 1KHz) while imaging, we will describe the scanner design we adopted. The range of the scanner (i.e. largest sample it can image) is 50 microns in both the X and Y direction. Figure 2-1 and 2-2 shows the parallel scanner design we adopted (for detailed description, please refer to [3]).

Our high speed AFM scanner scans in both the X and Y direction at 1kHz. The range of the scanner is also larger than conventional AFM. It can be seen clearly from figure 2-3 that the cantilever moves together with the scanner during imaging while the grating or sample remains stationary. This is known as a probe scan AFM which is a requirement because the sample that we are scanning is large and heavy.

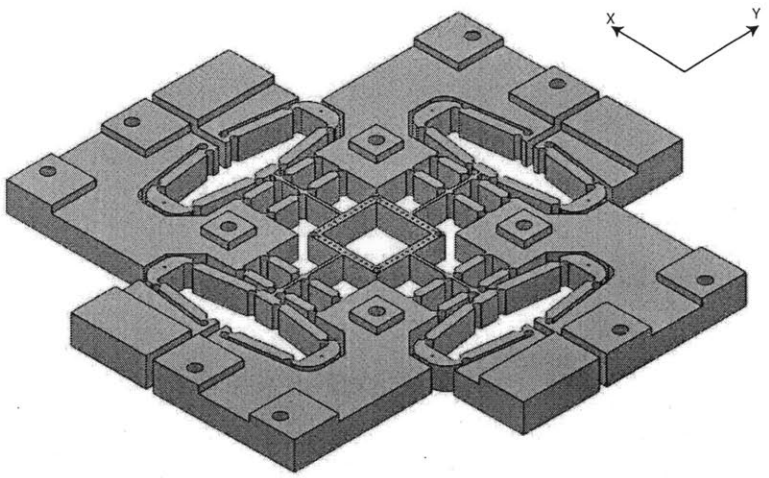

Figure 2-1: Parallel scanner design.

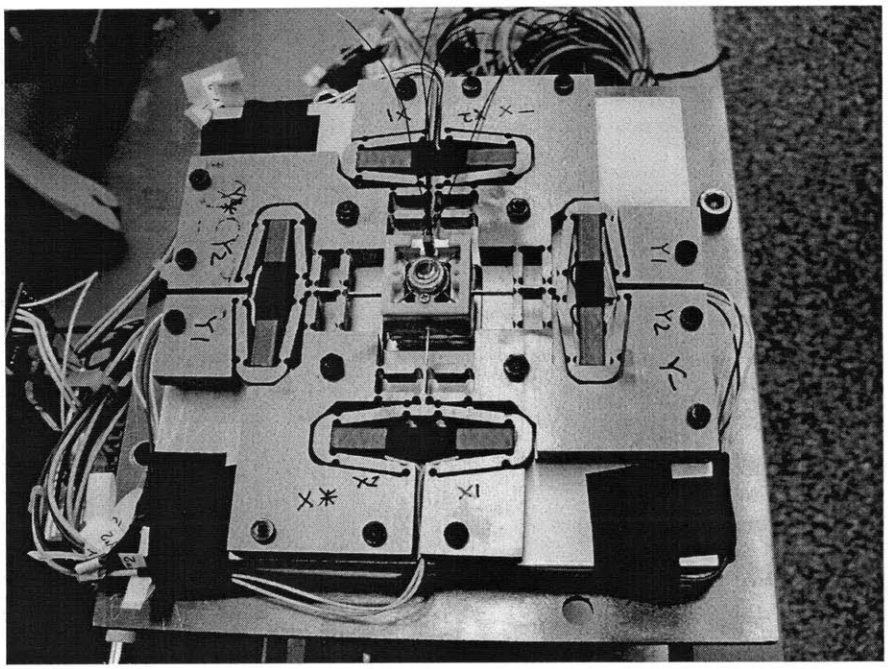

Figure 2-2: Photo of scanner with piezos mounted.

There are several challenges when tracking a cantilever mounted on a parallel scanner that is imaging at 1kHz. The optics need to be able to track the cantilever

at high speed and still maintain a large range. As a result, the optical subassembly must not affect the dynamics of the X-Y scanner when the scanner is in operation. The laser spot size must also be smaller than 10 microns so that the laser will remain on the back of the cantilever when the scanner is in operation. Finally, the design will also need to allow the AFM user to adjust the optical subassembly so that the laser spot will fall on the back of the cantilever when a new cantilever is mounted.

These challenges makes the design of the optics system difficult and various design proposals that we explored are presented in section section 2.3.

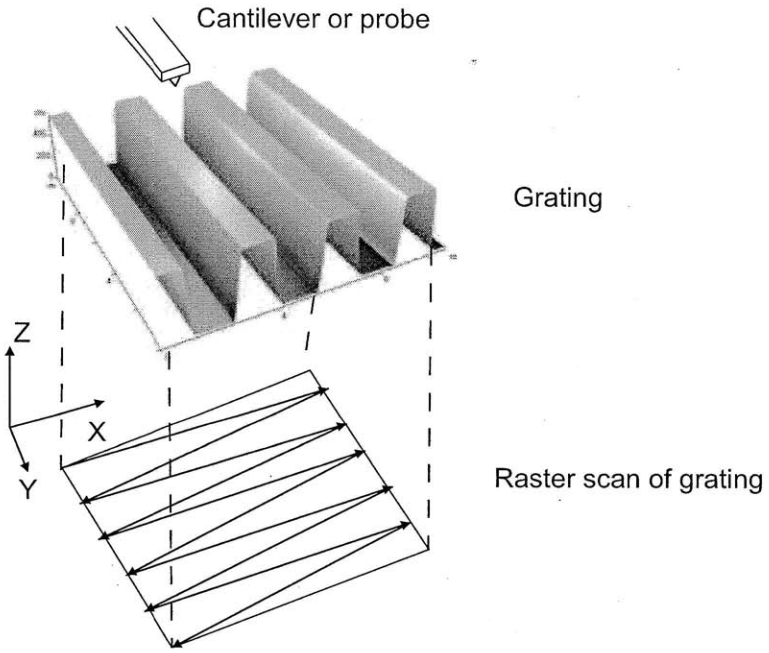

Figure 2-3: Depiction of raster scanning of a grating using our proposed parallel scanner.

2.3 Alternative Design Proposals for High Speed AFM Cantilever Tracking

This section will describe the various alternative designs we considered and list out their advantages and disadvantages. A summary of these different alternatives is tabulated in table 2.1.

One proposal was to use a 2-axis galvanometer scanning mirror to direct the laser beam onto the cantilever. Since the scanner is moving at 1KHz in both the X and Y direction, the bandwidth of a suitable galvanometer mirror should be approximately 5 times (i.e. 5 kHz). The schematic is shown in figure 2-4.

One advantage of this method is that the galvanometer has a range of at least 50 microns. The optical subassembly is also totally detached from the X-Y scanner, which means that the weight of the optical subassembly has no effect on the X-Y scanner.

There are various difficulties in this concept. The main difficulty is that the fastest galvanometer scanning mirrors that is commercially available is only about 1KHz bandwidth at small angles. The resolution of the galvanometer will also be in the range of microns instead of nanometers due to the resolution of the galvanometer mirror. It will also be difficult to align and assemble the galvanometer with the back of the cantilever. Tracking errors from the galvanometer actuators will increase error sensitivity[1] and this setup will be expensive. Of course, one can look into the design of a high speed and large range galvanometer.

[1]Error sensitivity is how sensitive the system is to errors

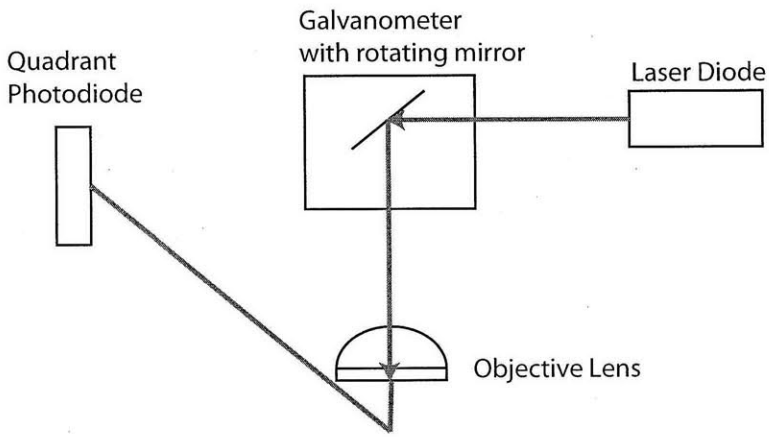

Figure 2-4: Galvanometer method for tracking cantilever.

The second proposal was to use a small fiber collimator for the laser source and an image preserving fiber bundle for directing the reflected laser beam from the back of the cantilever to the quadrant photodetector diode that is mounted away from the scanner.

This method has the advantage of a light optical subassembly that is attached to the central stage of the X-Y scanner. Since the optical subassembly is light and attached to the central stage of the X-Y scanner, it is likely to be able to reach a high bandwidth of 1KHz and a large range of 50 microns. Alignment and assembly will also be easy as the design has to accommodate only the fiber bundle and the laser fiber collimator.

This method is not favorable because spatial information will be lost in the low resolution fiber bundle, coupling efficiency to the fiber bundle will be low and both the tiny fiber collimator and the fiber bundle are expensive.

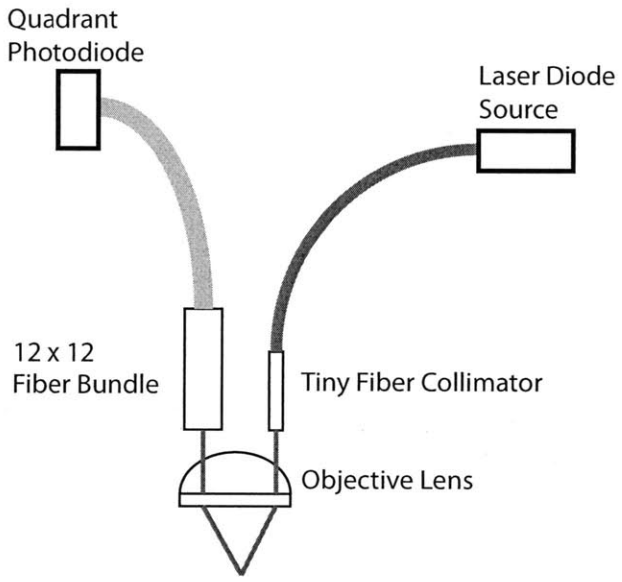

Figure 2-5: Fiber bundle method for tracking cantilever.

The third alternative is to use penta prisms and flexures that are able to rotate the entire optics subassembly about the center of the penta prism.

The advantage of this method is that the laser diode module and quadrant photodiode detector can be mounted outside the optical subassembly that is attached to the X-Y scanner. This reduces the weight of the optical subassembly and a light optical subassembly means that the design is likely to reach a bandwidth of 1KHz and a large range of 50 microns.

However, we anticipate that there will be difficulties in locating the exact center of the penta prism and difficulty in assembly. As a result, this method is not adopted.

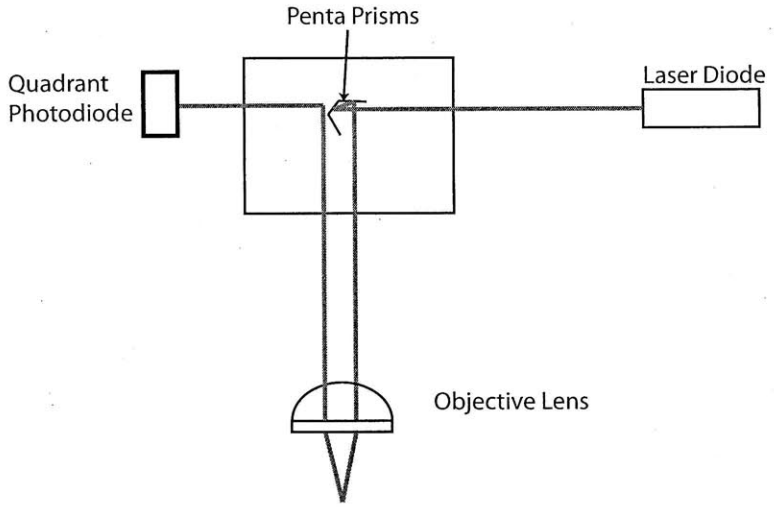

Figure 2-6: Penta prism method for tracking cantilever.

The fourth alternative is to make use of a mechanical connection between the optical subassembly and the X-Y scanner. The laser comes from the laser diode on the right of figure 2-7. The laser beam then gets focused onto the back of the cantilever and the reflected laser beam travels to the photodiode detector. Using 2 flexures, we pivot the optics subassembly about the center of the top flexure to gain mechanical advantage, thereby, reducing effective mass.

The advantage of this method is that the reduction in the effective mass of the optical subassembly on the central stage of the X-Y scanner is reduced significantly. As a result, we expect the bandwidth of this method to be above 1KHz and the range to be above 50 microns.

This method, however, will introduce an error as the optical subassembly tilts. There may also be mechanical coupling of resonance of the optical subassembly to the X-Y scanner.

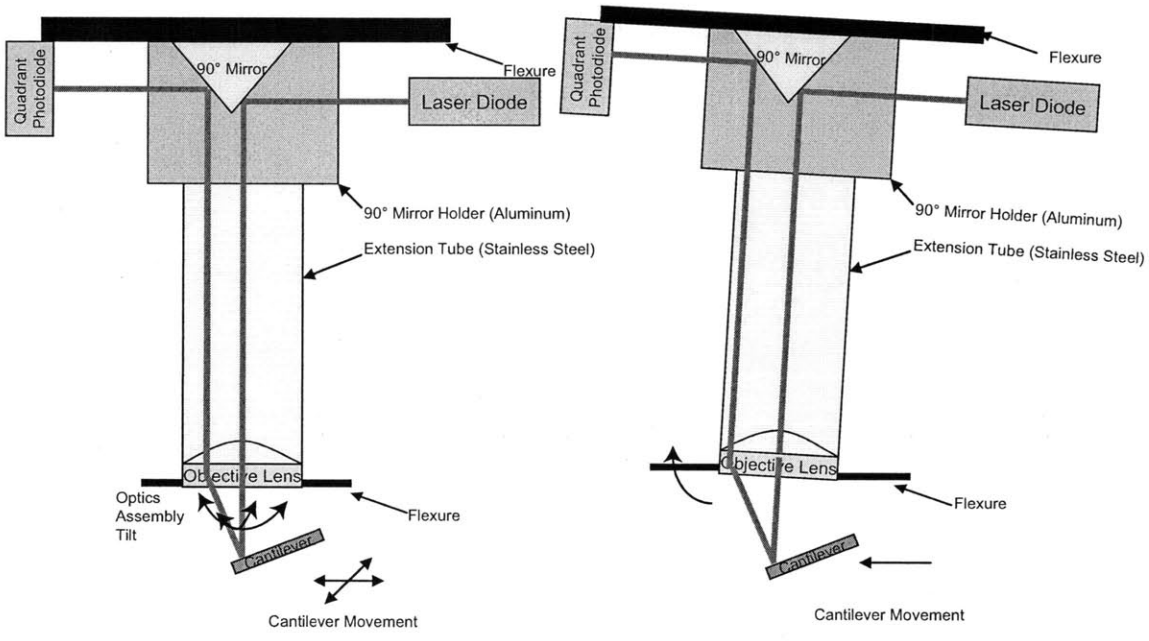

Figure 2-7: Lever method for tracking cantilever.

The fifth proposal is shown in figure 2-8. Figure 2-8 shows a novel method that uses a small fiber collimator to lead the laser beam from an external laser source to the objective lens. This method eliminates the need for a large solid state laser diode and removes the need for bulky and heavy fine adjustment mechanisms.

This method has the advantage that the laser diode module is mounted outside of the optical subassembly. This method also does not require heavy adjustment mechanisms required to align the laser diode module and the photodiode detector. We expect this design to be able to reach a bandwidth of 1KHz and a range of at least 50 microns.

However, we need to incorporate a way to adjust the back of the cantilever to the focal point of the objective lens since the laser diode and objective lens is fixed.

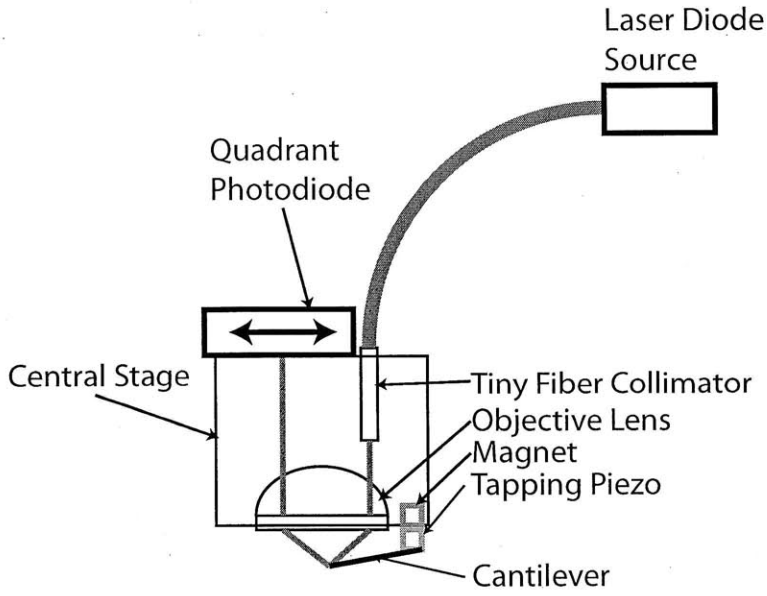

Figure 2-8: Fiber Collimator method for tracking cantilever.

Table 2.1 list the advantages and the disadvantages of the each proposed method.

Table 2.1: Summary of Tracking Methods

Specifications	Mechanical	Galvanometer	Fiber Bundle	Penta Prism	Fiber Collimator
Bandwidth	$\geq$ 1kHz	$\leq$ 1kHz	$\geq$ 1kHz	$\geq$ 1kHz	$\geq$ 1kHz
Range	50 micron	50 micron	50 micron	50 micron	50 micron
Resolution	nm	microns	nm	nm	nm
Alignment	Difficult	Difficult	Easy	Difficult	Difficult
Assembly	Difficult	Easy	Easy	Difficult	Easy
Cost	Low	High	High	Low	High
Weight	High	Low	Low	Low	Low

2.4 Summary

In this chapter, the challenges that are faced when tracking the cantilever that is moving in the X and Y direction at 1kHz and with a range of 50 microns is presented. Finally, a summary of the performance of a scanning mirror method versus a mechanical tracking method is tabulated.

Chapter 3

Objective Lens for AFM Optics

3.1 Introduction

To track a small cantilever at high speed, large range and with minimum error, we chose to use an objective lens method for the optics. In this chapter, we describe the use of an objective lens to focus the laser beam onto the back of the cantilever and direct the reflected laser beam back into the photodiode detector. The optics ray tracing is presented and the optics components are chosen so that the laser spot size is focused to under 10 microns. The depth of focus for this lens is discussed and the optical power along the laser beam path is recorded.

3.2 Overview of Optics System

3.3 Geometrical Laser Path Tracing

This section will describe how the laser beam will travel from the laser diode to the cantilever and back to the quadrant photodiode. Figure 3-1 shows the layout of the optics components and the travel of the laser path from the solid state laser diode, the 90° mirror, objective lens and the quadrant photodiode detector. The laser source

from the solid state laser is directed at the objective lens. The laser beam is reflected 90° by the 90° mirror and focused onto the back of cantilever with the help of the objective lens. The reflected laser beam is directed back into the left side of the objective lens. It travels back to the left side of the 90° mirror and finally to the quadrant photodiode detector.

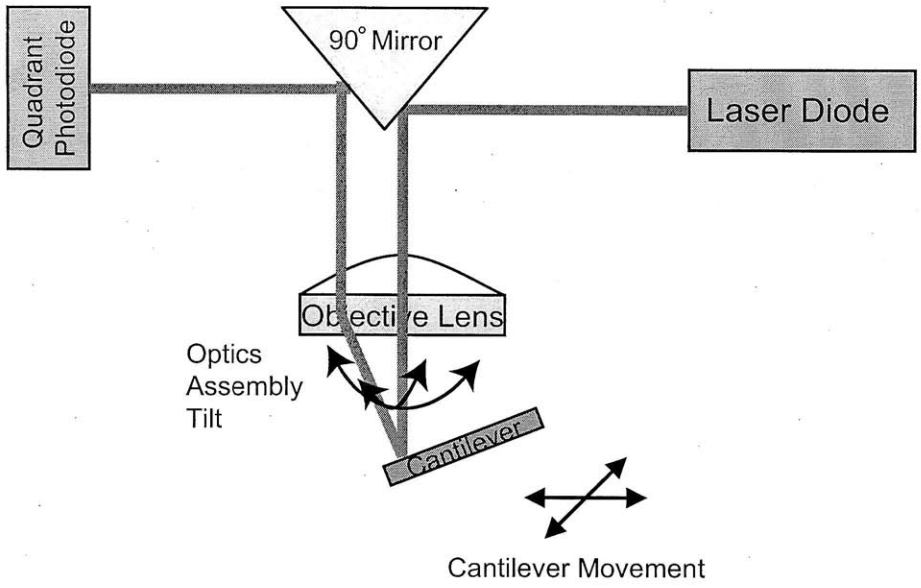

Figure 3-1: A diagram of the laser path from the laser diode to the quadrant detector.

3.4 Selection of Objective Lens

This section describes our specifications for the objective lens we chose. The proper selection of an appropriate objective lens is crucial and it is selected to fulfill the following requirements:

The proper selection of an appropriate objective lens is crucial and it is selected to fulfill the following requirements:

Lens diameter	$\leq$ 7mm
Working distance	$\leq$ 5mm

Clear aperture	$\geq$ 4mm
Laser spot size	$\leq$ 5 microns
Numerical aperture	$\geq$ 0.5

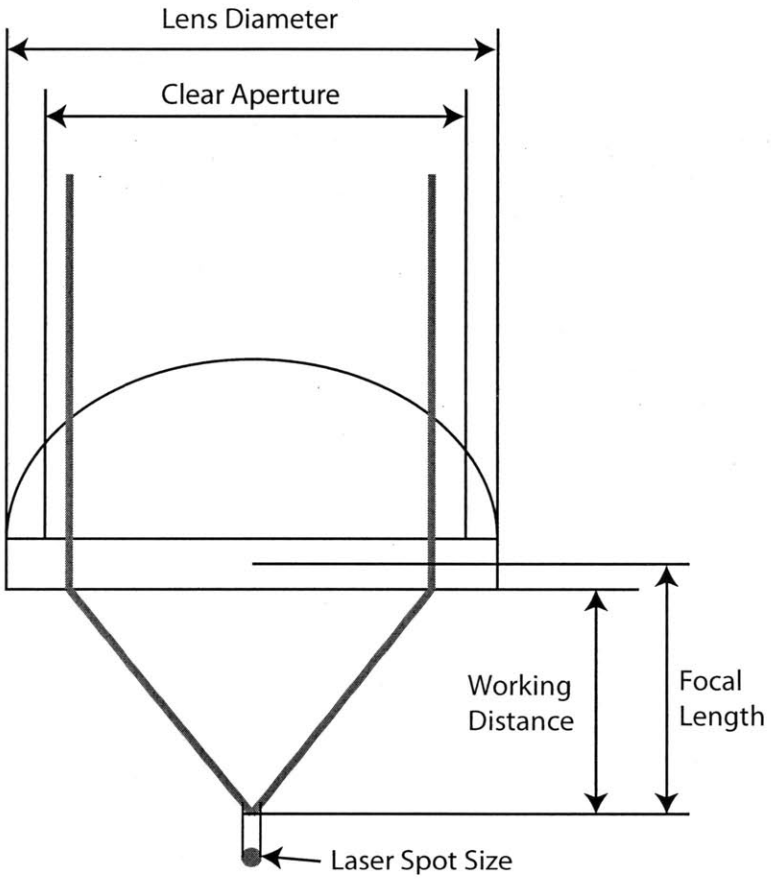

Figure 3-2: Parameters of a lens.

The lens diameter is the outside diameter of the objective lens as shown in figure 3-2. The lens diameter is preferred to be as small as possible to reduce the weight at the central stage of the scanner. This also affects how close the Z piezos can be to the focal point of the objective lens when mounted on the central stage.

The working distance is the distance from the face of the lens to the focal point as shown in figure 3-2. This is the actual distance that the back of the cantilever has

to be placed from the face of the lens. It is different from the focal length as the focal length starts inside the lens. The working distance is the actual parameter we use to position the back of the cantilever from the face of the lens.

The clear aperture is the diameter that light can be focused effectively without clipping. It is shown in figure 3-2. It is smaller than the lens diameter. Outside the clear aperture, the laser beam is dispersed. A larger clear aperture is preferred so that we can allow a larger cantilever tilt angle when the laser beam is reflected back into the objective lens.

The laser spot size is the diameter of the focused laser beam at the focal point of the objective lens as shown in figure 3-2. A small laser spot diameter is preferred so that the laser spot will not fall out of the back of the cantilever when the scanner is in operation.

The numerical aperture is a dimensionless number that characterizes the angle over which the lens can emit and receive light, NA. Figure 3-3 shows the angle of the NA. The NA needs to be a large as possible to enable the smallest spot size.

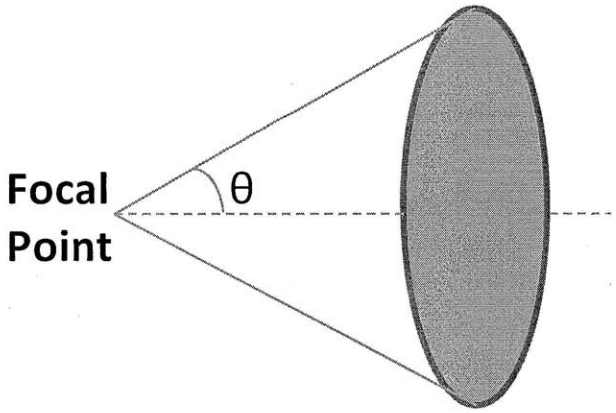

Figure 3-3: Numerical aperture of a lens.

This can be estimated with the following equation:

$$NA = n \sin \Theta \tag{3.1}$$

where NA is the numerical aperture, n is the index of refraction and Θ is the half-angle of the maximum angle that light exits or is received by the lens.

$$NA \simeq \frac{2\lambda}{\pi D} \tag{3.2}$$

where λ is the wavelength of the laser beam (i.e. 650nm in our system) and D is the diameter of the laser spot. With a numerical aperture of 0.55 and a wavelength of 650nm, we can calculate the laser spot size to be 1.6 microns.

The working distance is the distance from the front of the lens to the focal point of the lens. It is thus related to the focal length of the lens. The focal length is in turn related to the numerical aperture.

$$NA = n \sin \Theta = n \sin \arctan \frac{D}{2f} \approx n \frac{D}{2f} \tag{3.3}$$

From the derivation, it shows that to obtain a lens with high NA, it is desirable to select a lens with a large diameter and a focal length that is small. There is a trade-off as there is a limit on the diameter of the lens and an optimal focal length to accommodate the Z and tapping/dithering piezos.

The lens that is selected will have to have a good set of parameters that satisfy all the specifications. The selected lens is a precision molded aspheric lens 46-351 from Edmund Optics. The lens has the following specifications:

Table 3.1: Summary of Lens Specification

Parameters	Requirement	Lens Specifications
Lens diameter	$\leq$7mm	6.325mm
Working distance	$\leq$5mm	2.91mm
Clear aperture	$\geq$4mm	4.95
Laser spot size	$\leq$5 microns	Approximately 2 microns
Numerical aperture	$\geq$0.5	0.55

3.5 Selection of Solid State Laser Diode

We chose a solid state laser diode that is compact and has a well collimated circular laser beam. The laser diode that we used is the VLM2 Miniature Diode Laser Module from Coherent Inc. It is a 4mW laser diode module that is able to output a circular laser beam spot with a diameter of 1mm. The divergence is only 0.7mrad. The wavelength of the laser beam is 635nm and can be powered with just a 5V regulated power supply. The module is only 15mm in diameter and only 34mm in length. Figure 3-4 is a drawing of the laser diode module.

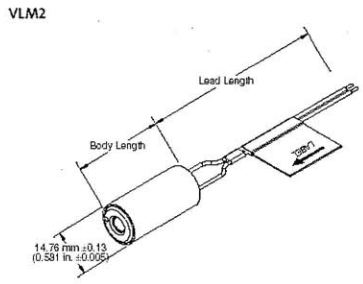

Figure 3-4: VLM2 laser diode module from Coherent.[13]

3.6 Depth of Focus

This section describes how depth of focus of a lens allow the laser spot size to be still under 10 microns even with the Z translation of the cantilever. The depth of focus is the maximum Z direction error of the cantilever that will allow the laser spot that falls onto the back of the cantilever to be still under 10 microns. This is shown in figure 3-5.

This means that even if the cantilever tip moves up or down by 5 microns in either direction, the laser spot diameter will still be below 10 microns, which in turn means that the laser spot will still fall onto the back of the cantilever.

This is important because we can make sure that the laser spot falls onto the back of the cantilever when the cantilever is oscillating.

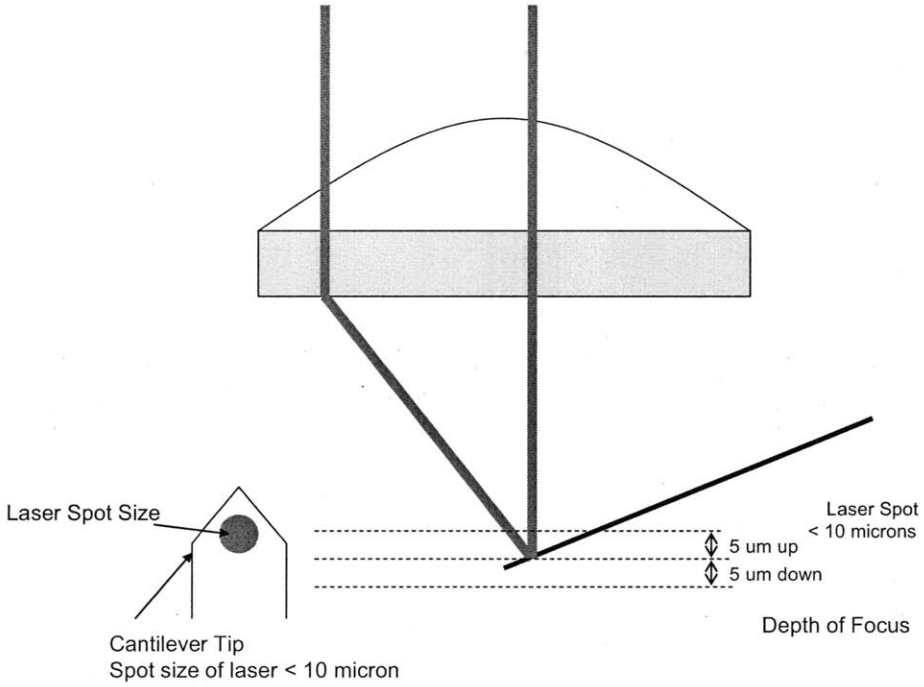

Figure 3-5: Depth of focus for objective lens.

3.7 Optical Power Along Laser Beam Path

This section describes the optical power at different points of the laser beam path. Figure 3-6 shows the optical power along the path that the laser beam travel. It can be seen that optical power is lost as the laser beam is reflected from the cantilever tip. The optical power that the solid state laser emits is 2.4mW and the optical power of the laser that comes out of the objective lens is 1.8mW. The optical power that does not fall onto the cantilever is 400 microwatts. According to measurement, the laser beam power that falls onto the quadrant photodiode is approximately 600 microwatts. This is sufficient for accurately tracking of the cantilever oscillation.

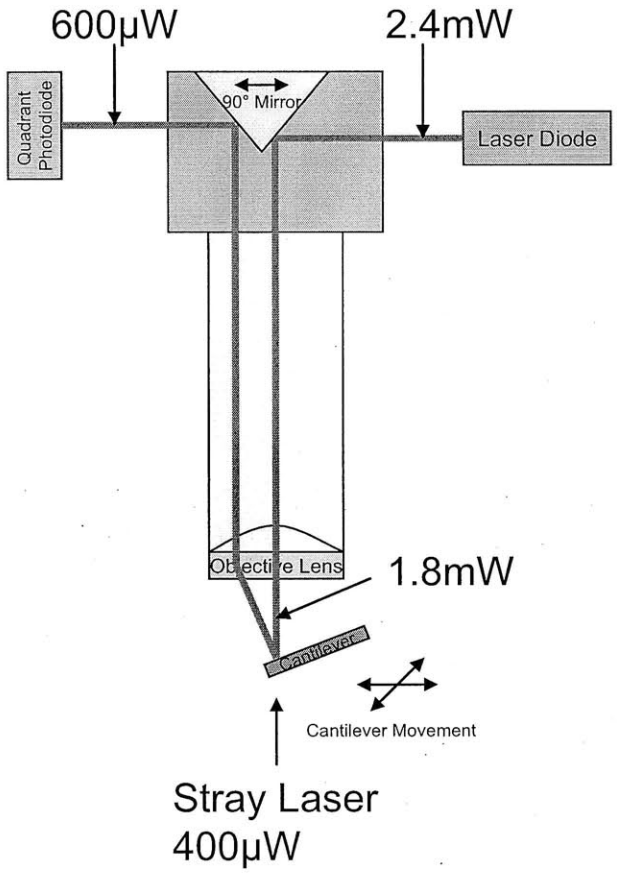

Figure 3-6: Intensity of laser at different points of its path.

3.8 Summary

We described the use of an objective lens in detail in this chapter. This is a mechanical mean of tracking the cantilever tip while maintaining high speeds (i.e 1kHz). The laser beam path is also presented and optics components selected based on required specifications.

This chapter addressed how the laser spot size is focused using the objective lens to under 10 microns so that the laser spot will not fall out of the back of the cantilever. We used an objective lens that has the correct parameters and thus satisfied the laser spot size requirement.

Chapter 4

Lever Method - Cantilever Tracking

4.1 Introduction

In this chapter, we describe a lever method that uses the objective lens described in chapter 3 to connect to the scanner so that the laser spot is able to track the back of the cantilever at high speed.

4.2 Mechanical Connection of Optical Subassembly and X-Y Scanner

This section describes in detail the lever method that uses a tube to mechanically connect the optical subassembly to the X-Y scanner and the components that are mechanically connected. Figure 4-1 shows the optical subassembly connected to the tube. The tube is in turn connected to the bottom flexure and this bottom flexure is connected to the central stage of the X-Y scanner.

We will describe the components of the optical subassembly and the adjustment

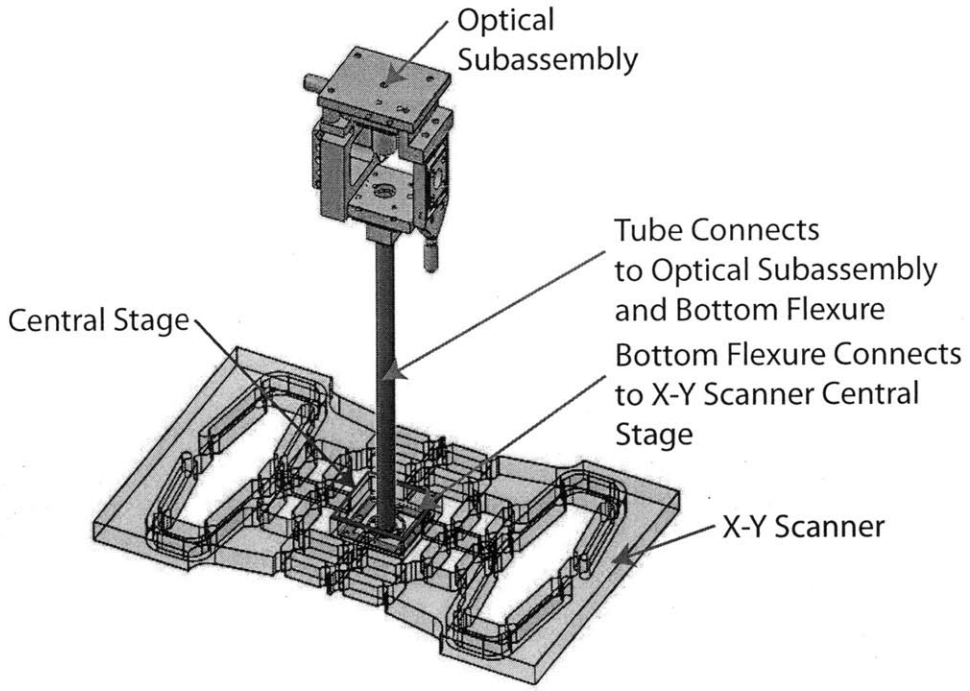

Figure 4-1: How optics is connected to central stage of X-Y scanner.

mechanism incorporated. We will also describe how the tube, objective lens and the bottom flexure is connected to the X-Y scanner. Figure 4-2 is an exploded view of the optical subassembly integrated with the X-Y scanner. At the very top of figure 4-2, there is a flexure that is attached to the optical subassembly. This flexure is to hold the optical subassembly and to allow the optical subassembly to rotate about the X and Y axis. The top plate and the 10mm spacer is used to hold the 1-axis slide A for the 90° mirror. The 90° mirror is mounted on the 90° mirror extension, which is in turn attached to the 1 axis slide at the top.

The purpose of the laser support and the 1-axis slide C in figure 4-2 is to hold the solid state laser. The 1-axis slide C allows the solid state laser to be adjustable in the X translation axis.

The purpose of the corner support and the 1 axis slide B in figure 4-2 is to hold the quadrant photodiode detector. The 1-axis slide allows the quadrant photodiode

detector to be translated in the Z axis for adjusting the photodiode detector so that the laser beam is at the center of the four quadrants of the quadrant photodiode detector.

The purpose of the bottom plate is to hold the laser support and the 1-axis slide C for the photodiode detector in place. In addition, the bottom plate is connected to the tube via a 3D printed bottom tube connect.

The tube is then connected to the bottom flexure and the objective lens. This bottom flexure is in turn connected to the X-Y scanner. This assembly couples the optical subassembly to the X-Y scanner mechanically.

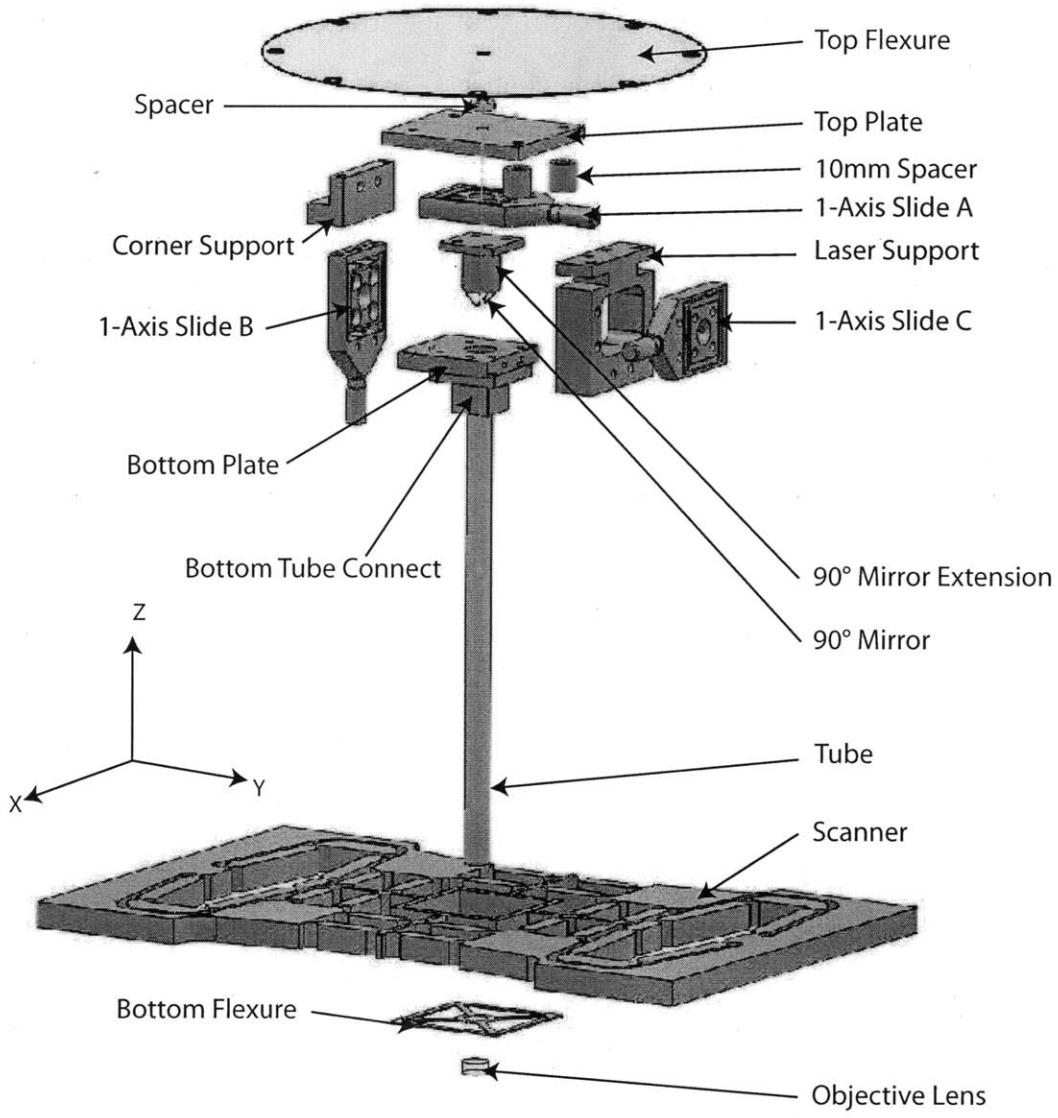

Figure 4-2: Exploded view of all mechanical parts in the optical subassembly in Prototype 3.

4.3 Tracking of the Cantilever

This section describes how the cantilever is tracked as the optics subassembly, that is connected to the X-Y scanner, tilts when the X-Y scanner is in operation. Figure 4-3 shows a top flexure and a bottom flexure that is connected to the optical subassembly and the X-Y scanner via the tube. The purpose of these 2 flexures is to allow the optical subassembly to tilt when the scanner is in operation. With the 2 flexures, the optical subassembly can rotate about the X (i.e. out of the page) and the Y axis as the X-Y scanner translates.

Figure 4-4 illustrates the path of the laser beam as the optical subassembly tilts and shows how the laser spot will fall onto the back of the cantilever when the cantilever moves to the left and to the right.

The laser beam that is emitted from the solidstate laser is reflected 90° by the 90° mirror. The laser beam is directed to the objective lens and the objective lens focuses the laser beam onto the back of the cantilever. The size of the laser spot is under 10 microns as described in chapter 3. The laser spot is reflected back into the objective lens and finally reflected 90° by the 90° mirror to the quadrant photodiode detector.

Figure 4-4 shows how the objective lens is able to keep the laser spot on the back of the cantilever even as the cantilever is moving. The focal point of the objective lens is still on the back of the cantilever as the cantilever moves. The addition of an objective lens thus is crucial in tracking the back of the cantilever.

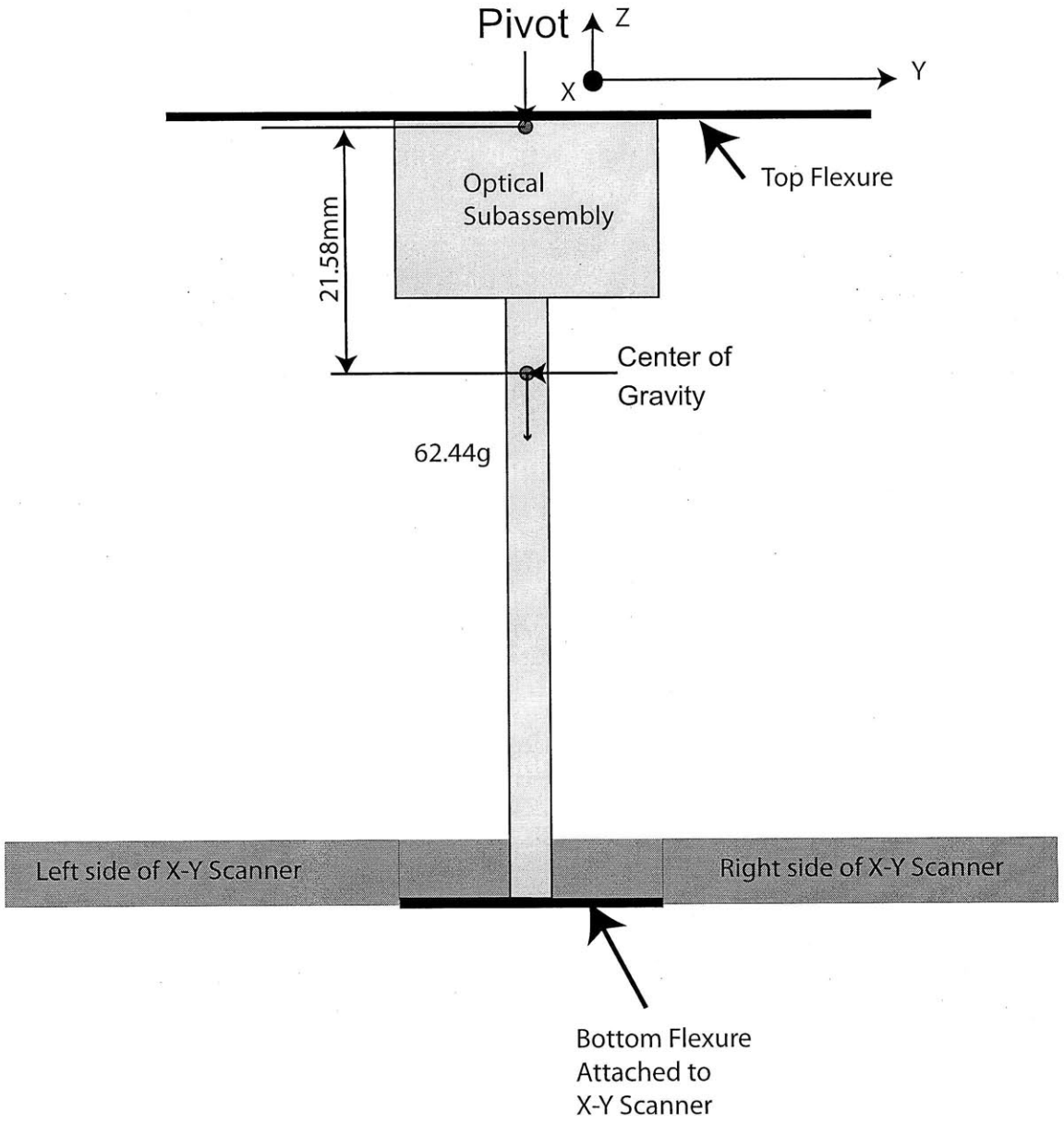

Figure 4-3: Flexure to allow tilt of the optical subassembly for tracking the cantilever.

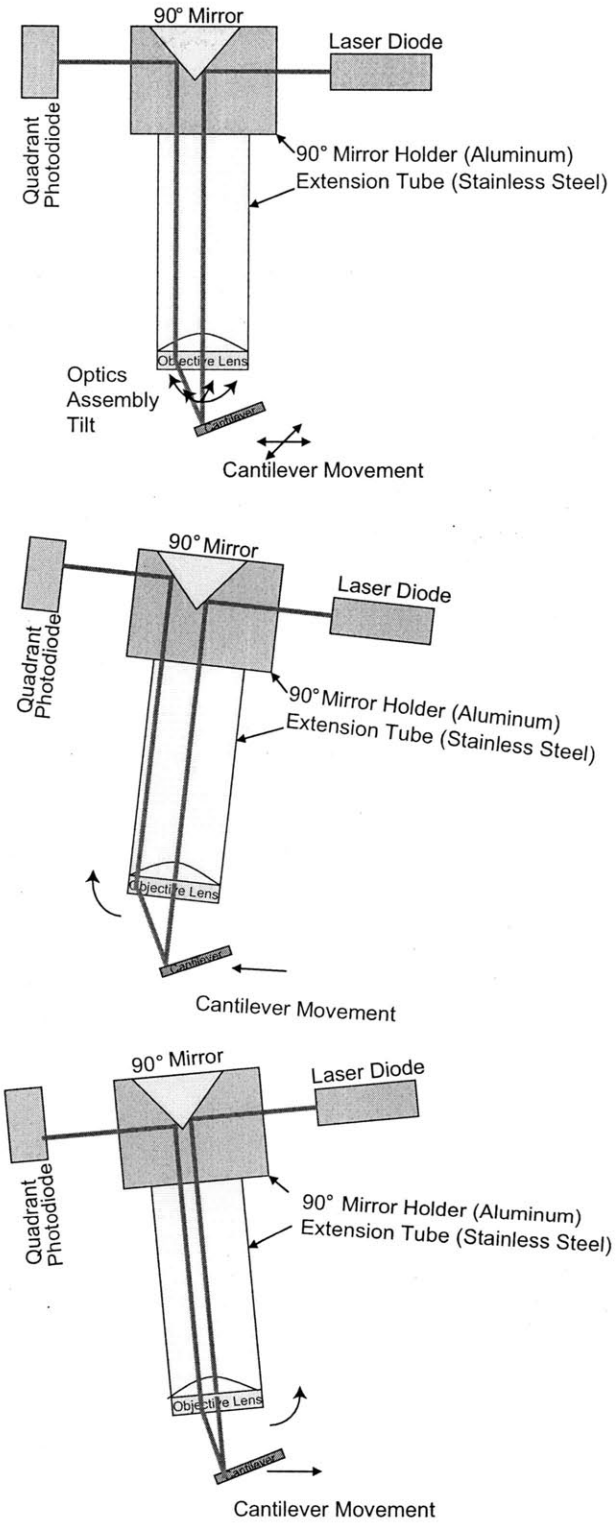

Figure 4-4: Laser landing on the cantilever as the optical subassembly tilts.

4.4 Summary

In this chapter, we described how the optical subassembly is connected to the X-Y scanner and how the optical subassembly is able to track the back of the cantilever as the cantilever is translating in the X and Y directions.

Chapter 5

Lever Method - Kinematics

5.1 Introduction

In this chapter, we describe our consideration for deciding the length of the tube that connects the optical subassembly and the X-Y scanner. The length of the tube will affect the magnitude of the errors that are produced as the optical subassembly tilts. The length of the tube will also affect the range of the initial adjustment of the laser spot when a new cantilever is mounted.

5.2 Offset Error Introduced as Optics Subassembly Tilts

In this section, simple geometry is used to predict the errors that will be generated when the optical subsystem is rotated about the center of the top flexure. The error that will be generated is a function of the ratio between the objective lens focal length and the pivot length of the optical subsystem. A detailed analysis will be given and graphs of the relationship between the length of the pivot to the objective lens, the working distance and the offset error in percentage of the width of the cantilever.

The length of the tube (e.g. 50mm) and the translation of the cantilever (i.e. 25 microns) forms the adjacent and opposite sides of a triangle. A smaller similar triangle has the working distance of the objective lens (i.e.2.91mm) and the offset of the laser spot as the adjacent and the opposite sides of the smaller triangle. To compute the offset, we multiply 25 microns (X-Y scanner range) with 2.91mm (i.e. working distance of the objective lens) and divide the result by 50mm (i.e. length of the tube). The example calculation for figure 5-1 is shown in the equation and computation below.

$$\begin{aligned} \text{Offset Error} &= \frac{\text{Range of scanner} \times \text{Working distance of the objective lens}}{\text{Length of the tube}} \\ &= \frac{25microns \times 2.91mm}{50mm} = 1.454 \text{ microns} \end{aligned}$$

From figure 5-1, we calculate that the offset error to be 1.454 mircons at the maximum range of the scanner (i.e. 25 microns in all directions from the center of the scanner).

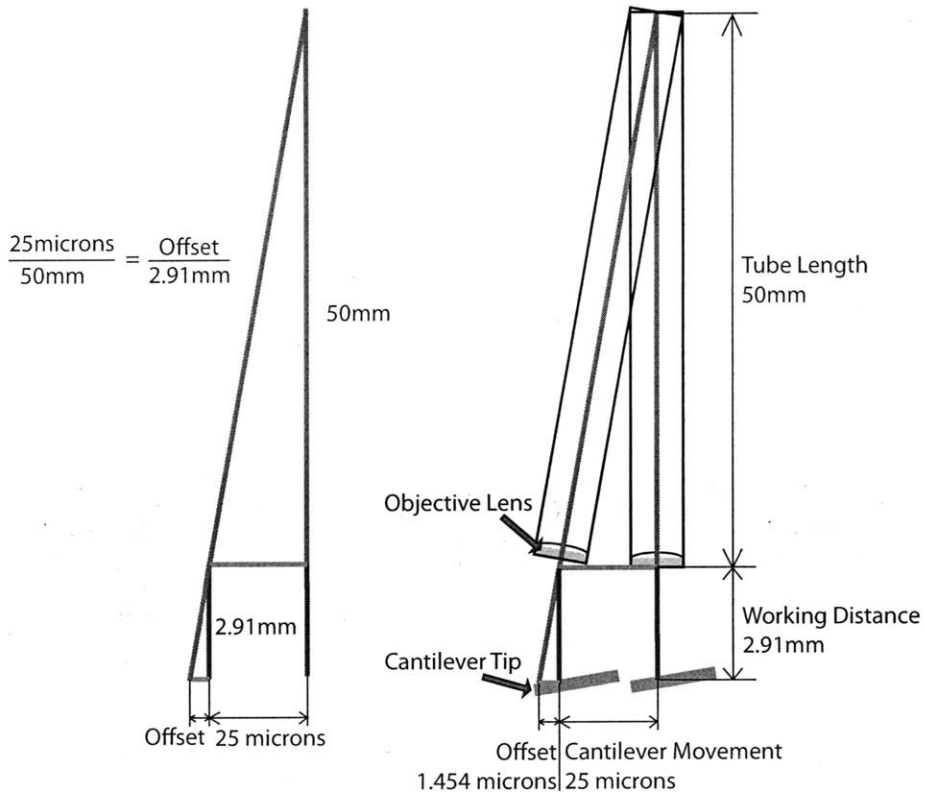

Figure 5-1: Geometry for calculating the offset error that the system has as the optics subassembly tilts.

Figure 5-2 is the computed error in degrees when the scanner moves from 0 microns to $\pm$ 25 microns in one direction. The X axis is the position along the 50 micron range and the Y axis is the error in degrees.

Figure 5-3 is a plot of the changes in the errors with respect to tube length and focal length. This allows us to select the optimum tube length and a suitable working distance of the lens. The computation for the tube length is shown in the next paragraph.

We set our error to be less than 7.5 percent of the width of the cantilever. Assuming the cantilever to be 10 microns, the offset error allowable will be 0.075 * 10 microns = 0.75 micron. The equation below shows the computation for the length of the tube.

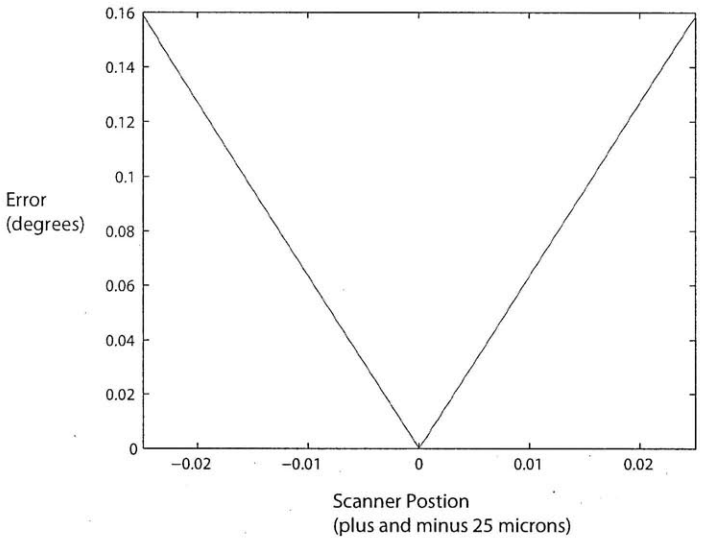

Figure 5-2: 2D graph of error versus scanner position (i.e. $\pm$ 25 microns).

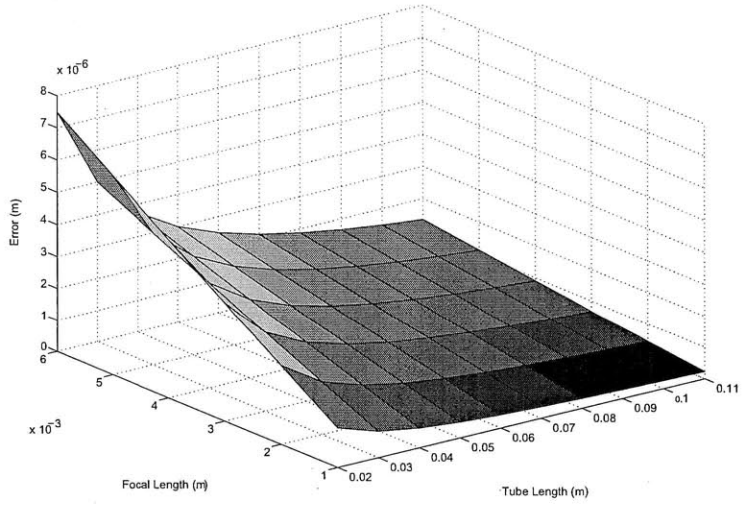

Figure 5-3: Errors computed with change in tube length and focal length.

$$\text{Tube length} = \frac{\text{Range of scanner} * \text{Working distance of objective lens}}{\text{Allowable offset error}}$$
$$= \frac{25microns * 2.91mm}{0.75microns} = 97mm \simeq 100mm$$

We selected a tube length of 100 mm based on the limit of 7.5 percent error that will be introduced.

5.3 Angular Error Introduced as Optics Subassembly Tilts

This section describes the geometry used to calculate the angular error. In addition to the offset error, there is an angular error that is introduced when the optical subassembly tilts. This error, however, can be eliminated with the built in lock-in amplifier built into the Anfatec controller.

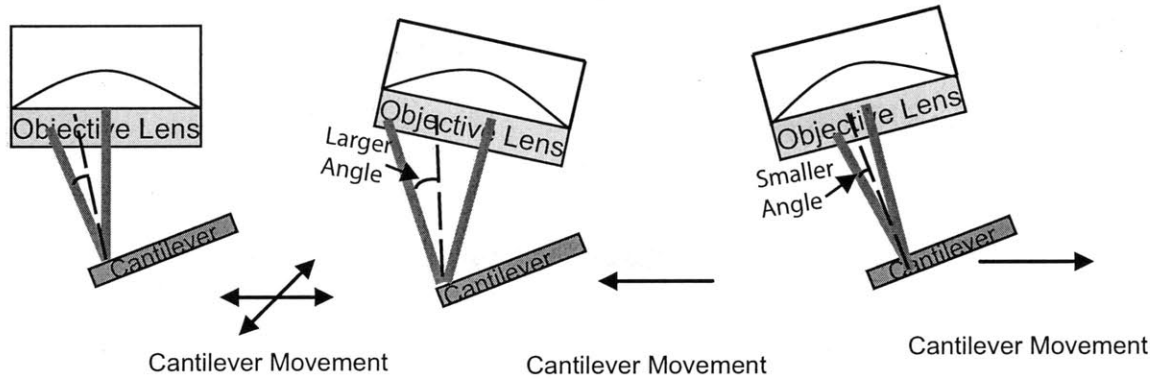

Figure 5-4: Changes in cantilever reflection angles as optics subassembly tilts.

As can be seen from figure 5-4, even when the cantilever is not tapping or oscillating, there will be a displacement recorded on the quadrant photodiode detector when the entire optics subassembly is tilted as the scanner and cantilever moves in the X and Y directions. The generated displacement on the quadrant photodiode detector due to the tilt of the optics subassembly instead of the oscillation of the cantilever can be taken out as the lock-in amplifier will only accept signals at the oscillation frequency of the cantilever. The lock-in amplifier method to overcome this tilt error is explained in detail in section 5.4.

5.4 Lock-in Amplifier to Eliminate Changes in Cantilever Angle when Optics Subassembly Tilt

A lock-in amplifier is essentially a narrow bandpass filter that allows only signal of a narrow passband region to be captured or measured (parameters measured are phase and amplitude). Figure 5-5 shows the Anfatec controller that hosts the lock-in amplifier.

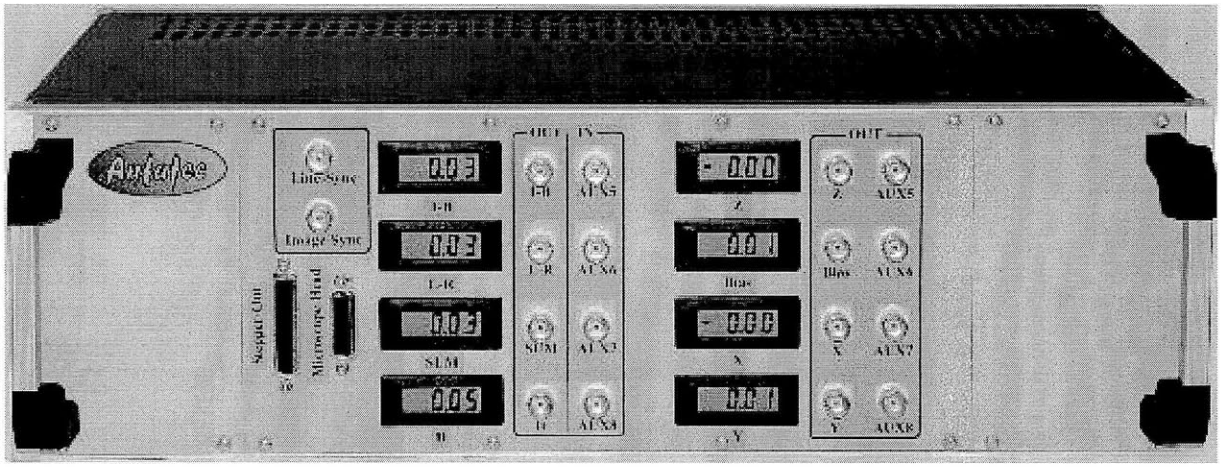

Figure 5-5: Photo of Anfatec controller with built-in lock-in amplifier.[11]

The frequency to lock into is set using the Anfatec SPM controller SXM software. This is accomplished by connecting the dither/tapping output of the Anfatec controller (i.e. oscillate the cantilever at a range of frequency) to the dither/tapping piezo and capturing the output of the top minus bottom output signal from the quadrant photodiode detector. This is clearly depicted in figure 5-6.

The Dynamic Non-Contact (i.e. tuning) window is selected to and run (i.e. the green round button at the top left corner) at a gain of 1 and a driving voltage of approximately 0.1 volt. A frequency sweep is carried out and the frequency that has the high amplitude is selected. Figure 5-7 shows a graph of the amplitude from a low frequency (i.e. 306611 Hz) to a high frequency (i.e. 311560 Hz). The frequency with

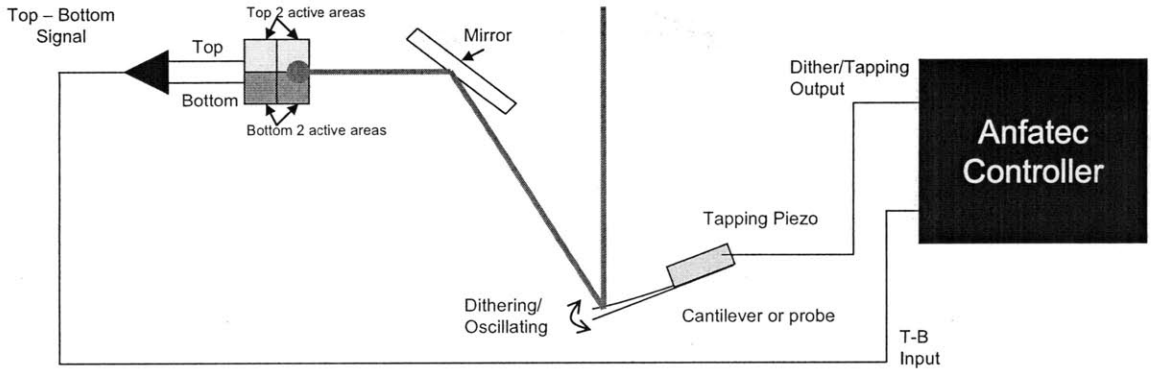

Figure 5-6: Diagram showing the connections between the Anfatec controller and the tapping piezos and quadrant photodiode detector for the tuning curve.

the highest amplitude (i.e. 310071 Hz) is selected as the lock-in frequency.

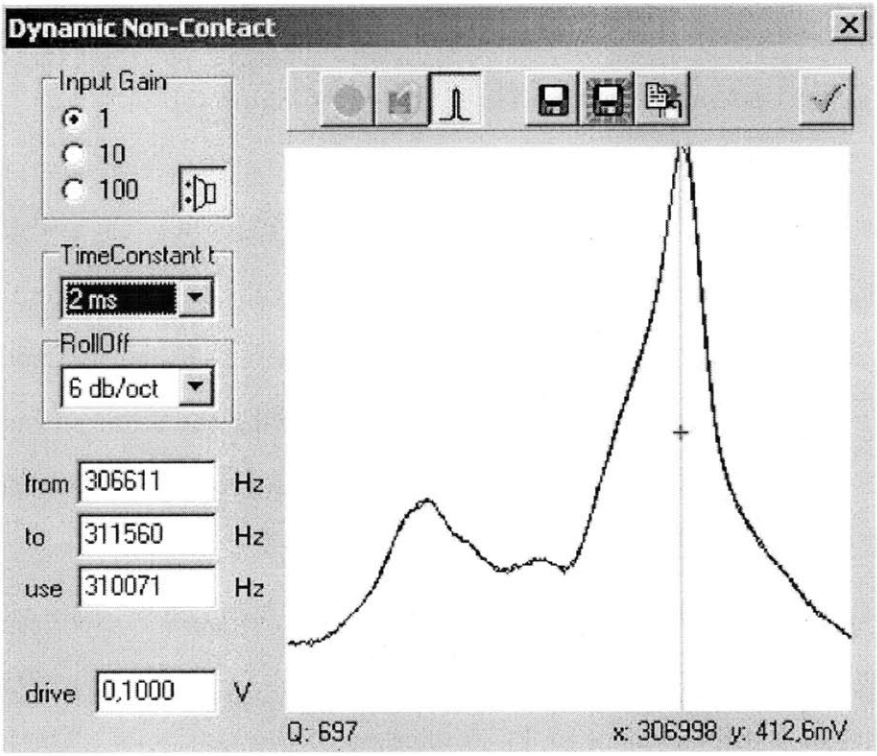

Figure 5-7: Tuning curve captured by the Anfatec controller SXM software.[11]

With the selected lock on frequency, we can extract only the amplitude of the top-minus-bottom signals from the quadrant photodiode detector with the same frequency. Any other change in amplitude at a different frequency will not be captured.

This will resolve the changes in output of the quadrant photodiode detector due to the tilt of the optics subassembly even when the cantilever is not tapping/dithering.

5.5 Fine Adjustment of Laser Spot during Initial Setup

This section describes the geometry for calculating the adjustable range of the optical subassembly and position of the laser spot during initial setup. In order to allow for the fine adjustment of the laser spot onto a cantilever tip that is newly mounted, we make use of our proposed top and a bottom flexures. These flexures are flexible enough for fine adjustment of the focal point of the objective lens so that the laser spot will fall on the cantilever tip. This is shown in figure 5-8.

Figure 5-9 shows the geometric calculations to determine the range of the laser focal point when we move the top flexure by 5mm. This time, the pivot point is at the center of the bottom flexure. The length of the tube is the adjacent side of the larger triangle. The top flexure is translated by 5mm and this is the opposite side of the larger triangle. The smaller triangle is formed with the adjacent side from the working distance of the objective lens and the fine adjustment range as the opposite side of the smaller triangle.

Using the ratio of the length of the tube to the distance between the center of the bottom flexure to the focal point, we determine that moving the top flexure by 5mm results in a displacement of 145.5 microns of the laser spot. This is shown in the equation below.

$$\begin{aligned} \text{Fine Adjustment Range} &= \frac{\text{Translation of top flexure} * \text{Working distance of lens}}{\text{Length of tube}} \\ &= \frac{5mm * 2.91mm}{100mm} = 145.5microns \end{aligned}$$

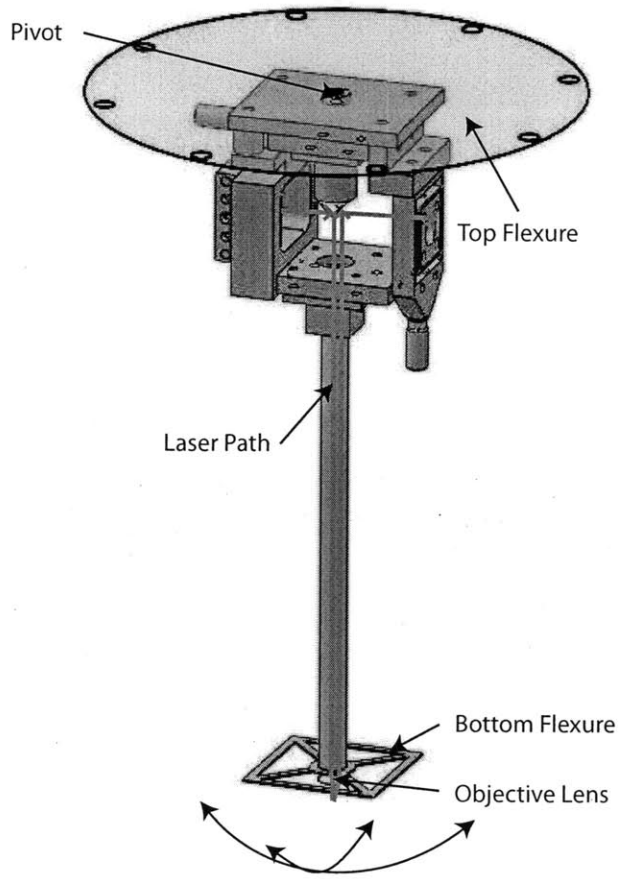

Figure 5-8: Top and bottom flexure to allow optical subassembly to tilt and allow fine adjustment of the laser spot.

Therefore, the laser spot will be adjustable within the range of 145.5 microns in the X and Y directions.

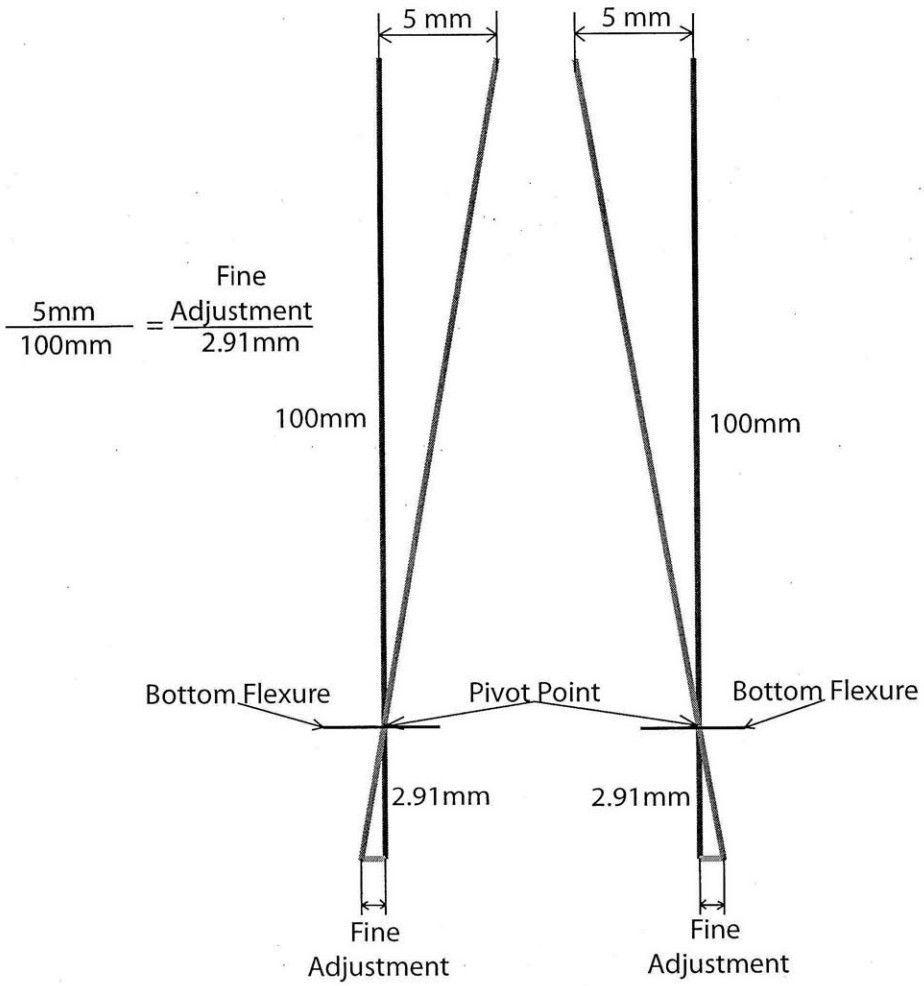

Figure 5-9: Geometry for calculating the range that the system can have for initial adjustment.

Figure 5-10 is a graph that shows the effect the ratio of the tube length to the focal length has on the range for initial adjustment as described above. The front axis is tube length in meters and the left axis is the focal length of the objective lens. The vertical axis is the adjustment range in meters.

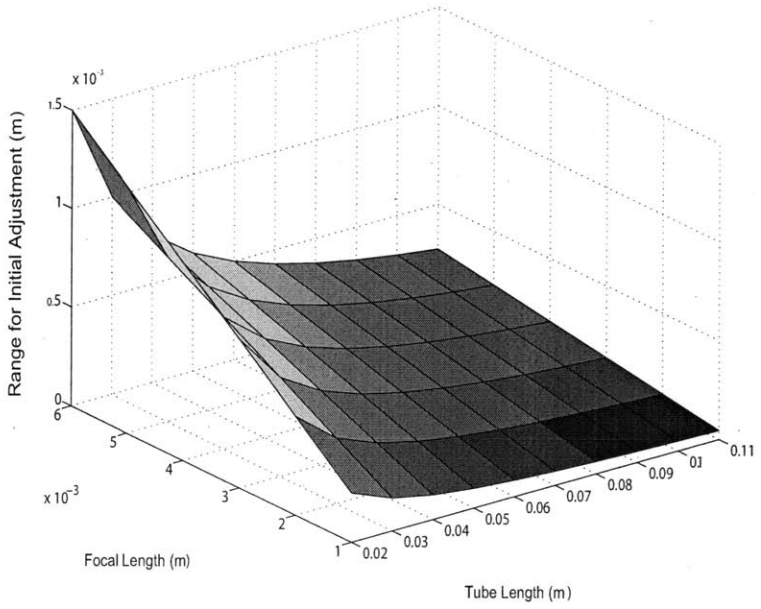

Figure 5-10: Range for initial adjustment of the focus point with a translation of 5mm at the top translation stage.

5.6 Mass of Optical Subassembly on Scanner Central Stage

In this section, we make use of the mechanical advantage of the lever method to reduce the effect of the mass of the optical subassembly on the X-Y scanner with simple geometry. It is desirable to move the optical subassembly as near to the pivot (i.e. center of the top flexure) as possible to make use of mechanical advantage of the lever method.

Figure 5-11 shows the calculations that gives the effective mass of the optics subassembly at the X-Y scanner. The theoretical weight of the optics subassembly is 62.44g and the effective mass at the X-Y scanner is 2.907g. This mass is significantly lower than if the optics components were mounted on the central stage.

$$\text{Effective Mass} = \frac{\text{Distance of pivot to center of gravity}^2 * \text{Mass of optical subassembly}}{\text{Length of tube}^2}$$

$$= \frac{21.58^2 mm * 62.44 grams}{100^2 mm} = 2.907 grams$$

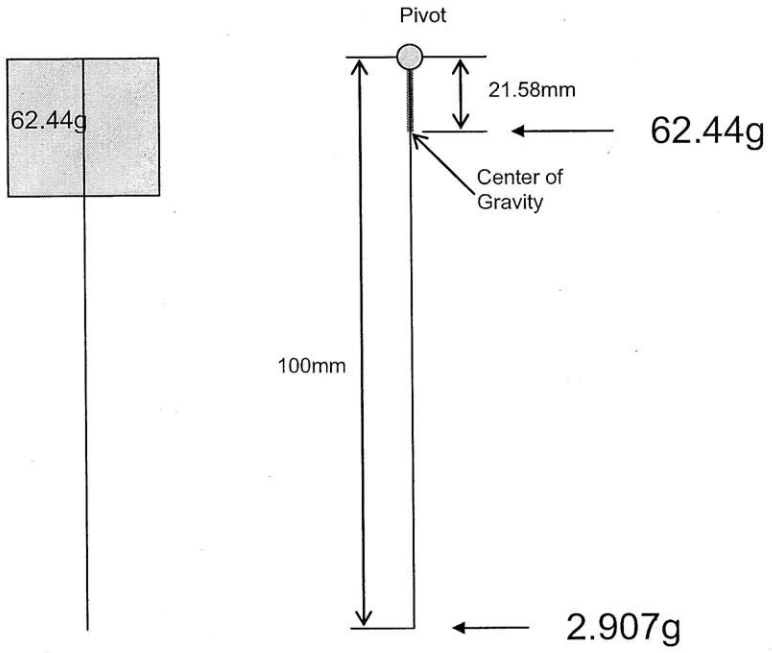

Figure 5-11: Calculation of effective weight on the central stage.

5.7 Summary

In this chapter, we described the kinematics and geometry of the lever method in detail. Due to the tilt of the optical subassembly, an offset error and an angular error is introduced. The offset error can be reduced by extending the length of the tube or

reducing the working distance of the lens. The angular error can be eliminated with the lock-in amplifier of the Anfatec controller. We also used geometry to calculate the range for the initial adjustment of the position of the laser spot. Finally, we make use of the mechanical advantage of the lever method to reduce the effective mass of the optical subassembly on the X-Y scanner.

Chapter 6

Lever Method - Dynamics

6.1 Introduction

In this chapter, we present the simulations of the stiffnesses and the resonance of the top flexure, bottom flexure and the optical subassembly integrated with the X-Y scanner. By simulating the stiffnesses of the flexures, we can evaluate and optimize the sizing of the flexures so that the optical subassembly will not significantly affect the dynamics of the X-Y scanner. This chapter also describes our design considerations and how we assign the stiffnesses for all 6 degrees of freedom of the optical subassembly.

6.2 Relationship between Spring Constant and Natural Frequency

The mass and spring constant or stiffness of the optical subassembly has a significant effect on the resonance of the entire assembly. Thus, we can assign stiffnesses appropriately to increase the resonance of the optical subassembly. We want the stiffness to be as high as possible to increase the resonance of the optical subassembly. It is

also preferred that the mass be reduced as much as possible. The resonant frequency of for a simple mass and spring system is governed by

$$\omega = \sqrt{\frac{k}{m}} \tag{6.1}$$

where ω is the angular frequency in rad/s, k is the stiffness in N/m and m is the mass in kg.

6.3 Stiffness and Resonance of Top Flexure

This section discusses the simulations of the stiffnesses of the top flexure in all 6 degrees of freedom. The specifications we assign for the stiffnesses are also presented.

We decided to use a disc for the top flexure due to the ease of manufacturing so that we can quickly test our concept. The flexure is shown in figure 6-1. There are eight holes at the periphery of the disc flexure that is to be bolted to ground.

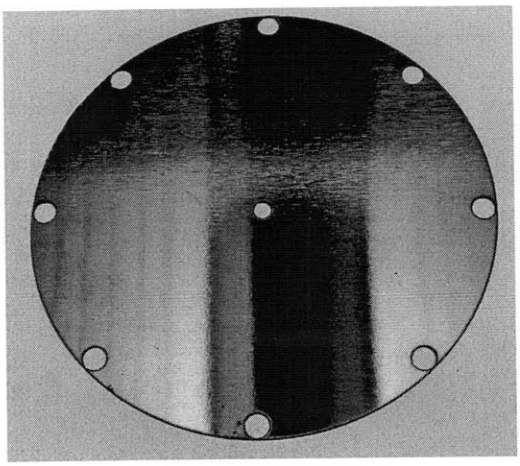

Figure 6-1: Photo of the top flexure.

We want the top flexure to have a low stiffness for θ_x and θ_y while maintaining high stiffness for X, Y, Z and θ_z directions. This is because we only want the top flexure to allow the optical subassembly to rotate about the X and Y axis and be

rigid in all other axes.

We assign the ratio of Z stiffness to the θ_x and θ_y as follows:

Ratio of Z stiffness to θ_x or θ_y stiffness	$\geq 10:1$

The stiffnesses of the first top flexure is simulated using COSMOSWorks. Figures 6-2, 6-3 and 6-5 are simulations of the top flexure to obtain the stiffnesses in the Z, θ_x and θ_z respectively. The stiffness of θ_y is the same as the stiffness of θ_x due to symmetry. The stiffnesses for the X and Y directions are not included because they are greater than 100N/mm. In all simulations, the disc is fixed at the faces of the 8 holes at the circumference. The material properties we use for simulations is tabulated in section 7.3.

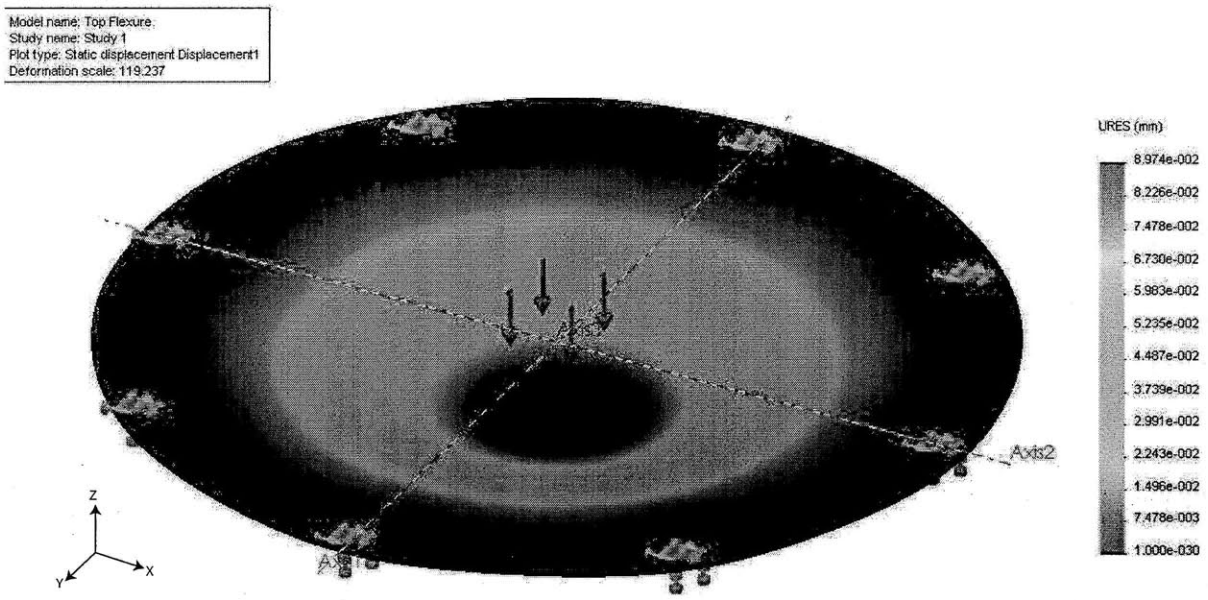

Figure 6-2: COSMOSWorks simulation of top flexure for Z with a force of 1N.

Figure 6-2 is a COSMOSWorks simulation of the Z axis stiffness. The eight holes at the circumference of the disc is grounded and a force of 1N is applied at the center of the disc in the Z direction. The force is divided by the maximum deflection shown on the simulation to determine the stiffness in the Z direction. The maximum Z displacement is 0.089mm and taking the reciprocal of the maximum Z displacement gives us a Z stiffness of 11.31N/mm.

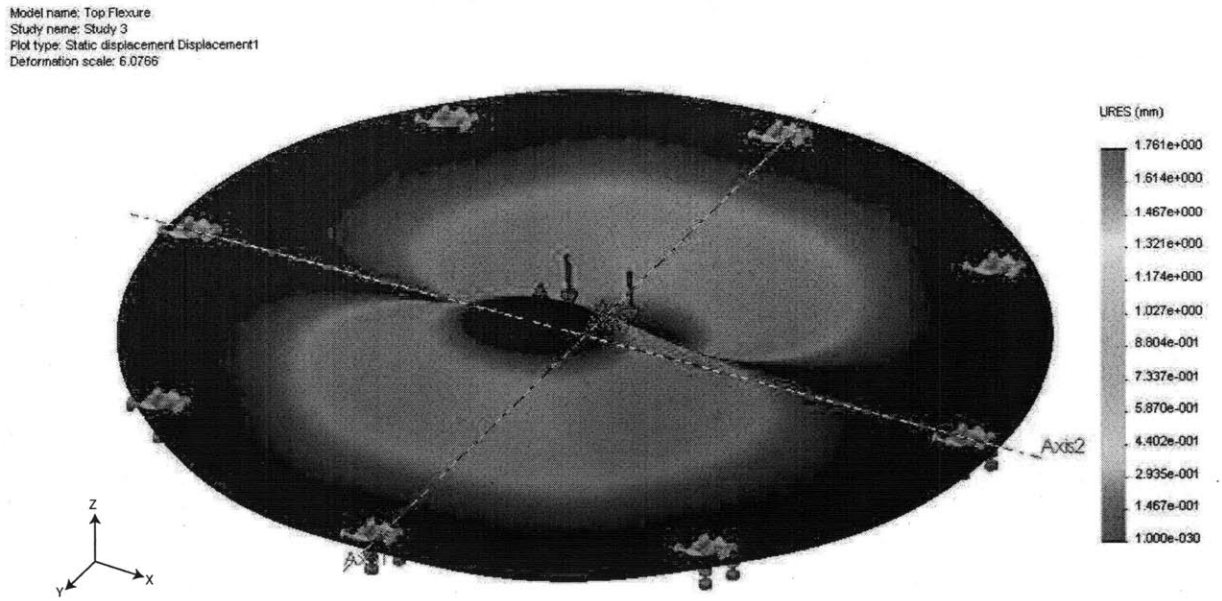

Figure 6-3: COSMOSWorks simulation of top flexure for θ_x with a torque of 1Nm.

Figures 6-3 is COSMOSWorks simulation of the θ_x stiffness. The eight holes at the circumference of the disc is grounded and a torque of 1Nm is applied at the center of the disc and about the X axis.

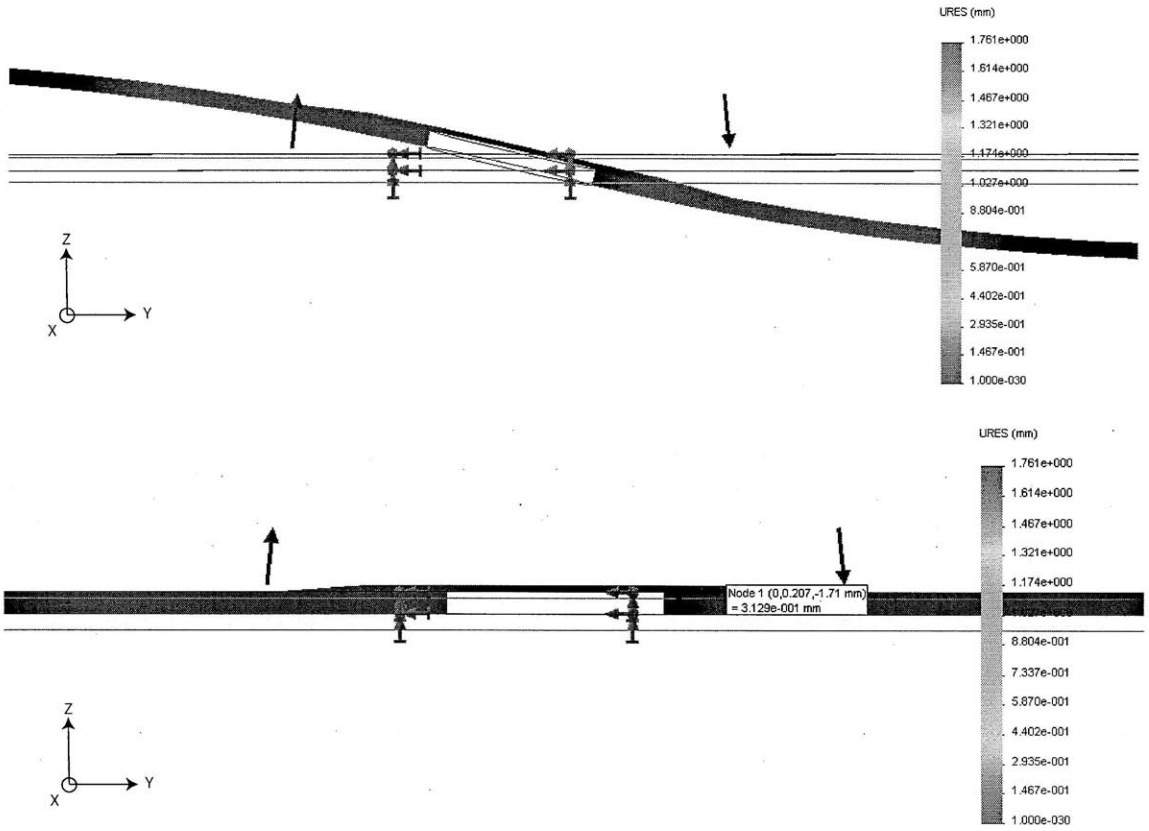

Figure 6-4: Section of simulation of top flexure for θ_x with a torque of 1Nm.

Figure 6-4 is a zoomed-in section of the top flexure across the Y axis. The deformation of the top flexure is shown in the figure at the top. The lower figure displays the value of the deformation (i.e. 0.3129mm) at a coordinate of -1.71mm along the Y axis. The angle formed from this deformation is the arctangent of 0.3129 divided by 1.71. The angle formed when the flexure deflect from 1Nm of torque is 0.18 radians. Taking the reciprocal of the 0.18 radians gives a stiffness of 5.53Nm/rad.

The simulation of the stiffness about the Y axis (i.e. θ_y) is the same as the simulation of the stiffness about the X axis due to symmetry.

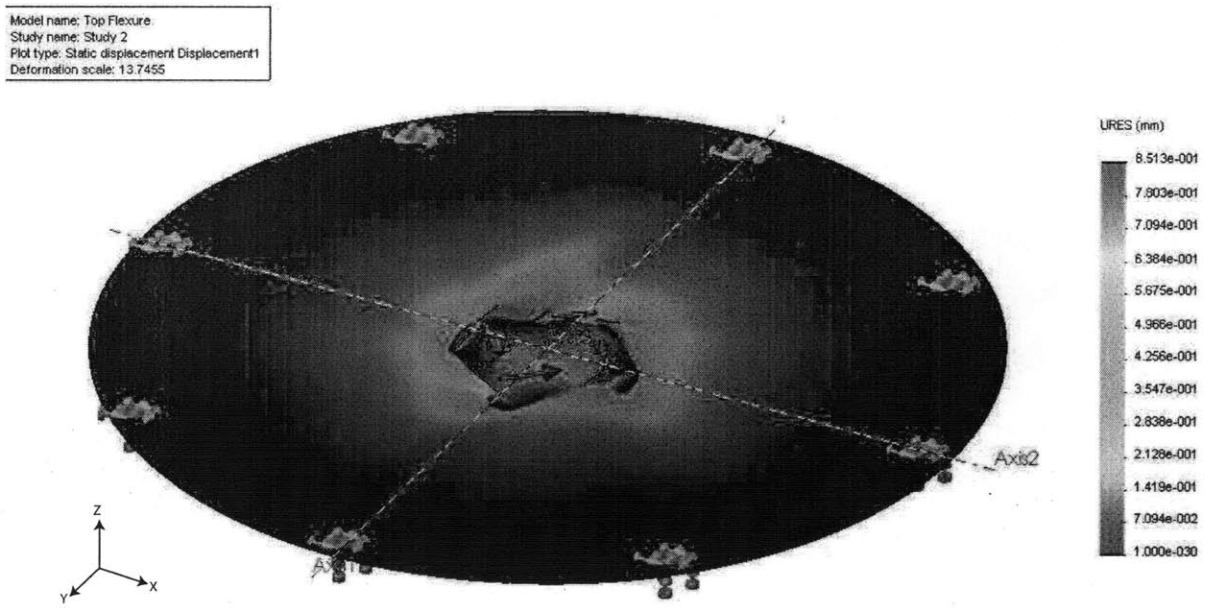

Figure 6-5: COSMOSWorks simulation of top flexure for θ_z with a torque of 1Nm.

Figure 6-5 is a COSMOSWorks simulation of the θ_z stiffness. The eight holes at the circumference of the disc is grounded and a torque of 1Nm is applied at the center of the disc and about the Z axis.

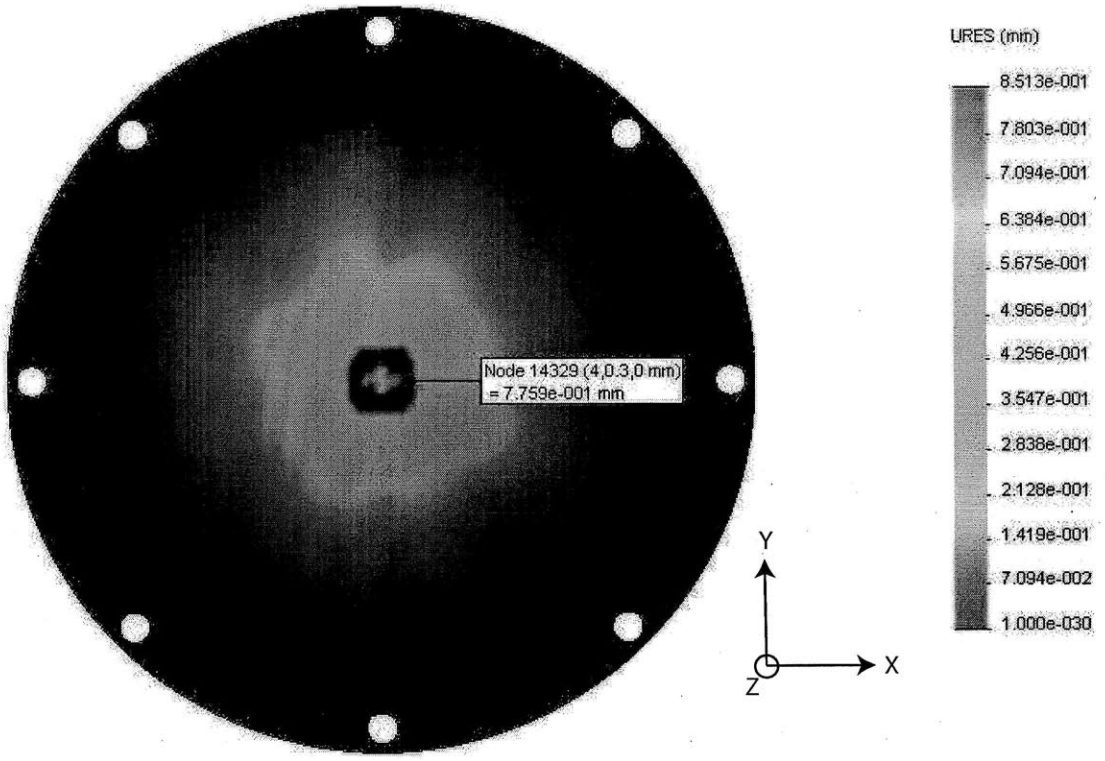

Figure 6-6: Section of simulation of top flexure for θ_z with a torque of 1Nm.

Figure 6-6 is a view from the top of the top flexure. Figure 6-6 displays the value of the deformation (i.e. 0.7759mm) at a coordinate of 4mm along the X axis. The angle formed from this deformation is the arctangent of 0.7759 divided by 4. The angle formed when the flexure deflect from 1Nm of torque is 0.19 radians. Taking the reciprocal of the 0.19 radians gives a stiffness of 5.23Nm/rad.

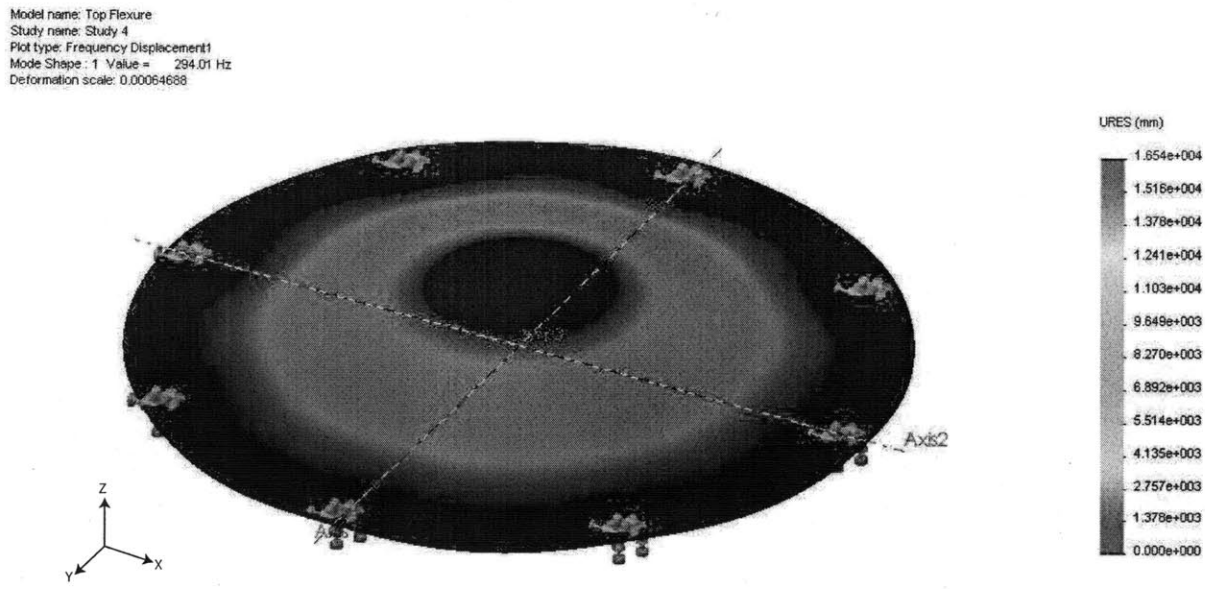

Figure 6-7: COSMOSWorks simulation of top flexure for resonance in the Z direction.

Figure 6-7 is a simulation of the Z resonant frequency of the top disc flexure. Figure 6-7 has no forces applied to the disc and are fixed with the faces of the 8 holes at the circumference of the disc. From the simulation, it can be seen that the resonance in the Z direction of the disc is only 294.01Hz. That is not desirable when the scanner is scanning or moving at 1kHz. Due to the top disc flexures' poor Z resonance, the top disc flexure is not suitable for our application. We used it because it can be fabricated easily to quickly test our prototype.

From the top disc flexure stiffnesses in Table 6.1, we can see that the stiffness of the top disc flexure in the Z direction is only about 11.31 N/mm. This does not satisfy our initial specifications but we decided to test the integrated optical subassembly and X-Y scanner.

Table 6.1: Stiffness of top flexure

Direction	Top Flexure Stiffness
X	$>100\frac{N}{mm}$
Y	$>100\frac{N}{mm}$
Z	$11.31\frac{N}{mm}$
θ_x	$5.53\frac{Nm}{rad}$
θ_y	$5.53\frac{Nm}{rad}$
θ_z	$5.23\frac{Nm}{rad}$

6.4 Stiffness and Resonance of Bottom Flexure

This section discusses the simulations of the stiffnesses of the bottom flexure in all 6 degrees of freedom. The specifications we assign for the stiffnesses is also presented.

We decided to use a cross layout for the bottom flexure for easy of manufacture so that we can test our concept quickly. This is shown in figure 6-8. The four outer sides of the bottom flexure are to be epoxied the central stage of the X-Y scanner.

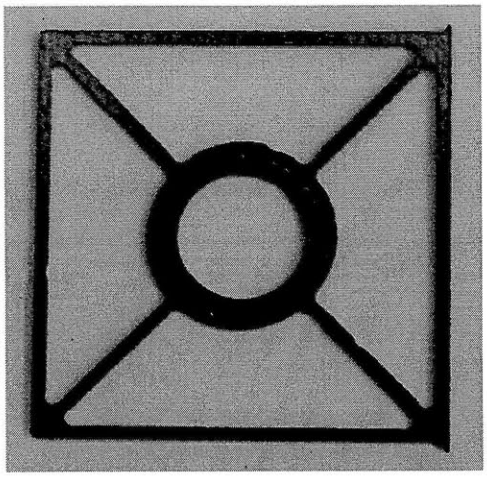

Figure 6-8: Photo of the bottom flexure.

For the bottom flexure, we want it to allow rotation about the X and Y axis and prevent rotation about the Z axis.

We assign the ratio of θ_z stiffness to the θ_x and θ_y as follows:

Ratio of θ_z stiffness to θ_x or θ_y stiffness	$\geq 10:1$

We will now discuss the simulation results for the bottom flexure. Figures 6-9, 6-10, 6-11 and 6-13 are simulations for the bottom flexure in the X, Z, θ_x and θ_z respectively. The stiffness of the Y direction is the same as the stiffness for the X direction due to symmetry. The flexure is grounded at the 4 outer faces as shown in the figures. For the X and Z direction simulation, a force of 1N is applied to the center of the flexure. A torque of 1Nm is applied to the center of the flexure to compute the angular stiffnesses about the Z and X axis (i.e. θ_z and θ_x). To apply the torque at the center of the flexure, a rectangular plate is added to the circular ring in the center. The torque is applied to the face of the added plate. The material properties we use for simulations is tabulated in section 7.3.

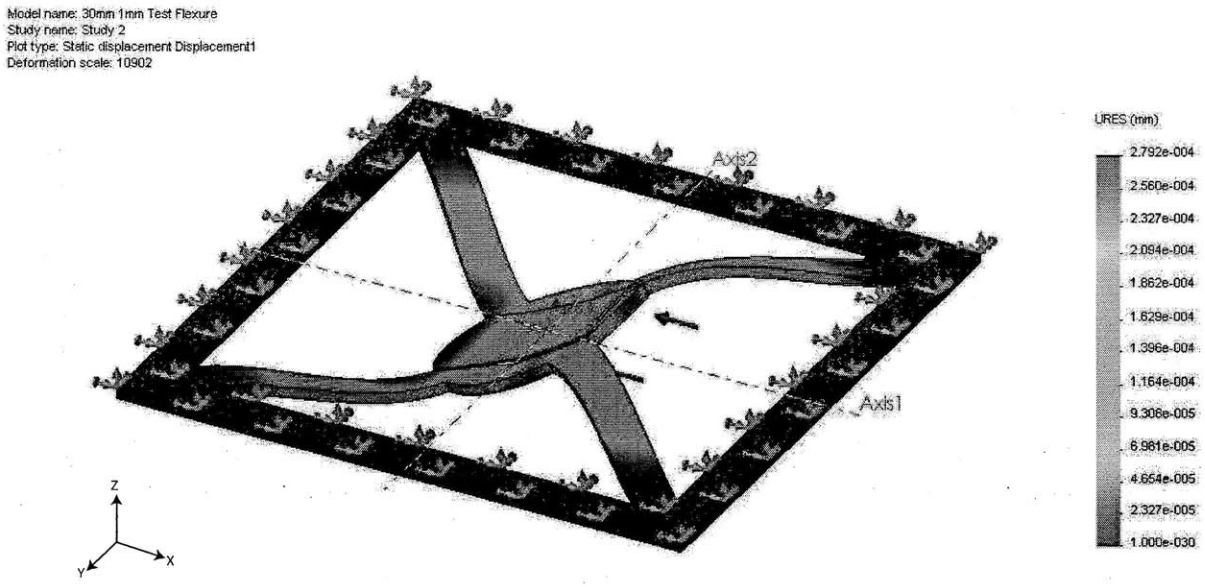

Figure 6-9: COSMOSWorks simulation of bottom flexure for X with a force of 1N.

Figure 6-9 is a COSMOSWorks simulation of the X axis stiffness. The four sides of the flexure is grounded and a force of 1N is applied at the center in the X direction. The force is divided by the maximum deflection shown on the simulation to determine the stiffness in the X direction. The maximum X displacement is 0.0002792mm and taking the reciprocal of the maximum X displacement gives us a X stiffness of greater than 100N/mm.

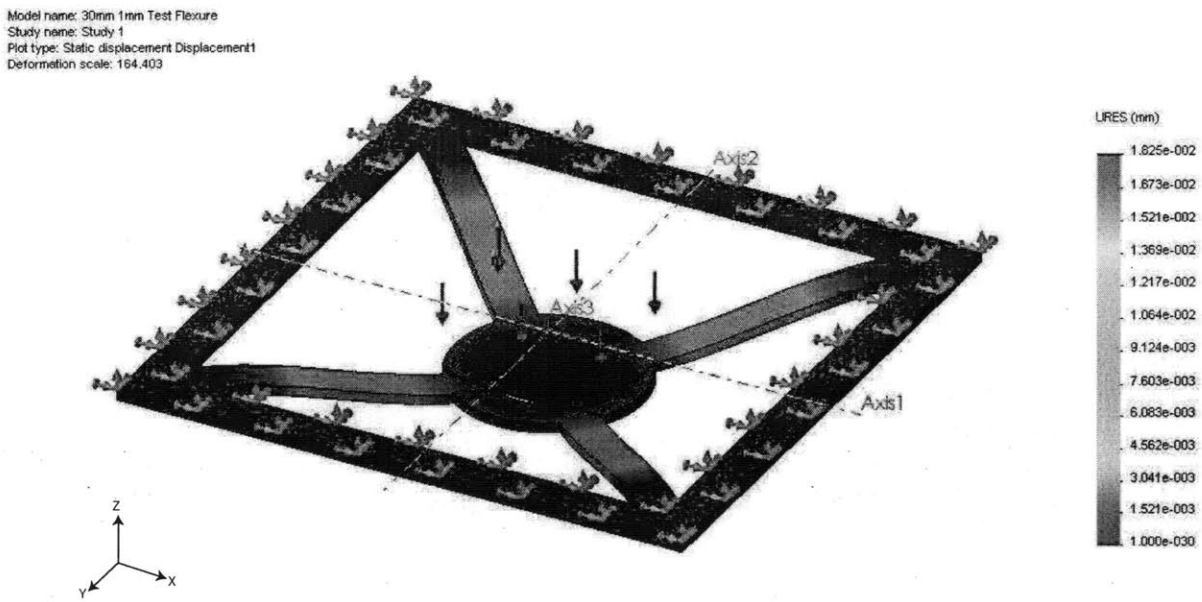

Figure 6-10: COSMOSWorks simulation of bottom flexure for Z with a force of 1N.

Figure 6-10 is a COSMOSWorks simulation of the Z axis stiffness. The four sides of the flexure is grounded and a force of 1N is applied at the center in the Z direction. The force is divided by the maximum deflection shown on the simulation to determine the stiffness in the Z direction. The maximum Z displacement is 0.01825mm and taking the reciprocal of the maximum Z displacement gives us a Z stiffness of 54.8N/mm.

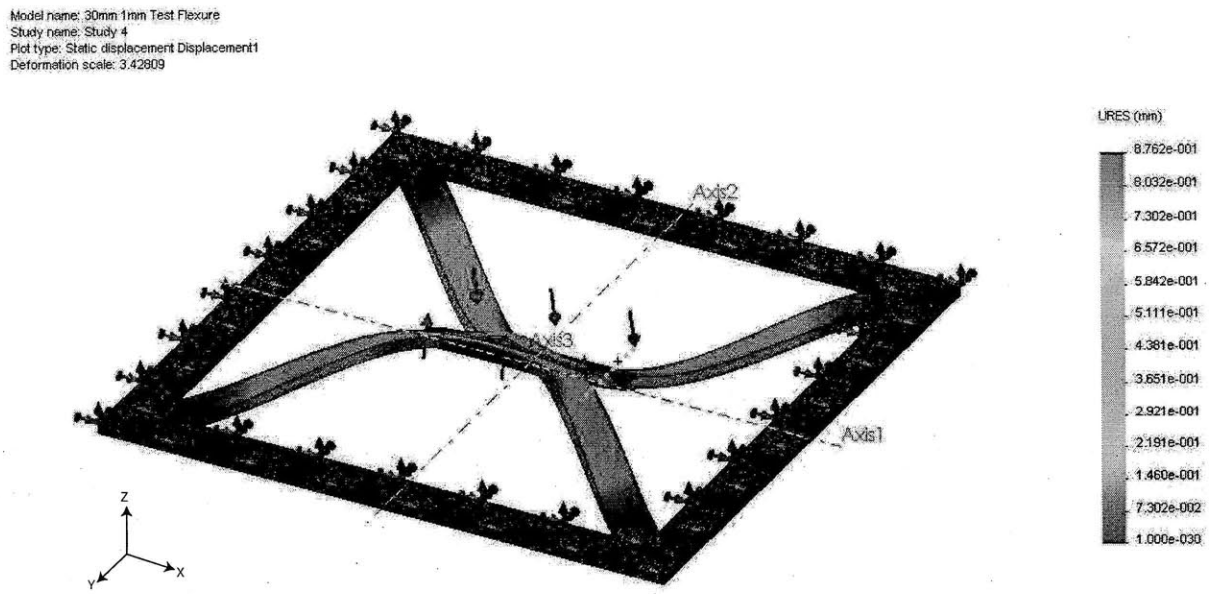

Figure 6-11: COSMOSWorks simulation of bottom flexure for θ_x with a torque of 1Nm.

Figures 6-11 is COSMOSWorks simulation of the θ_x stiffness. The four sides of the flexure is grounded and a torque of 1Nm is applied about the center about the X axis.

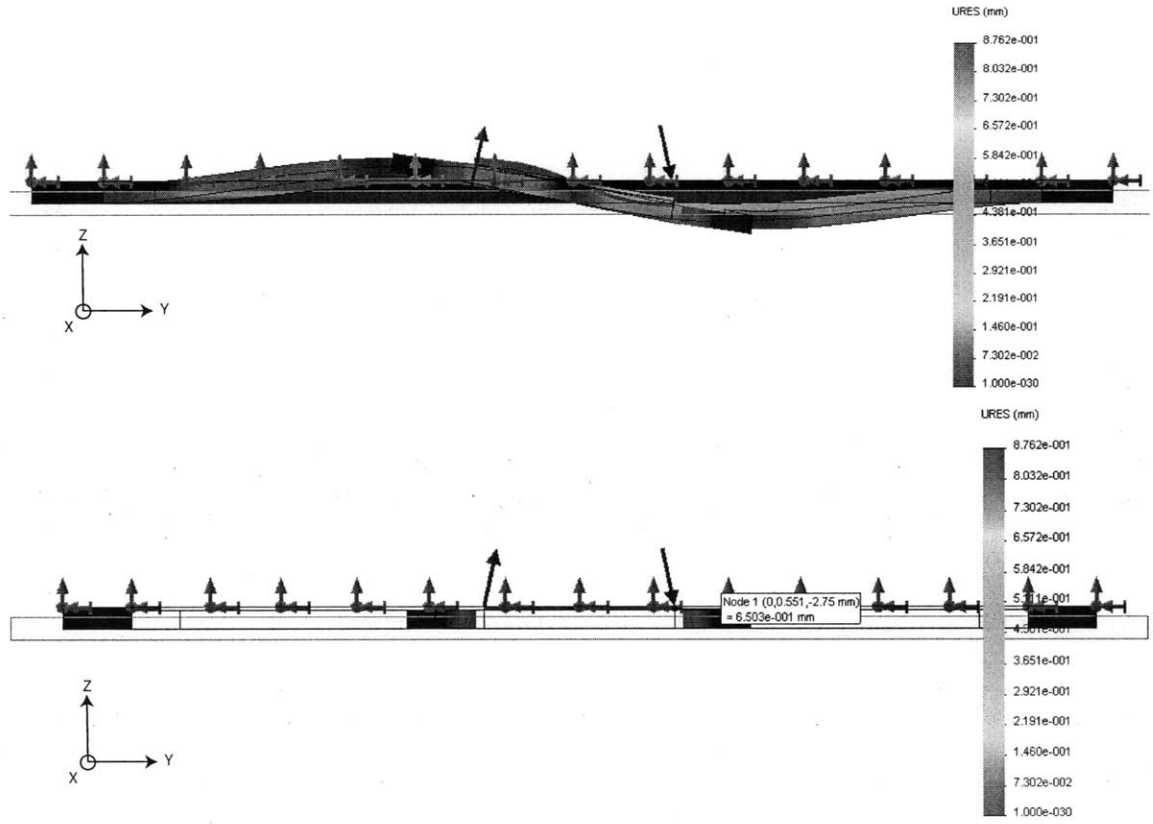

Figure 6-12: Section of simulation of bottom flexure for θ_x with a torque of 1Nm.

Figure 6-12 is a zoomed-in section of the bottom flexure across the Y axis. The deformation of the bottom flexure is shown in the figure at the top. The lower figure displays the value of the deformation (i.e. 0.6503mm) at a coordinate of -2.75mm along the Y axis. The angle formed from this deformation is the arctangent of 0.3129 divided by 1.71. The angle formed when the flexure deflect from 1Nm of torque is 0.232 radians. Taking the reciprocal of the 0.18 radians gives a stiffness of 4.31Nm/rad.

The simulation of the stiffness about the Y axis (i.e. θ_y) is the same as the simulation of the stiffness about the X axis due to symmetry.

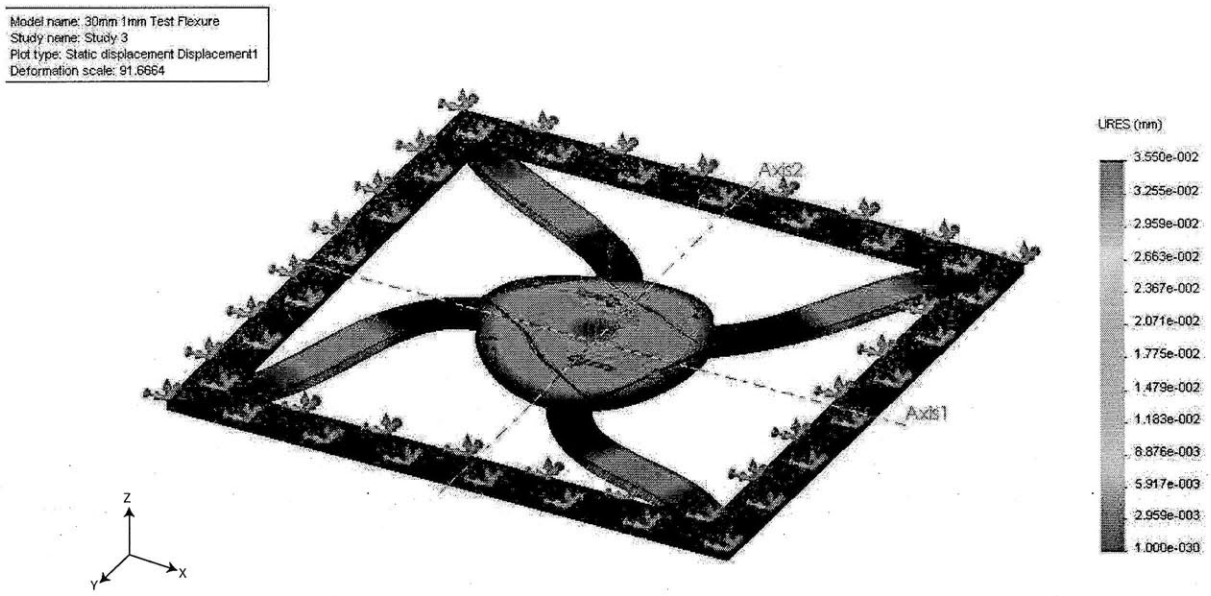

Figure 6-13: COSMOSWorks simulation of bottom flexure for θ_z with a torque of 1Nm.

Figure 6-13 is a COSMOSWorks simulation of the θ_z stiffness.The four sides of the flexure is grounded and a torque of 1Nm is applied at the center about the Z axis.

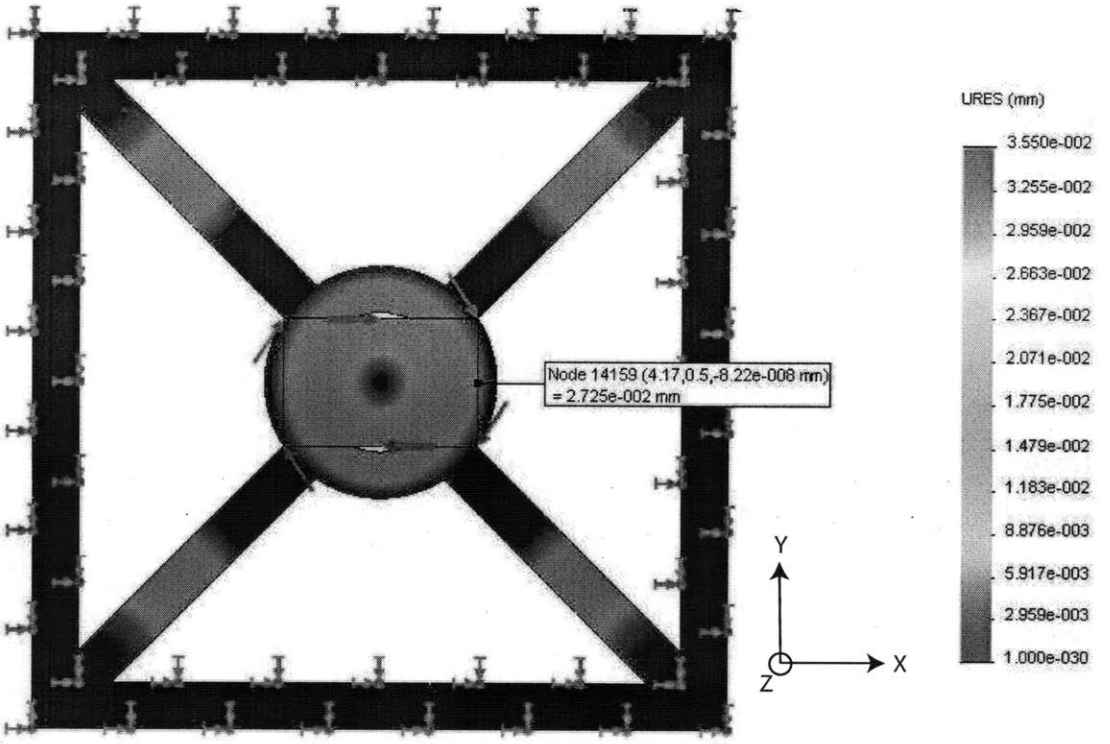

Figure 6-14: Section of simulation of bottom flexure for θ_z with a torque of 1Nm.

Figure 6-14 is a view from the top of the bottom flexure. Figure 6-14 displays the value of the deformation (i.e. 0.02725mm) at a coordinate of 4.17mm along the X axis. The angle formed from this deformation is the arctangent of 0.02725 divided by 4.17. The angle formed when the flexure deflect from 1Nm of torque is 0.0065 radians. Taking the reciprocal of the 0.0065 radians gives a stiffness of 153Nm/rad.

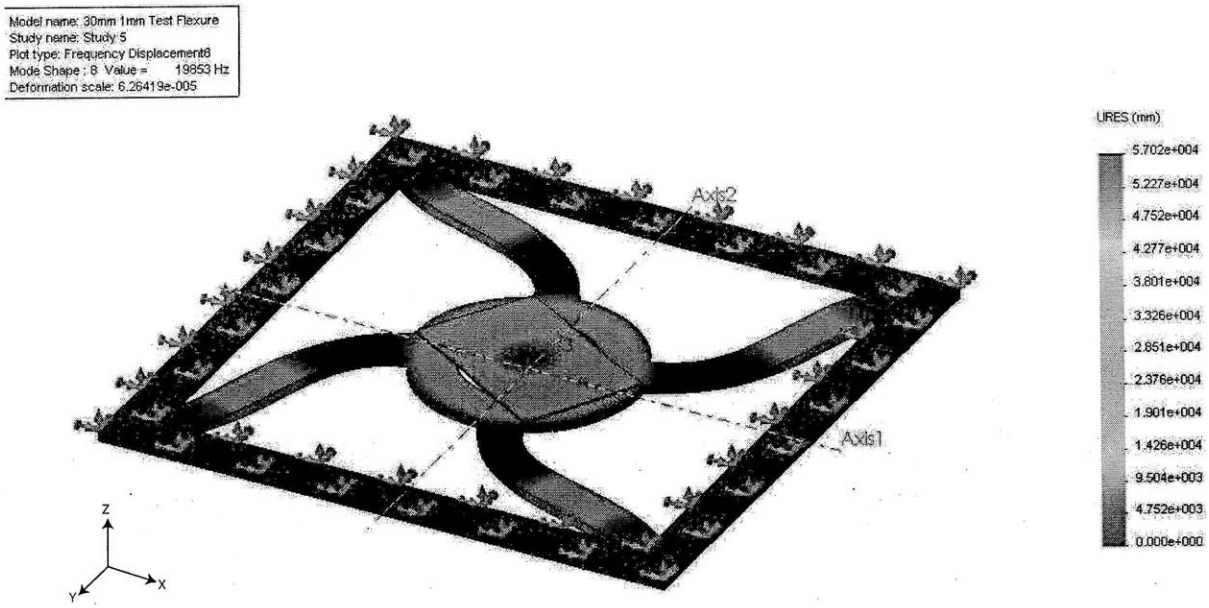

Figure 6-15: COSMOSWorks simulation of bottom flexure for resonance in the θ_z direction.

Figure 6-15 is a simulation of the resonance modes of the bottom flexure. Figure 6-15 has no forces applied to the flexure and is fixed with the faces of 4 outer sides. From the simulation, it can be seen that the resonance of the flexure is 19853Hz. The high θ_z resonance will help in increasing the θ_z resonance when the flexure in bonded to the optical subassembly.

Table 6.2 lists the stiffnesses of the bottom flexure in all 6 degree of freedom. The values are calculated from simulations in COSMOSWorks and are shown in figures 6-9, 6-10, 6-11 and 6-13. From the stiffness estimated with COSMOSWorks, it can be seen that the this bottom flexure satisfy our requirements of high θ_z stiffness to θ_x and θ_y stiffnesses. The high stiffness in θ_z will also increase the resonance of the flexure about the Z axis (i.e. θ_z).

Table 6.2: Stiffness of bottom flexure

Direction	Bottom Flexure Stiffness
X	$>100\frac{N}{mm}$
Y	$>100\frac{N}{mm}$
Z	$54.80\frac{N}{mm}$
θ_x	$4.31\frac{Nm}{rad}$
θ_y	$4.31\frac{Nm}{rad}$
θ_z	$153.00\frac{Nm}{rad}$

6.5 Stiffness and Resonance of Integrated Optical Subassembly and X-Y Scanner

After evaluating the stiffnesses and resonance of the top and bottom flexure, we simulate the stiffnesses and frequencies of resonance of the optical subassembly (i.e. top flexure, bottom flexure, tube and optical components) integrated with the X-Y scanner.

The optics components (i.e. 90 ° mirror, objective lens, laser diode and photodiode detector sensor) is not included into the simulation to simplify the model so that computation time can be reduced.

We want the resonance of the integrated optical subassembly and the X-Y scanner to be as high as possible. This high resonance will ensure that the optical subassembly will not affect the dynamics of the X-Y scanner.

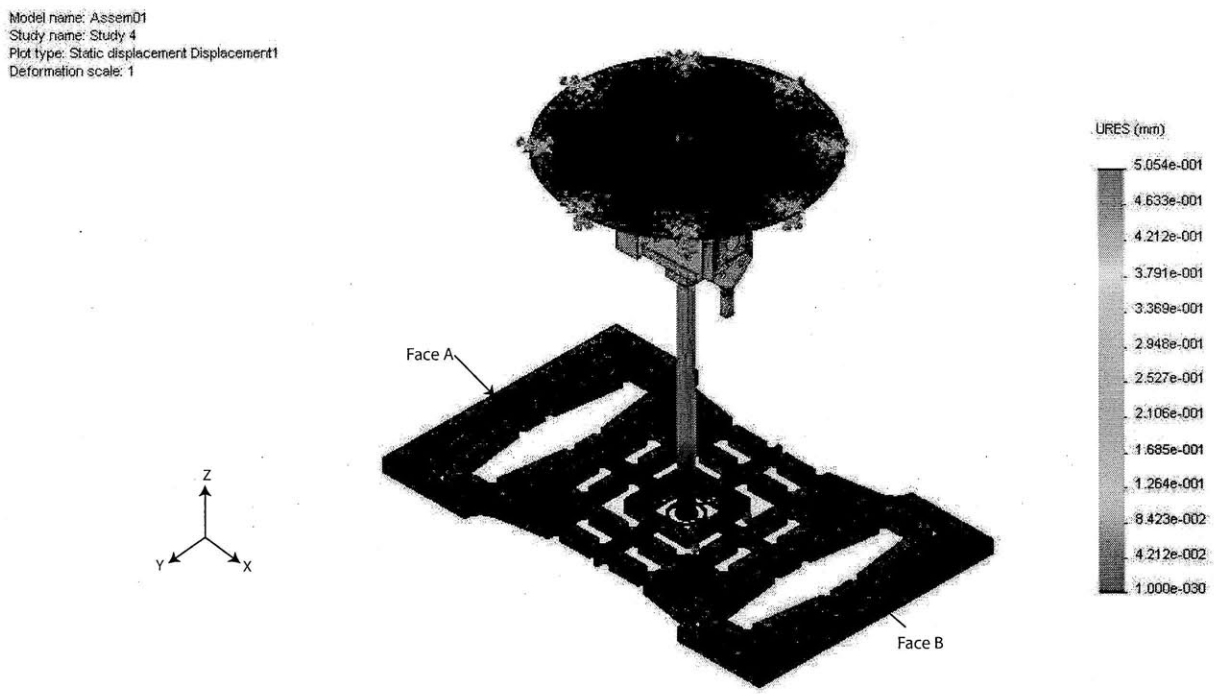

Figure 6-16: COSMOSWorks simulation of optics subassembly for X with a force of 1N.

Figure 6-16 is a simulation of the X stiffness of the integrated assembly. The entire system was simulated assuming the 8 holes at the circumference of the top flexure and faces A and B are fixed. Taking the maximum displacement (i.e. 0.5054mm) and then the reciprocal of the maximum X displacement, we found that the X stiffness is approximately 2N/mm. The Y axis stiffness is also the same due to symmetry.

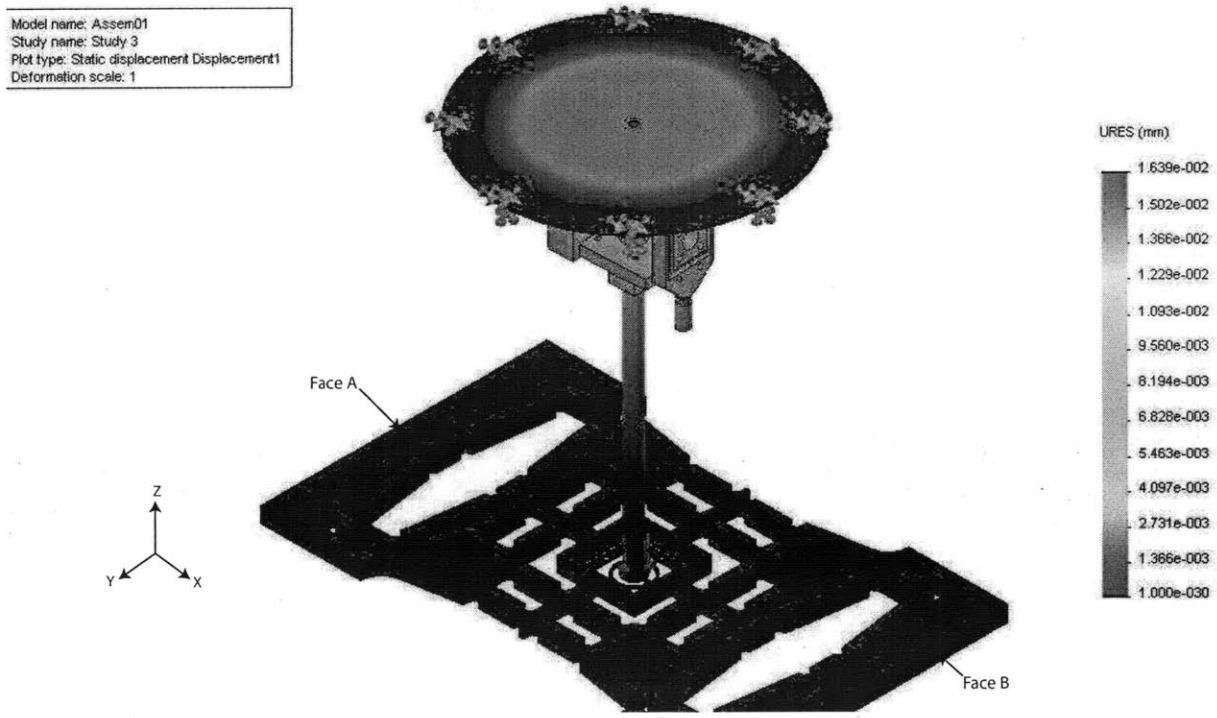

Figure 6-17: COSMOSWorks simulation of optics subassembly for Z with a force of 1N.

Figure 6-17 is a simulation of the Z stiffness of the integrated assembly. The top flexure is grounded at the eight holes around the circumference and the X-Y scanner is also grounded at the faces A and B. Taking the maximum displacement (i.e. 0.01639mm) and then the reciprocal of the maximum Z displacement, we found that the Z stiffness is approximately 61N/mm.

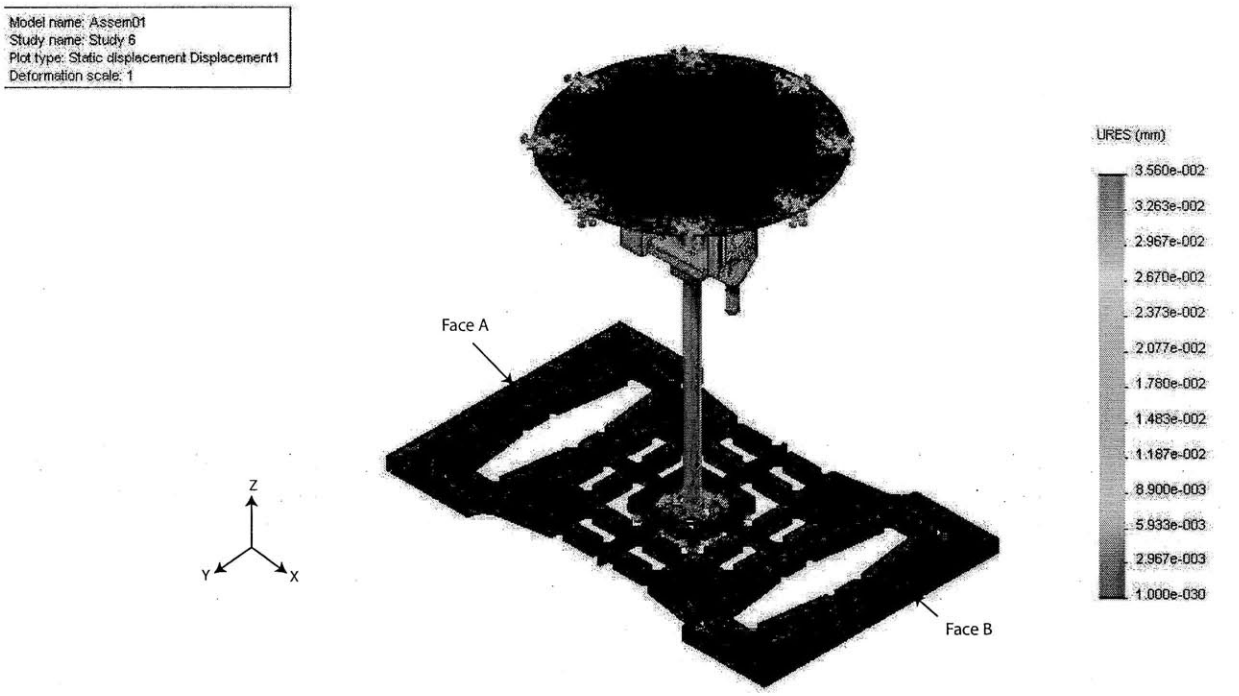

Figure 6-18: COSMOSWorks simulation of optics subassembly for θ_z with a torque of 1Nm.

Figure 6-18 is a simulation of the θ_z stiffness of the integrated assembly. The top flexure is grounded at the eight holes around the circumference and the X-Y scanner is also grounded at faces A and B.

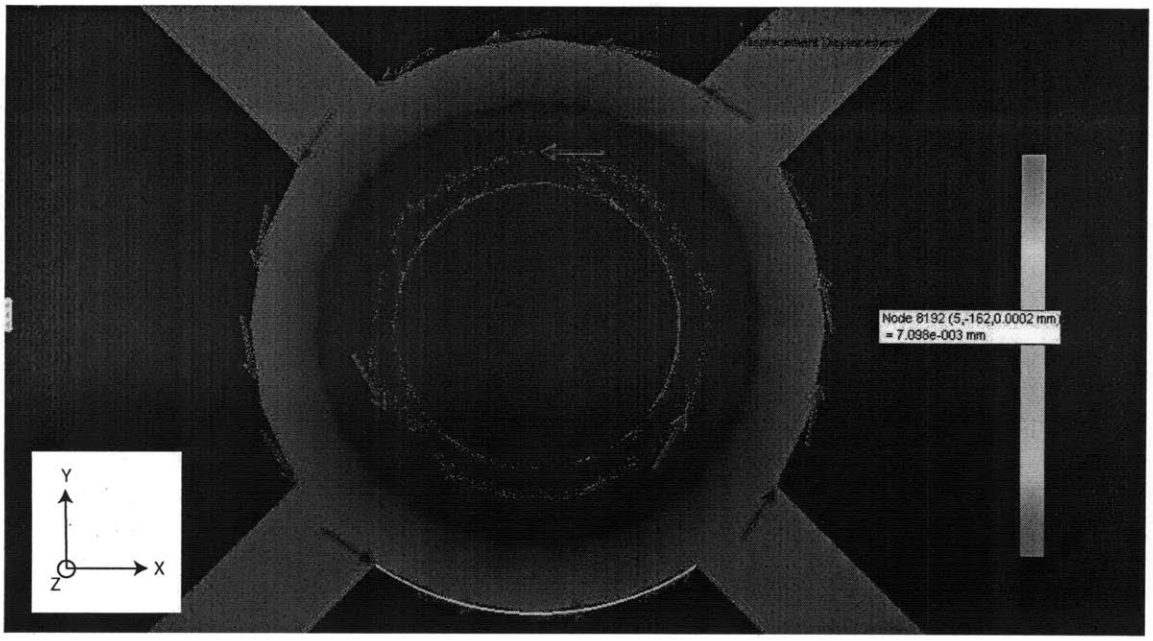

Figure 6-19: Bottom view of simulation of optics subassembly for θ_z with a torque of 1Nm.

Figure 6-19 is a view from the bottom of the integrated optical subassembly and X-Y scanner. Figure 6-19 displays the value of the deformation (i.e. 0.007098mm) at a coordinate of 5mm along the X axis. The angle formed from this deformation is the arctangent of 0.007098 divided by 5. The angle formed when the flexure deflect from 1Nm of torque is 0.00142 radians. Taking the reciprocal of the 0.0065 radians gives a stiffness of 704Nm/rad.

We integrated both flexures to the optics subassembly and used COSMOSWorks to simulate the stiffnesses in X, Y Z and θ_z direction. This is listed in table 6.3. The table shows that our optics subassembly has relatively low stiffnesses in the X and Y direction while maintaining a high stiffness in the Z direction. The angular stiffness, θ_z, is also relatively high.

The large Z stiffness to X and Y stiffness ratio will help decouple the Z resonance of the optics subassembly from the scanner. A high θ_z stiffness will also prevent the

tube from rotating about the Z axis at resonance.

Table 6.3: Stiffness of optics subassembly

Direction	Optics Subassembly Stiffness
X	$2\frac{N}{mm}$
Y	$2\frac{N}{mm}$
Z	$61\frac{N}{mm}$
θ_z	$704\frac{Nm}{rad}$

After calculating the stiffnesses of the integrated optical subassembly and the X-Y scanner, we now simulate the resonance frequencies of the integrated system in the X, Y, Z and θ_z directions.

The different resonance modes of the optical subassembly is carried out on a simplified model due to the long computation time it takes to compute the first 30 modes of the subassembly.

Figures 6-20, 6-21, 6-22 and 6-23, in the following pages are the X,Y,Z direction resonance and θ_z resonance of the optical subassembly integrated with the X-Y scanner.

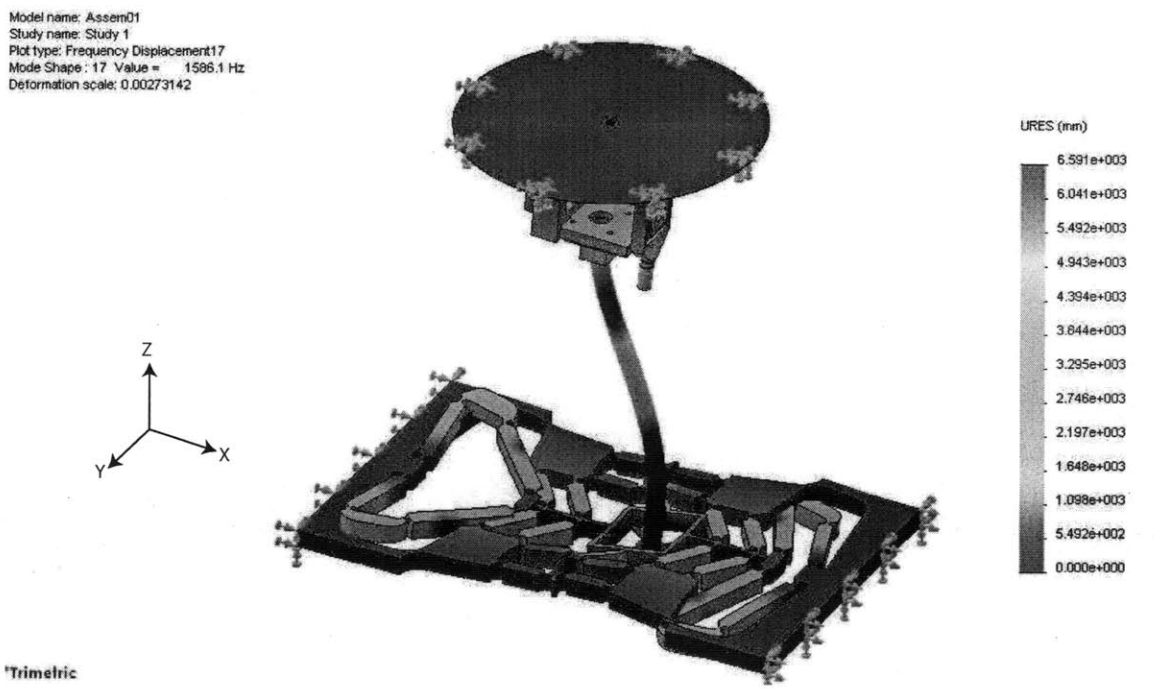

Figure 6-20: COSMOSWorks simulation of optics subassembly for resonance in the X direction.

Figure 6-20 is the simulation of the resonance of the integrated optical subassembly and the X-Y scanner. The resonance in the X direction is only 1581.1Hz as shown in the top left of the simulation plot.

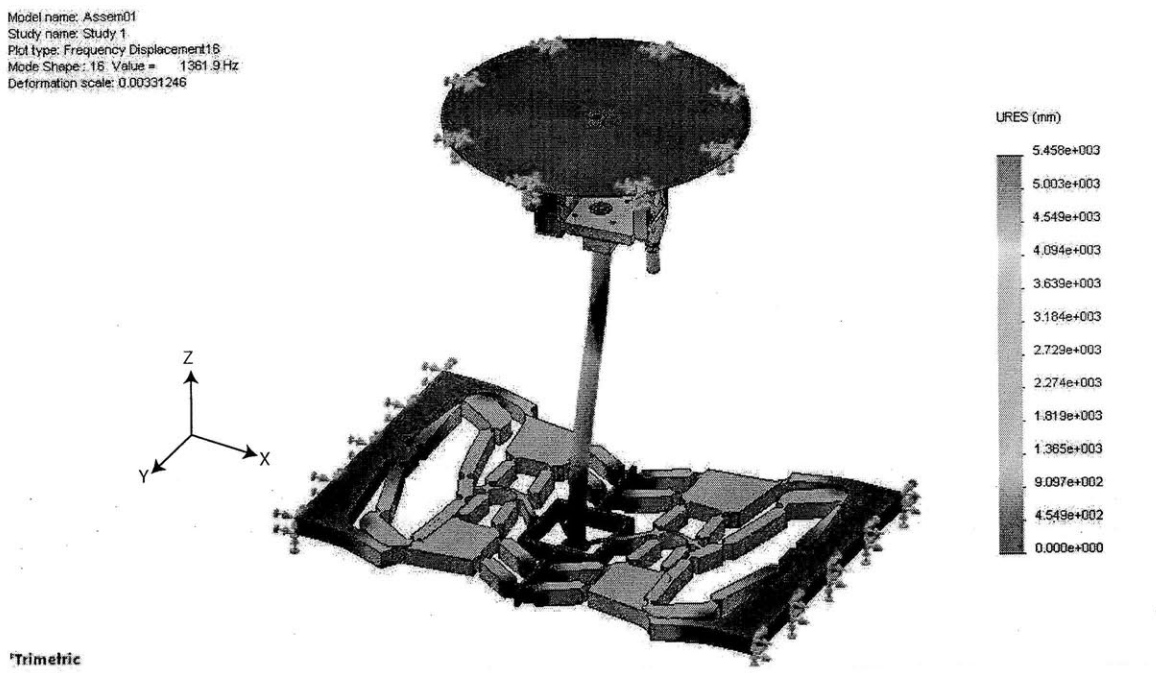

Figure 6-21: COSMOSWorks simulation of optics subassembly for resonance in the Y direction.

Figure 6-21 is the simulation of the resonance of the integrated optical subassembly and the X-Y scanner. The resonance in the Y direction is only 1361.9Hz as shown in the top left of the simulation plot.

Figure 6-22: COSMOSWorks simulation of optics subassembly for resonance in the Z direction.

Figure 6-22 is the simulation of the resonance of the integrated optical subassembly and the X-Y scanner. The resonance in the Z direction is only 233.72Hz as shown in the top left of the simulation plot.

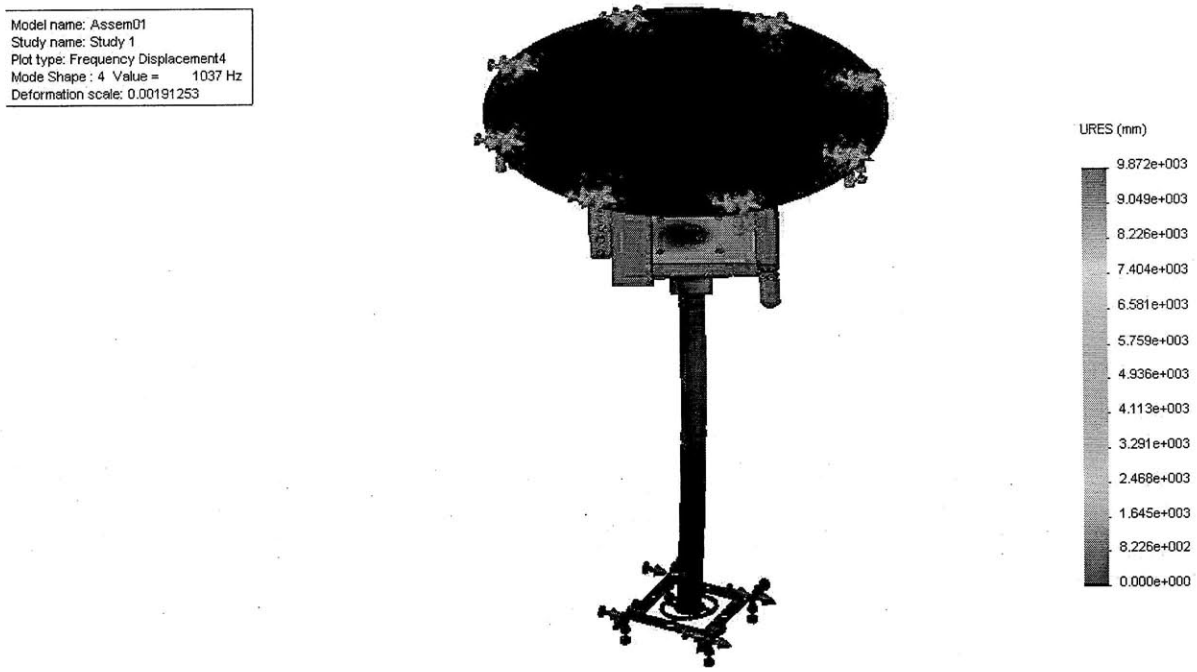

Figure 6-23: COSMOSWorks simulation of optics subassembly for resonance in the θ_z direction.

Figure 6-23 is the simulation of the resonance of the integrated optical subassembly and the X-Y scanner. The resonance in the θ_z direction is only 1037Hz as shown in the top left of the simulation plot.

Table 6.4: Resonances of optics subassembly

Direction	Optics Subassembly Resonance Frequency
X	1581.1Hz
Y	1361.9Hz
Z	233.72Hz
θ_z	1037Hz

As can be seen from figures 6-20, 6-21, 6-22 and 6-23, the X,Y,Z direction resonance and θ_z resonance of the optical subassembly integrated with the X-Y scanner are 1581.1Hz, 1361.9Hz, 233.72Hz and 1037Hz respectively. The values are not much

higher than the speed of the X-Y scanner (i.e. 1kHz). However, we adopted this flexure to quickly test our prototype. This is tabulated in table 6.4 and the next 2 figures shows the simulations of the Z and θ_z resonances.

6.6 Summary

This chapter describes the simulation and evaluation of the top flexure, bottom flexures and the optical subassembly. The main objective of the flexure design is to reduce the effect of the optical subassembly on the X-Y scanner dynamics.

Chapter 7

Lever Method - Prototype Fabrication and Assembly

7.1 Introduction

This chapter describes in detail the design and fabrication of 3 different prototypes of the optical subsystems and their components. The purpose of building these prototypes is to verify our proposed optical design and simulation discussed in chapter 5. Therefore, the design of the mechanical components are made to be easy to manufacture and assemble. The 3 different prototypes built and materials used are also described in detail.

7.2 Mechanical prototypes of Optical Subsystem Components

Prototype 1 of the mechanical structure is built using standard optics components, stages and mounts. Figure 7-1 is a photo of the actual setup to test the concept of our proposed objective lens optics. The 3mm solid state laser diode is mounted onto a

kinematic mount so that fine adjustment of the tilt (roll and pitch) of the laser diode is possible. This is necessary to accurately align the 3mm solid state laser diode with the 90° mirror. The 90° mirror is mounted on a rotation (yaw) stage which is in turn fixed to a kinematic mount. This allows the 90° mirror to rotate and ensure that the laser that reflects to the objective lens and laser beam that returns from the objective lens is horizontal. Figure 7-2 illustrates the need to have fine adjustment of the 90° mirror rotation.

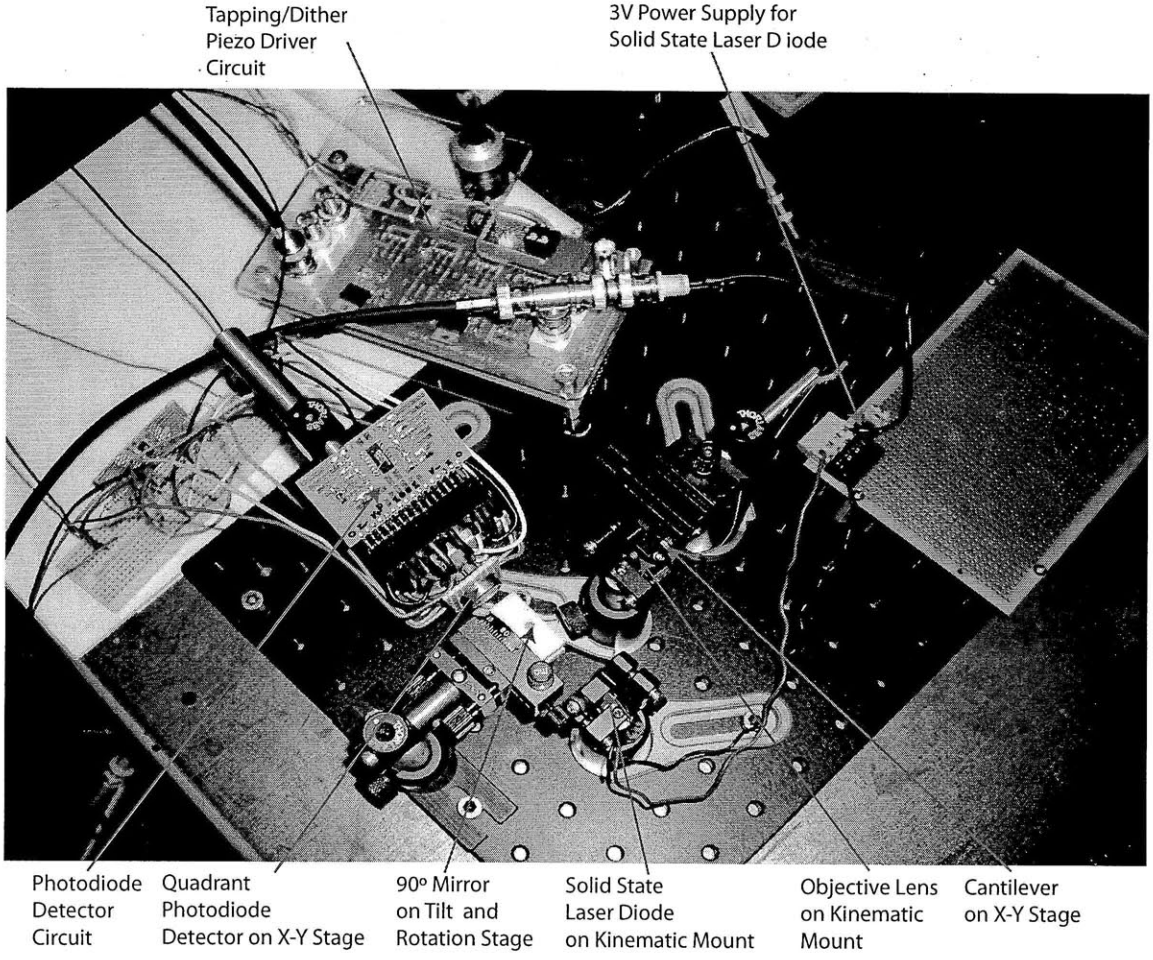

Figure 7-1: Experimental setup of prototype 1.

The objective lens is mounted on another kinematic to allow the objective lens to adjust its focal point to the back of the cantilever. The cantilever is also mounted on an X-Y translation stage to further assist the aligning the focal point of the lens to

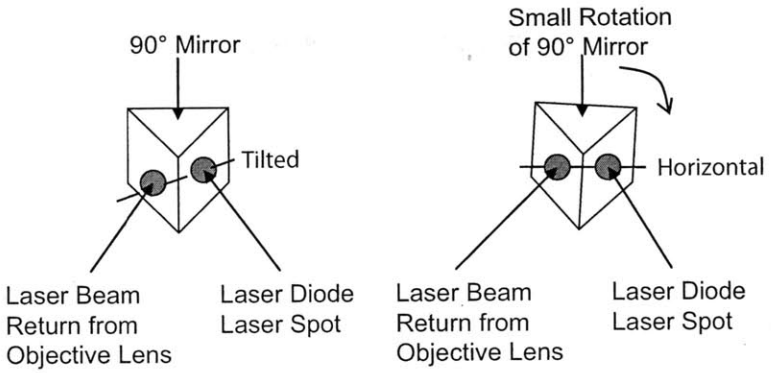

Figure 7-2: Slight adjustment of 90° mirror to align laser beam that returns from objective lens.

the tip of the cantilever.

Finally, the quadrant photodiode detector is mounted on another X-Y translation stage to move the quadrant photodiode to the center of the reflected laser beam so that the amplitude of the cantilever deflection will be centered at zero. The quadrant diode is moved to the center of the reflected laser beam by moving the quadrant diode up or down. It is desired to have the reflected laser beam at the center of the quadrant photodiode. This is illustrated in figure 7-3.

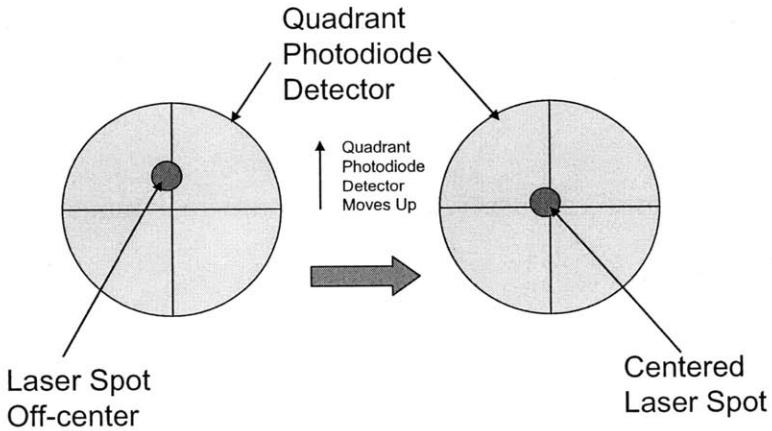

Figure 7-3: Illustration of centering laser spot on quadrant photodiode detector.

Now that the optical components are aligned, we will show that the laser spot falls on the cantilever. In order to show this, we obtain a tuning curve of the cantilever.

We excite the tapping piezo and measure the output signal from the photodiode and plot the frequency response of the photodiode signal. This is shown in figure 7-4.

Figure 7-4 shows the result taken from a digital signal analyzer. The X axis is the frequency and the Y axis is the amplitude in volts.

The amplitude of the cantilever vibration is captured and plotted in figure 7-4. As can be seen from the results, the cantilever resonates at a frequency of 82.91kHz. The results are relatively free from noise and show a distinct peak.

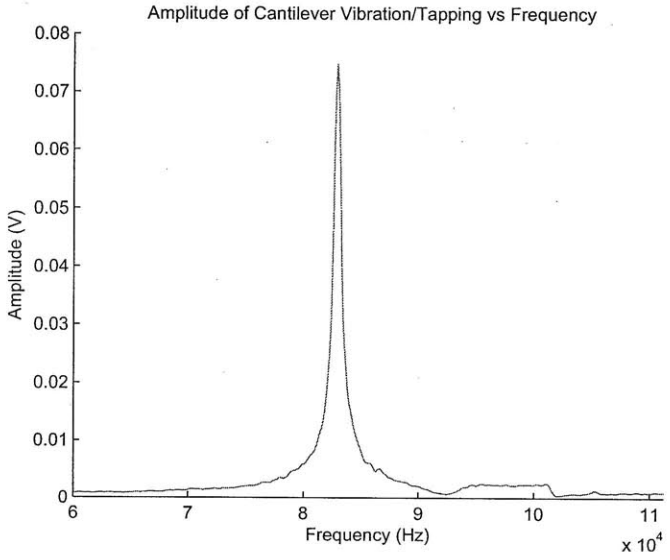

Figure 7-4: Amplitude of cantilever vibration at different input signal frequency of prototype 1.

Prototype 2 was an improvement from prototype 1 and is made to verify our proposed objective lens concept while the cantilever moves in steps of 5 microns in the X and Y directions.

Prototype 2 is different from prototype 1 in that the top and bottom flexures that allows the optical components to tilt is integrated into the optical subassembly. In prototype 2, the optical components are also embedded into an aluminum block (i.e.

2cm by 2cm by 2cm) while in prototype 1, the optical components are mounted on optical stages and kinematic mounts. Prototype 2 also uses a small cantilever instead of a conventional cantilever as in prototype 1. The resonance of a small cantilever is approximately 350KHz.

With the prototype 2, we want to verify 2 objectives. The first objective is to have the laser spot is small enough and fall onto the cantilever when the cantilever moves in the X and Y direction by 50 micron. The second objective is to have an initial adjustment mechanism that is necessary move the focal point of the laser spot to the desired tip of the cantilever. Both objectives are proven to work as proposed.

After describing the difference between prototype 1 and prototype 2, we will describe the model of prototype 2. A model of prototype 2 is shown in figure 7-5. Starting from the top of the figure, we have the top flexure. This top flexure carries the aluminum block that holds the laser diode, photodiode detector and the 90° mirror. The tube is then connected to the aluminum block. The other end of the tube is connected to a bottom flexure and the objective lens.

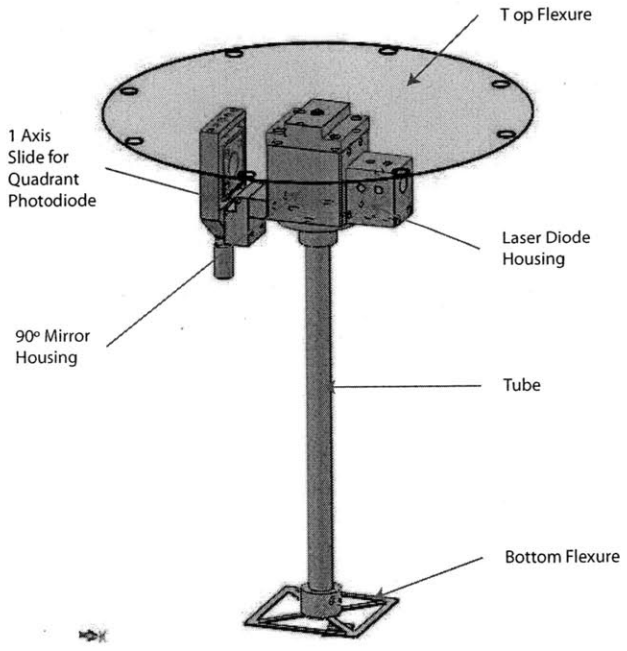

Figure 7-5: Prototype 2 model.

After describing the model of prototype 2, we will describe the experimental setup. The experimental setup of prototype 2 is shown in 7-6. The optical subassembly is mounted horizontally. Starting from the right of the figure, an X-Y micrometer stage is mounted on 2 aluminum frames. The X-Y micrometer stage is used a base for the top flexure. The aluminum block (i.e. 2cm by 2cm by 2cm) is attached to the top flexure. A 100mm tube is used to connect the aluminum block to the X-Y-Z and tilt stage. At the end of the 100mm tube, we attach the objective lens. The X-Y-Z and tilt stage holds the cantilever.

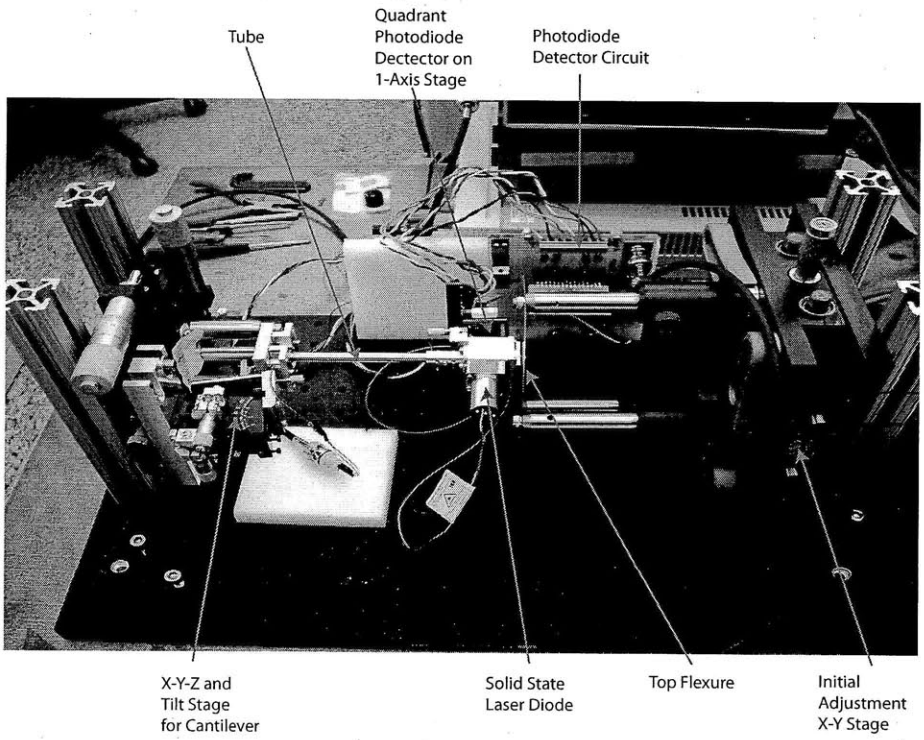

Figure 7-6: Prototype 2.

Figure 7-7 is the flexure that is fabricated for prototype 2. This flexure is cut out of blue-finished spring steel that is 0.4572mm(0.018") thick.The material properties in described in section 7.3. This flexure is fabricated with a waterjet machine. The detailed drawings can be found in Appendix A.

Figure 7-8 is the flexure that is used in prototype 2 and prototype 3. The material

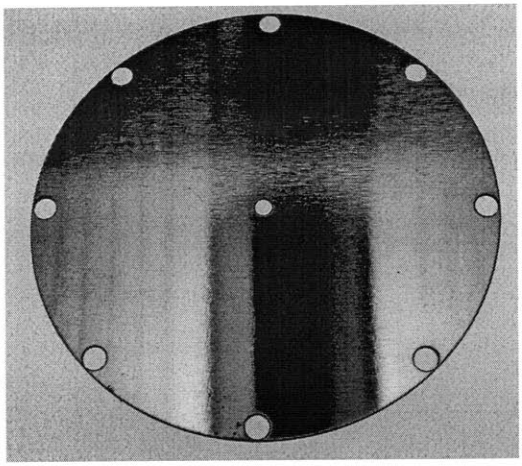

Figure 7-7: Photo of the top flexure.

properties of the bottom flexure is the same as the top flexure. This flexure is also made using a waterjet machine and is also spring steel.

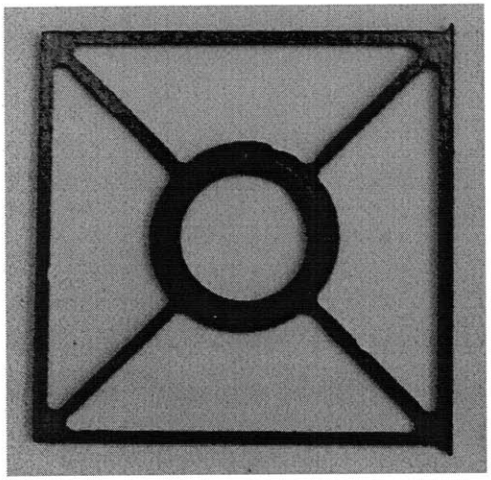

Figure 7-8: Photo of the bottom flexure.

In what follows, we present results showing that the laser spot falls onto the cantilever for the prototype 2 system.

The results of the amplitude plot of the prototype 2 is shown in figure 7-9. The X axis is the frequency and the Y axis is the amplitude of the signal from the photodiode detector. The result shows that the resonant frequency is approximately 355kHz.

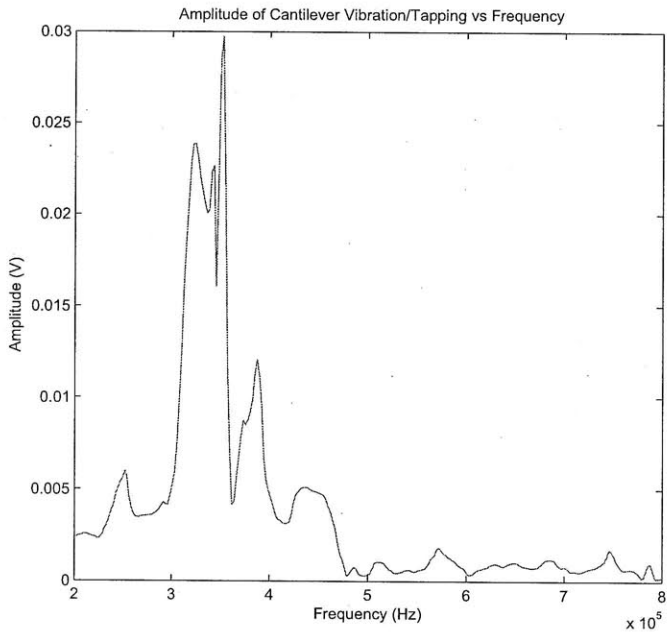

Figure 7-9: Amplitude of cantilever vibration at different input signal frequency of prototype 2.

The plot, however, is more noisy than the plot from the prototype 1 because there is optical clipping in the assembly. The clipping is caused by misalignment when the optical components are assembled in the aluminum block. There is no way to do fine adjustment of the optical components after they are embedded into the aluminum block. Numerous attempt were made to obtain accurate alignment by taking out all the optical components and re-assembling the optical components into the aluminum block but was not a good long term solution. Therefore, there is a need for the prototype 3 that does not have optical clipping.

We made some enhancements in prototype 3. In prototype 3, more adjustment mechanisms such as the miniature 1 axis slides were integrated in the optical subassembly so that we can align the 90° mirror, laser diode and photodiode detector. The adjustment mechanisms allow us to overcome optical clipping that exist in prototype 2. In prototype 2, there was no adjustment mechanisms for the optical components. Prototype 3 optical subassembly is also lighter and weighs only 62.44 grams. Prototype 2 weighs about 100 grams.

Prototype 3 is shown in figure 7-10. The detailed explanation of the mechanical assembly is in section 4.2.

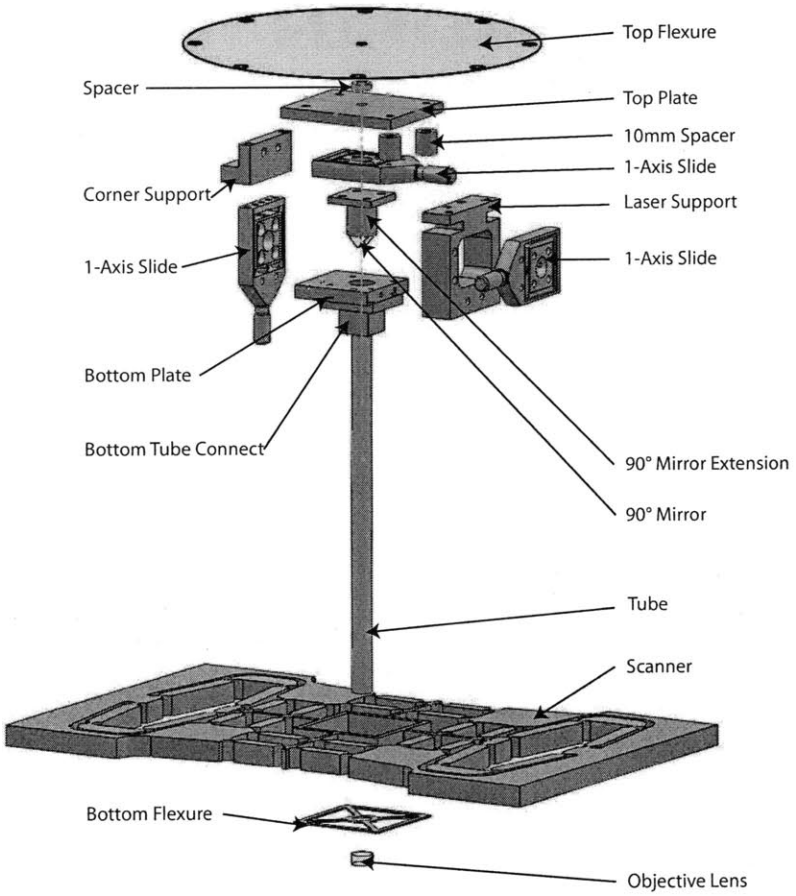

Figure 7-10: Exploded view of all mechanical parts in the optics subassembly of prototype 3.

In prototype 3, the objective lens, bottom flexure and the tube are epoxied together to prevent micro-slips that may occur when the scanner is in operation. This assembly of the tube, bottom flexure and the objective lens is shown in figure 7-11.

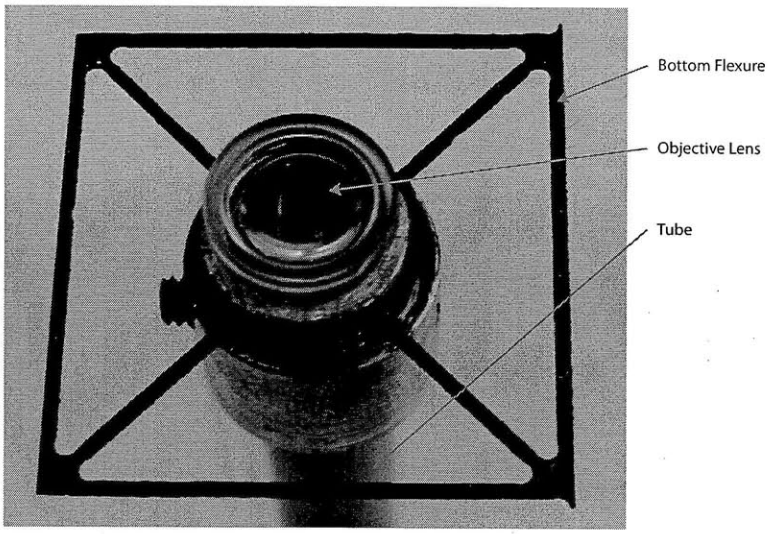

Figure 7-11: Bottom flexure and objective lens glued to the extension tube.

The assembled prototype that includes the optics subassembly and the X-Y scanner is shown in 7-12.

7.3 Material Selection for Optical Subsystem Components

There are 3 different types of materials we use for the flexures, extension tube and aluminum housing.

Both the top and bottom flexures are made of blue-finished and polished 1095 spring steel that is 0.4572mm(0.018") thick. Spring steel is necessary for the flexures as spring is able to restore it to its original shape after distortion.

The tensile strength of 1095 spring steel is 1015 MPa, yield strength is 505 MPa and modulus of elasticity is 205 GPa. The Poisson ratio is 0.29 and the density is

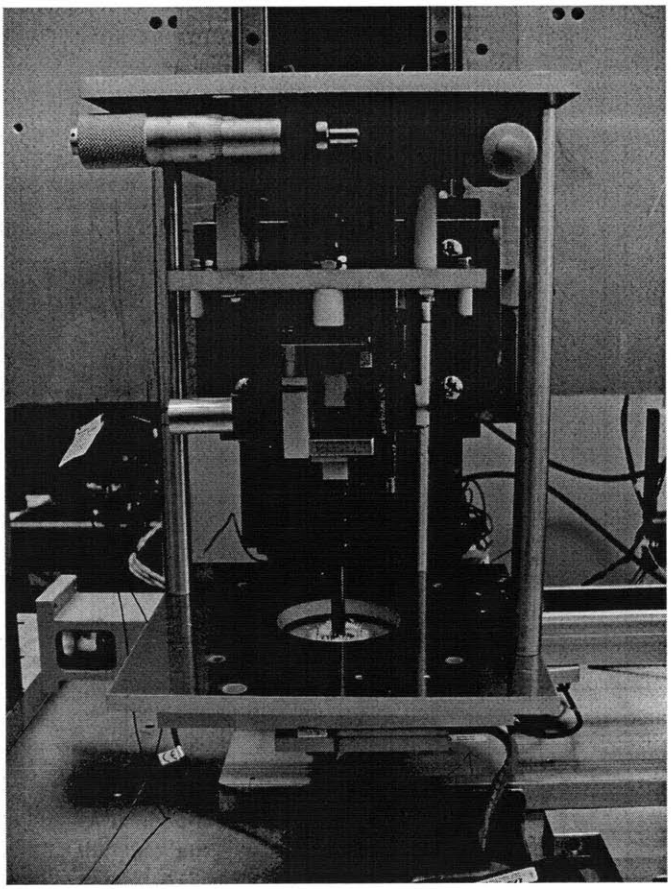

Figure 7-12: Photo of assembled prototype 3.

7850 kg/cubic meter[12].

The extension tube needs to be extremely stiff to prevent buckling and also need to be light. Therefore a stainless steel tube with 0.254mm(0.01") wall thickness.

The tensile strength of stainless steel is 870 MPa, yield strength is 613 MPa and modulus of elasticity is 196 GPa. The Poisson ratio is 0.284 and the density is 7810 kg/cubic meter[12].

Housings to locate and hold all the optics components such as the 90° mirror, etc. are made of 6061 aluminum for dimensional stability and light weight.

The tensile strength of 6061 aluminum is 124 MPa, yield strength is 55.2 MPa and modulus of elasticity is 68.9 GPa. The Poisson ratio is 0.33 and the density is 2700 kg/cubic meter[12].

Tables 7.1 and 7.2 lists the material properties of the 3 materials we use in prototype 3.

Table 7.1: Summary of Material Properties1

Material	Tensile Strength	Yield Strength	Modulus of Elasticity
1095 Spring Steel	1015 MPa	505 MPa	205 GPa
Stainless Steel	870 MPa	613 MPa	196 GPa
6061 Aluminum	124 MPa	55.2 MPa	68.9 GPa

Table 7.2: Summary of Material Properties 2

Material	Poission Ratio	Density
1095 Spring Steel	0.29	$7850m^2$
Stainless Steel	0.284	$7510m^2$
6061 Aluminum	0.33	$2700\text{kg}/m^2$

7.4 Summary

This chapter describes in detail the 3 different prototypes built and materials used. Prototype 3 design incorporated fine adjustment of the solid state laser diode, quadrant photodiode detector and the 90° mirror because the various optics components are extremely sensitive to misalignment and any slight misalignment will introduce optical clipping. This requirement is accomplished with small single axis slides weighing below 100g for all 3 optics components.

Chapter 8

Fiber Collimator Method - Design

8.1 Introduction

This chapter describes the design of the fiber collimator method. An overview of the concept is provided. The design of the optical subassembly is discussed and the design for integrating the optical subassembly to the X-Y scanner is also discussed.

8.2 Overview of the Fiber Optics Method

This section describes the fiber collimator design that uses a tiny fiber optic collimator instead of the Coherent VLM2 laser module used in the lever method. This eliminates the need for a lever mechanism. Therefore, the tube and heavy optical subassembly is not necessary.

However, the small optics lacks the facility to adjust the laser spot onto the back of the cantilever. To overcome this, we used a total of 4 single axis stages to move the cantilever holder so that the back of the cantilever is at the focal point of the objective lens. Another 1 single axis stage is used to move the quadrant diode detector to the center of the reflected laser beam.

Therefore, the main 2 differences between the lever method and the fiber collimator

method are the use of a fiber collimator instead of a laser diode module and the initial adjustment of the cantilever instead of the initial adjustment of the optical subassembly when a new cantilever is mounted.

Figure 8-1 shows the key components of the fiber optics method to track the cantilever. The optical path is the same as the objective lens method presented in chapter 3.

In figure 8-1, the laser beam comes from an external source and is guided to the optical subassembly using a fiber collimator. The laser beam from the fiber collimator is directed to the objective lens. The objective lens focuses the laser beam onto the back of the cantilever and the back of the cantilever reflects the laser beam back into the other end of the objective lens (as described in chapter 3). The reflected laser beam that passes through the objective lens then travels back up to the quadrant photodiode that is mounted at the top of the central stage of the X-Y scanner.

From figure 8-1, we see that the cantilever is attached to a tapping piezo and secured to the bottom of the central stage of the scanner using a magnet.

To adjust the cantilever so that the back of the cantilever falls onto the focal point of the objective lens, a 1 axis linear stage for cantilever adjustment is mounted near the cantilever so that we can push the cantilever with the 1 axis linear stage. A total of 4 single axis linear stages are necessary to move the cantilever in the X and Y directions (i.e. 2 for X direction and 2 for Y direction).

To adjust the quadrant photodiode, we mount another linear stage near the quadrant photodiode to move the quadrant photodiode in the X direction only. This is to move the quadrant photodiode so that the quadrant photodiode is at the center of the reflected laser beam. A total of 1 linear stage is necessary for moving the quadrant photodiode.

After all the adjustment is made, the 5 adjustment mechanism (i.e. 4 for the cantilever adjustment and 1 for the quadrant photodiode adjustment) will be removed

so that the X-Y scanner can start scanning.

In the next section, we will show the optical fiber collimator that will be integrated into the optical subassembly.

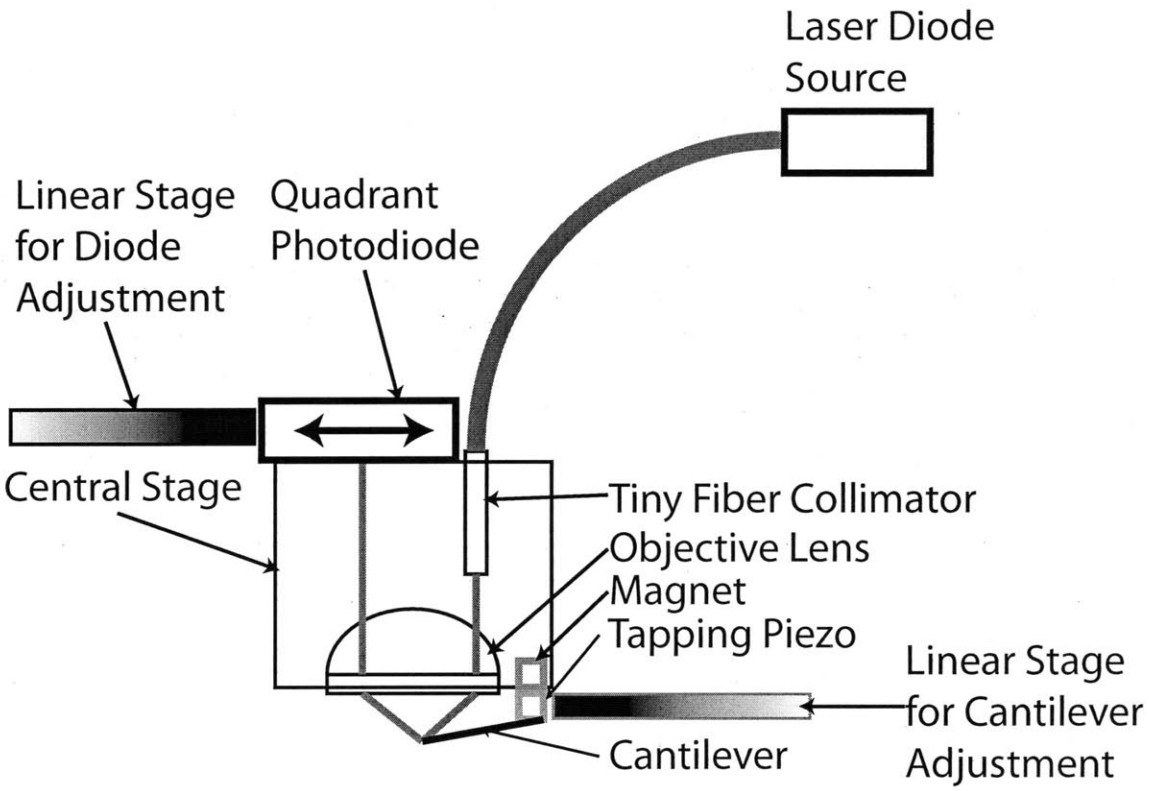

Figure 8-1: Schematic of the operation of the fiber optics method for tracking the cantilever.

8.3 Fiber Collimator

In this section, we will briefly describe the fiber collimator that we use for integration into the optical subassembly. Figure 8-2 is a photo of the tiny fiber collimator that is used in the fiber optics method. The collimator is at the tip of the fiber and the 5mW laser source is connected to the other end of the fiber. The supplier is Silicon Lightwave Inc. and the address is included in appendix B.

The next section discuss the design of the optical subassembly that includes the

fiber collimator, quadrant photodiode, optical subassembly block and the Z piezo stacks.

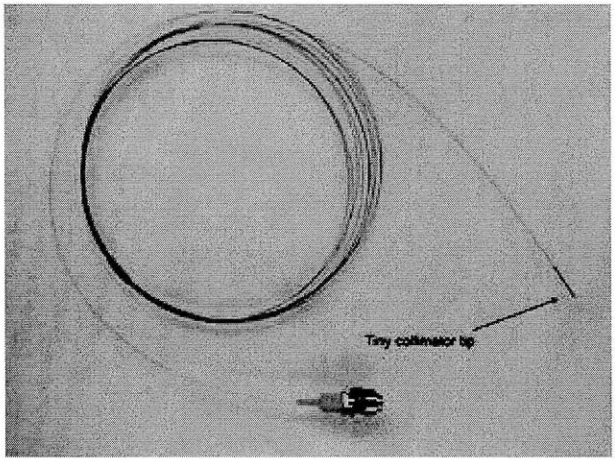

Figure 8-2: Photo of a tiny fiber collimator. [8]

8.4 Design of the Optical Subassembly for the Fiber Collimator Method

Figure 8-3 shows the design of the optical subassembly for holding the tiny fiber collimator and the quadrant photodiode. The optical subassembly block is made using ABS plastics. This optical subassembly block is displayed in transparent mode in figure 8-3.

There is also an opening to allow the stacking of 3 2x2mm Z piezo stack for the Z actuators. The cantilever epoxied to the cantilever cross as shown in figure 8-3 and can be adjusted in small steps to position the back of the cantilever at the focal point of the objective lens.

In the next section, we will discuss how this optical subassembly is integrated into the X-Y scanner.

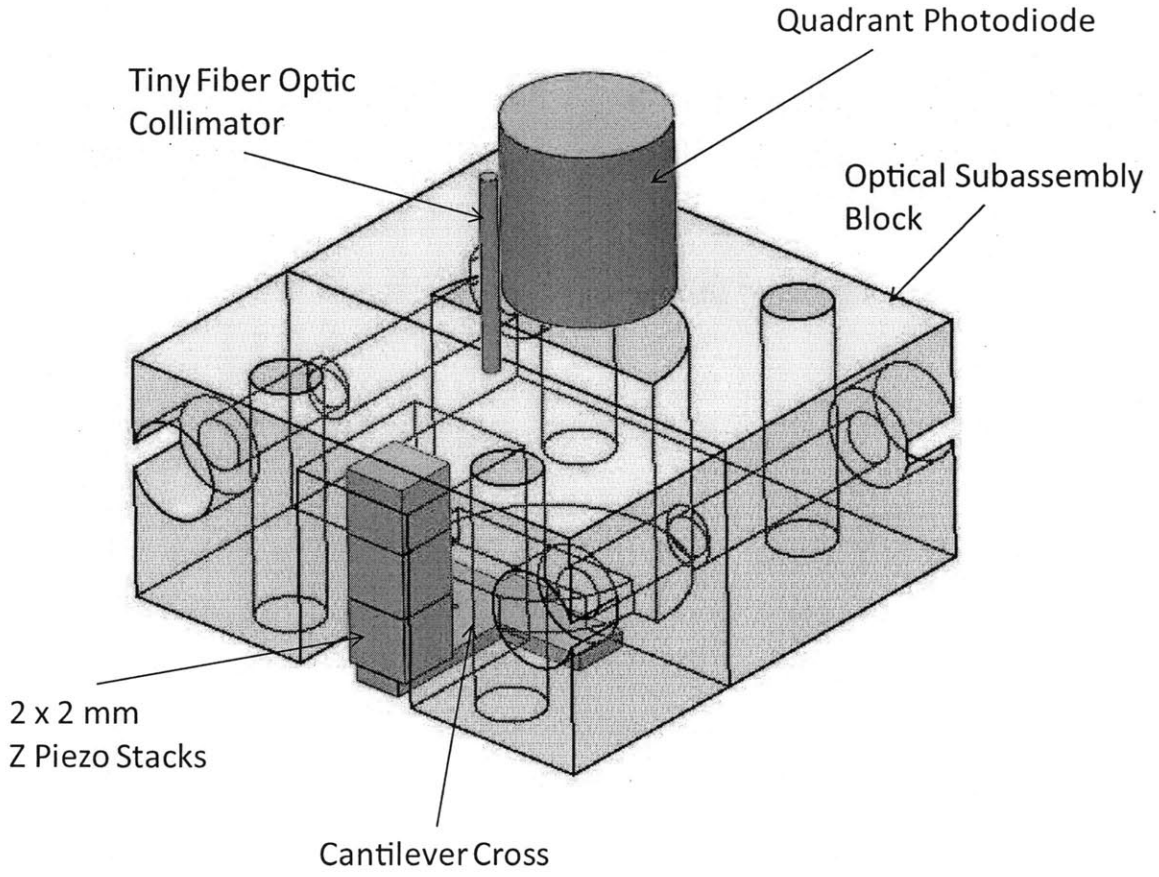

Figure 8-3: Design of central stage to hold tiny fiber collimator and bi-cell photodiode.

8.5 Integration of Optical Subassembly to the X-Y Scanner

We will now describe how the optical subassembly for the fiber collimator method is integrated into the X-Y scanner.

The design of the assembly that integrates the fiber collimator optical subassembly to the X-Y scanner is shown in figure 8-4. At the top of figure 8-4, there is a photodiode adjustment slide. This slide is to move the photodiode to the center of the reflected laser beam. This adjustment slide in mounted on a photodiode adjustment support plate.

Below the photodiode adjustment support plate, there are 4 adjustment linear stages. They are named as the cantilever adjustment slides in figure 8-4. These 4 single axis linear slides are in turn mounted on the cantilever adjustment support plate.

The cantilever adjustment support plate is then attached to the top of the scanner. At the bottom of the scanner are the objective lens, cantilever holder and the cantilever.

8.6 Summary

This chapter outlines the design of the fiber collimator design and the integration design with the X-Y scanner to track the cantilever.

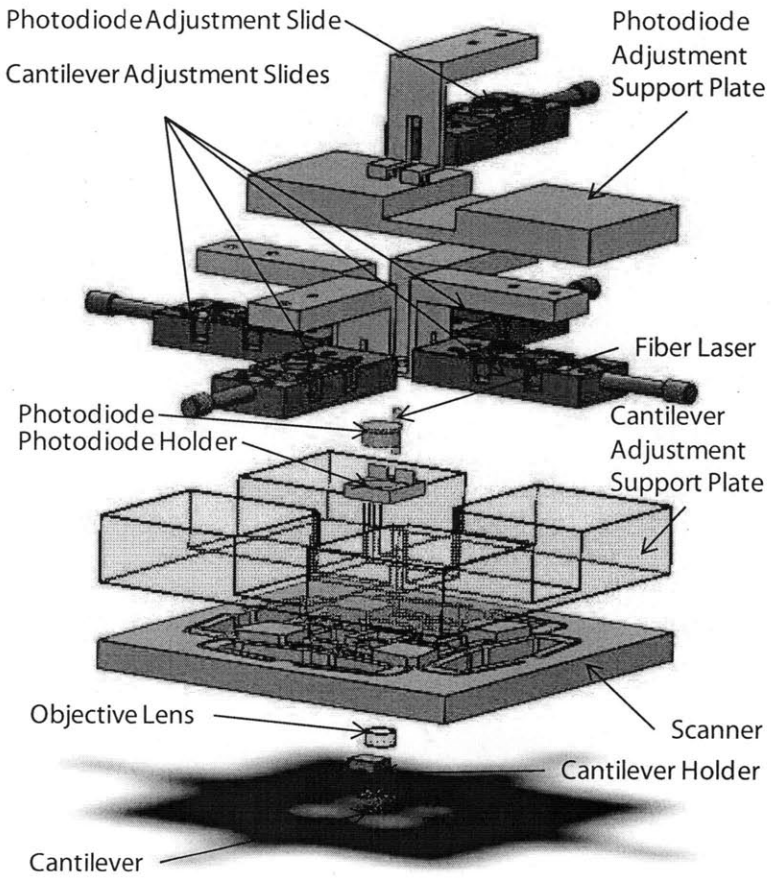

Figure 8-4: Design of the assembly of the central stage, the X-Y scanner and precision adjustment stage.

Chapter 9

Quadrant Photodiode Circuit for Lever and Fiber Optics Method

9.1 Introduction

This chapter describes the design details, simulation, fabrication and testing of the quadrant photodiode detector circuit. Section 9.3 provides a brief introduction of the sensor. Suitable quadrant photodiode sensor with a corresponding equivalent circuit model and high speed current to voltage converters with the correct specification are selected and described in sections 9.4 and 9.6 respectively. A simulation of the circuit is carried out and presented in section 9.7. The final section documents the fabrication, testing and deployment of the circuit.

9.2 Custom Quadrant Photodetector Circuit

There is a need to design and fabricate a new quadrant photodiode detector circuit because of a high 2MHz bandwidth requirement and limitations on size. A 2MHz bandwidth is required since we are using small cantilevers with resonance frequency of approximately 2 MHz. Typical resonance frequency of small cantilevers are in

the range of hundreds of KHz. Commercial quadrant photodiode position sensors[1] cost thousands of dollars and have a maximum bandwidth of only 150kHz. Our quadrant photo detector circuit cost only approximately $200 including the quadrant photodiode sensor[9].

9.3 Quadrant Photodiode Basics

A quadrant photodiode is a 2x2 array of different photodiode active areas. These 4 active areas are arrange in a rectangular fasion, 2 at the top and 2 at the bottom. These active areas are also separated by a small gap. As light enters a semiconductor material such as silicon, the semiconductor material produces a small current as shown in figure 9-1. This is known as the photo effect.

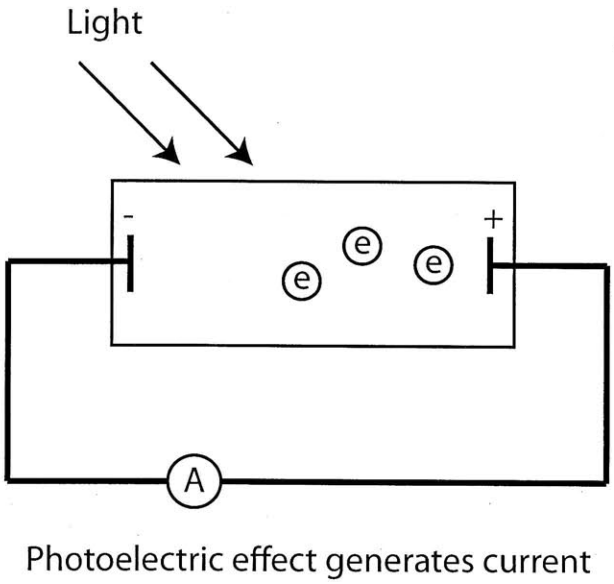

Figure 9-1: Photoelectric effect generates electric current.

A photodiode can also be configured to operate in reverse bias (photoconductive) or forward bias (photovoltaic) mode. When in reverse bias mode, the junction capacitance of the photodiode will be less, resulting in faster response. The tradeoff is

[1]such as Thorlabs and New Focus

a higher dark current when the active area is not exposed to any light. This dark current[2] will induce a offset in the output of the amplifier even when there is no light. The dark current offset in the amplifier can be overcome by choosing an appropriate amplifier that will be described in section 9.6. This current and voltage characteristics is shown in figure 9-2.

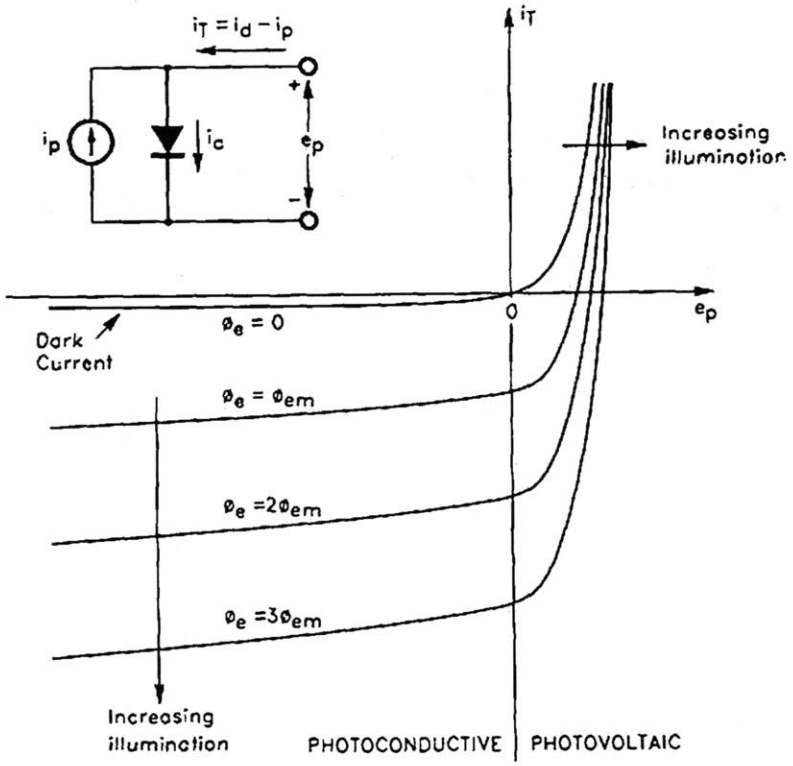

Figure 9-2: Operating regions of photoconductive and photovoltaic configurations of a photodiode.[9]

[2]Dark current is a small current that is produced by the photodiode even when there is no light falling on the sensor

9.4 Quadrant Photodiode Sensor

This section describes how we choose a suitable quadrant photodiode sensor for our application.

The requirements of the quadrant photodiode sensor are:

- 15mm diameter geometrical constraint
- 50g weight constraint
- 50 micron range
- 2MHz bandwidth
- nanometer resolution

A suitable photodiode that will satisfy the above specifications will have be in a package that has a diameter that is less than 15 mm. The standard TO-5 metal package has a diameter of 8mm and is smaller than 15 mm. Typical photodetector in the TO-5 metal package weight less than 10g. The active area of a TO-5 photodiode detector sensor is also larger than 50 microns. The photodetector sensor must also have a low junction capacitance (C_d) for a 2 MHz bandwidth. The final photodiode that is selected is a red enhanced quad cell silicon photodiode SD085-23-21-021 from Advanced Photonix Inc. Figure 9-3 shows the photodiode that is used in the optical system. The supplier is Advanced Photonix Inc. and the address is included in appendix B.

9.5 Quadrant Photodiode Sensor Equivalent Circuit

In order to model the response of the photodiode, the photodiode circuit model shown in figure 9-4 is used to simulate a real photodiode in SPICE.

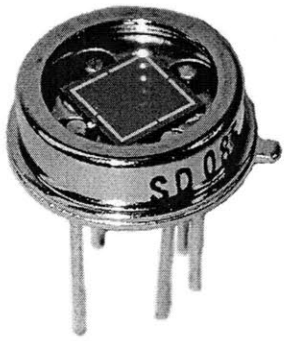

Figure 9-3: A photo of the quadrant photodiode used in the optics system. [10]

Since the photodiode detector sensor is a current source when light falls on the photodiode detector, we model current that the photodiode detector sensor produces as a current source (i_p). The photodiode detector is represented by the diode in figure 9-4. The junction capacitance is the capacitance of the active area of the photodiode detector sensor. The junction capacitance of the active area is lower when in reverse bias than when in forward bias. A junction capacitance of 9pF is assigned to the model because the diode is operating in the reverse biased configuration. The shunt resistance (R_s) represents the resistance of the photodiode detector sensor that is connect in parallel and is specified as 350MOhm in the datasheet. The series resistance (R_d) is assumed to be negligible.

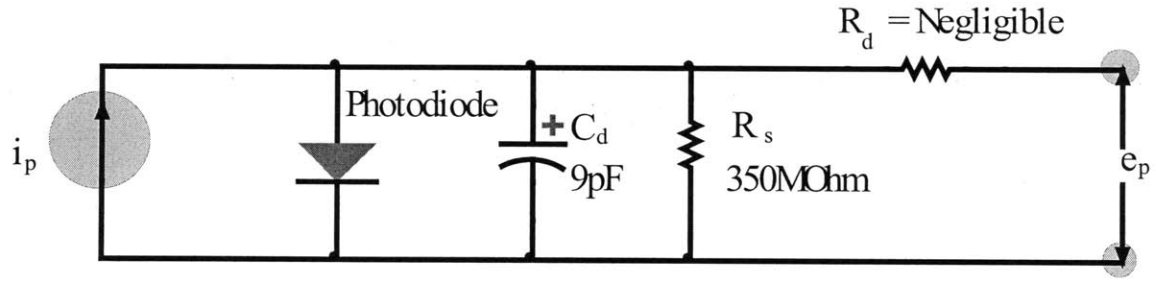

Figure 9-4: A model of an individual active area of a 2x2 aray quadrant photodiode.

9.6 High Speed Photodetector Circuit Design

The output of the photodiode needs to be converted from current to voltage. A transimpedance amplifier or current to voltage converter is used for this purpose. The input of the transimpedance (current to voltage) amplifier accepts signals from either the top 2 active areas or bottom 2 active areas (both active areas connected in parallel) of the quadrant photodiode. This is shown in figure 9-5.

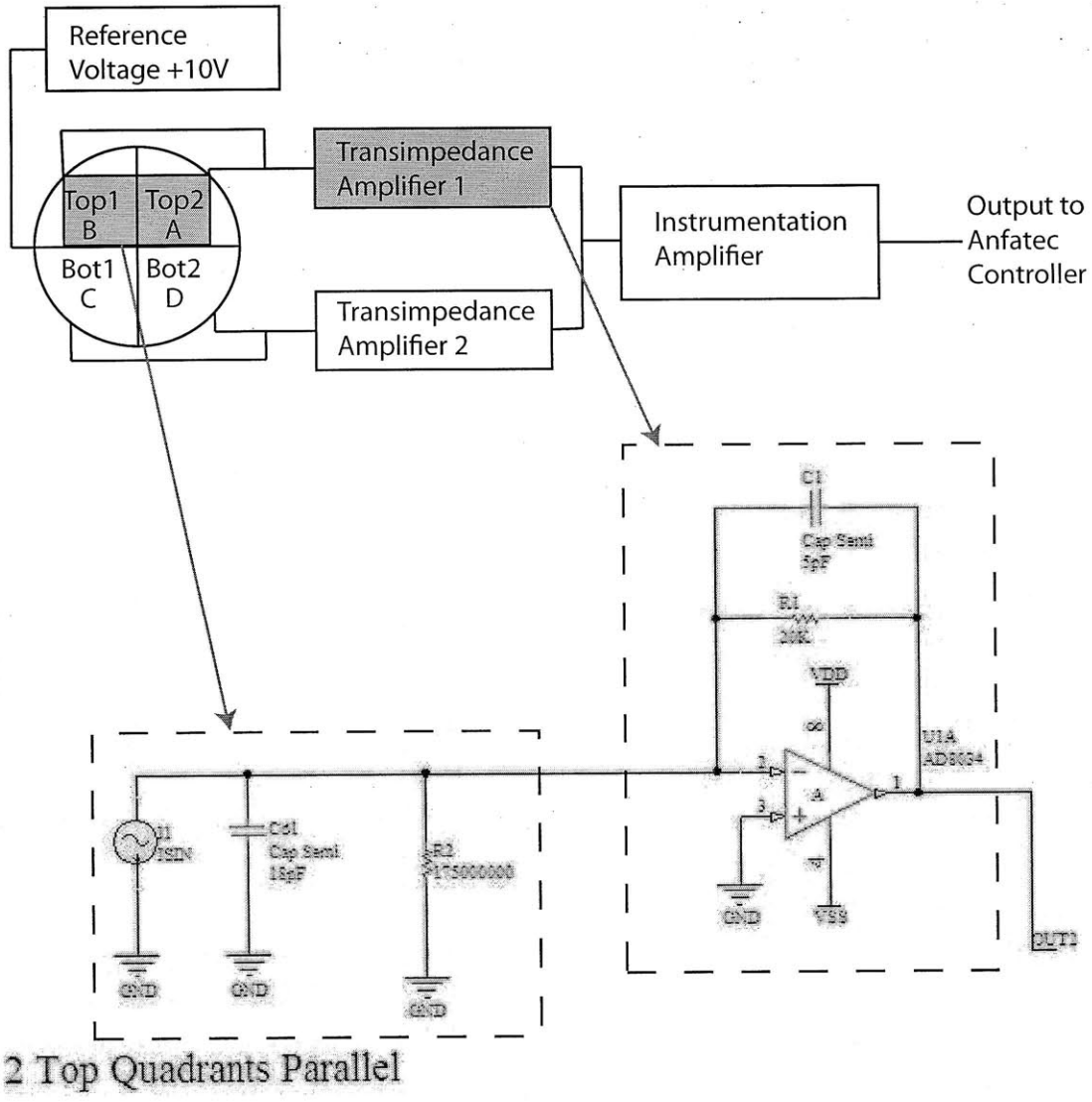

Figure 9-5: Schematic of a single current to voltage converter (also known as transimpedance amplifier).

The requirements of the transimpedance amplifiers are:

- 2MHz bandwidth
- $\pm 10V$ output
- Zero DC offset
- SOIC package
- Dual or quad package configuration

To achieve a bandwidth of 2 MHz, an amplifier of at least 10MHz is required. A $\pm 12V$ supply for the amplifier will be able to satisfy an output of 10V. The dark current that is generated by the quadrant photodiode has to be suppressed with an amplifier that has extremely low input bias current, preferably in the pA range. An 80 MHz FASTFET^{TM}operational amplifier AD8034 from Analog Devices Inc. meets both the high bandwidth and $\pm 10V$ output. This amplifier also has a low input bias current of 1pA. The amplifiers also come in dual 8-pin SOIC package.

The second stage of the amplifier circuit for the quadrant photodiode circuit is an instrumentation amplifier that subtracts the bottom 2 active areas of the 2x2 array from the top 2 active areas. The output from the first stage transimpedance amplifiers that is connected to the top 2 active areas is wired to the positive input of the instrumentation amplifier. Similarly, the output of the first stage amplifier that is connected to the bottom 2 active areas is wired to the negative input of the instrumentation amplifier.

The instrumentation amplifier chosen is AD8253 from Analog Devices Inc. It is a programmable gain instrumentation amplifier with a bandwidth of 10MHz at a gain of 1 and accepts a supply voltage of $\pm 12V$. This makes it the most suitable

instrumentation amplifier for a 2MHz photodetector circuit. The full schematic of the photodetector circuit is shown in figure 9-6.

In addition, we want to operate the photodiode detector in reverse bias mode. Therefore, we need to provide a precision reference voltage of 10V to the common of the 4 active areas of the quadrant photodetector sensor.

In order to operate the photodiode detector in reverse bias, we use a precision reference voltage REF102AU from Texas Instrument Inc. that provides a reverse voltage of 10V to the common cathode of the quadrant photodiode. This 10V reverse bias voltage will force the photodiode to operate in the reverse bias configuration and will result in faster response. The dark current that is present when the photodiode is in the reverse bias mode is circumvented by using a transimpedance amplifier (AD8034) with only 1pA input bias current. The precision reference voltage is included in the schematic in figure 9-6.

To reduce the power-supply noise coupling to the circuit, a pair of $\pm 12V$ regulators are also included in the circuit. Decoupling capacitors are also placed at the supply pins of all amplifiers to reduce noise. Since all power supply sources come from on-board components, noise coupling from external power supply is reduced to a minimum.

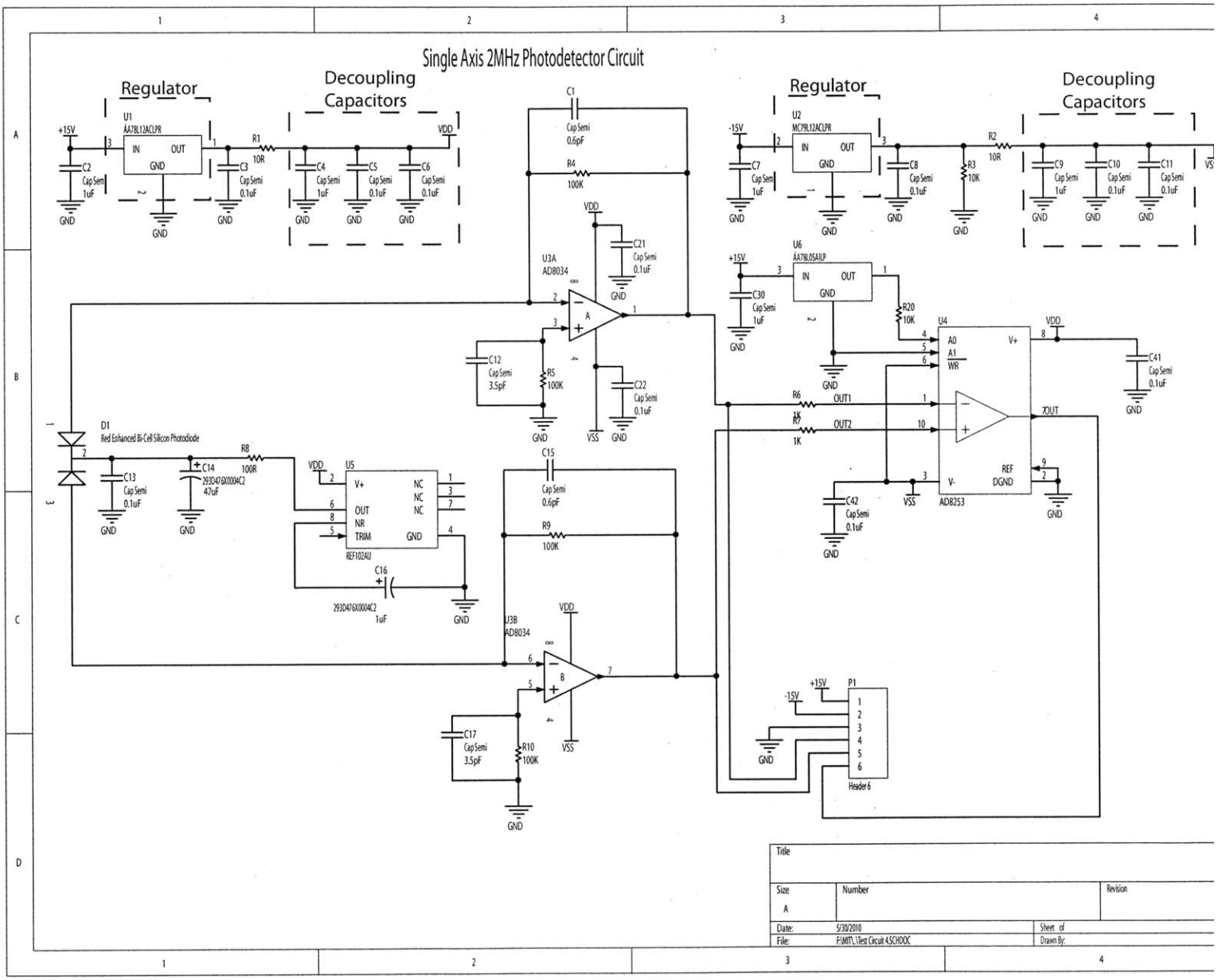

Figure 0.6: Schematic of the entire circuit including transimpedance amplifiers in-

9.7 Circuit Simulation

The proposed circuit design is simulated in SPICE to verify the stability and bandwidth of the electrical design. From the simulation, we can obtain the frequency response of the circuit. The target bandwidth of our circuit should be approximately 2MHz

The quadrant photodiodes are simulated as sine wave current source with a shunt resistance of 1750Mohm and a junction capacitance of 18pF. The datasheet specified the shunt resistance and junction capacitance of each active area to be 350MOhm and 9 pF respectively. The shunt resistance and junction capacitance is set to 175Mohm and 18pF respectively because 2 active areas (top 2 or bottom 2) of the quadrant photodiode is connected in parallel. Figure 9-7 is the circuit that is used to simulate the performance of the proposed design in SPICE.

To obtain the frequency response of the circuit, we run a simulation with frequency of the sine wave current source ranging from 100Hz to 20MHz. This is known as AC analysis in SPICE. Figures 9-8 and 9-9 are the simulated result presented as a bode plot in magnitude and phase respectively. From the figure, it can be seen that the circuit have a bandwidth of about 2 MHz (where the magnitude is at -3dB).

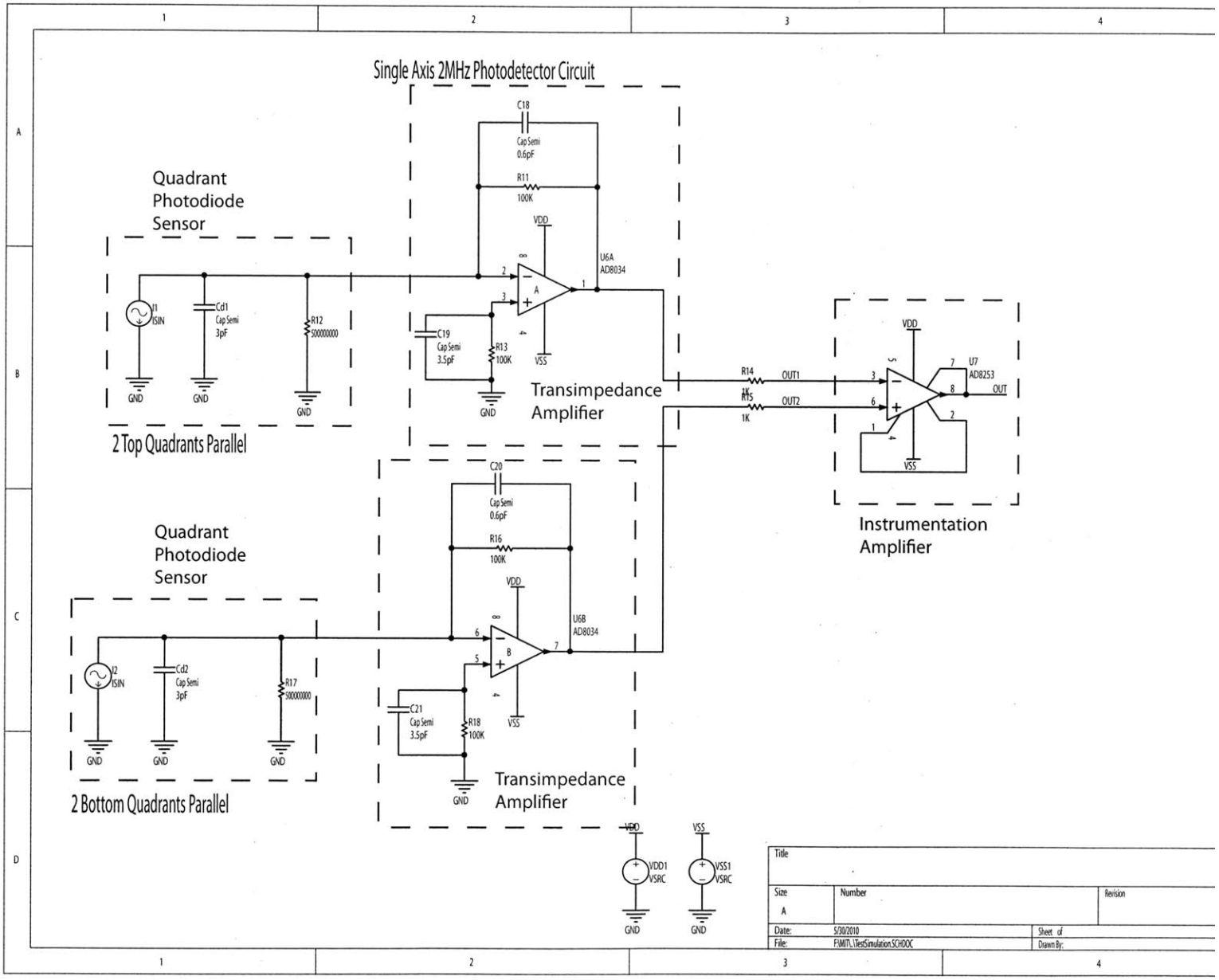

Figure 9-7: Schematic of the circuit that is simulated. photdiode is represented by a

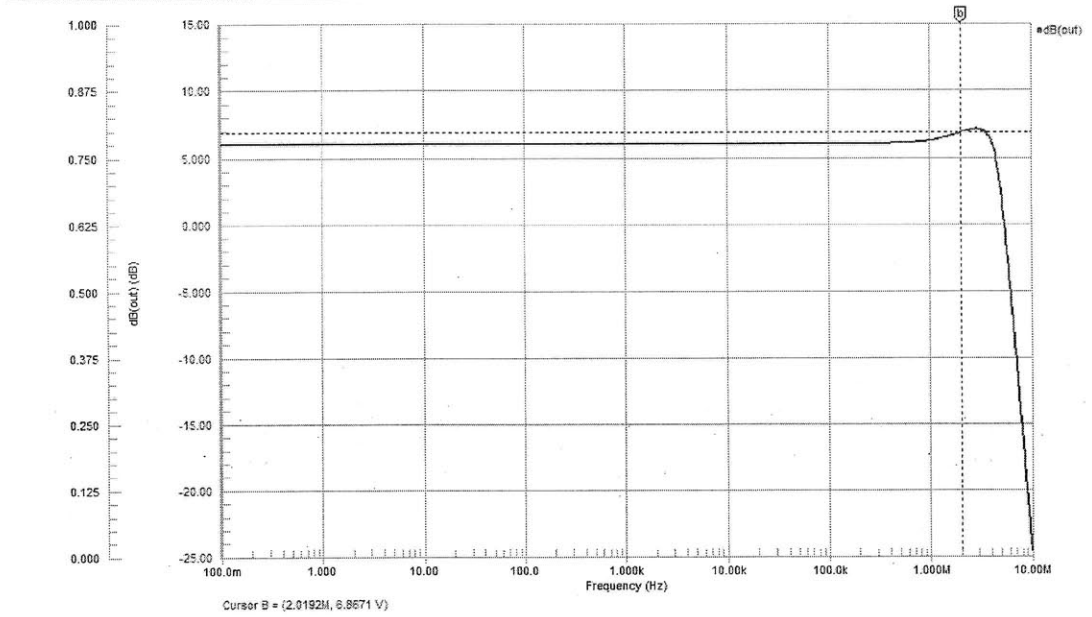

Figure 9-8: Magnitude bode plot of the output of the simulated circuit.

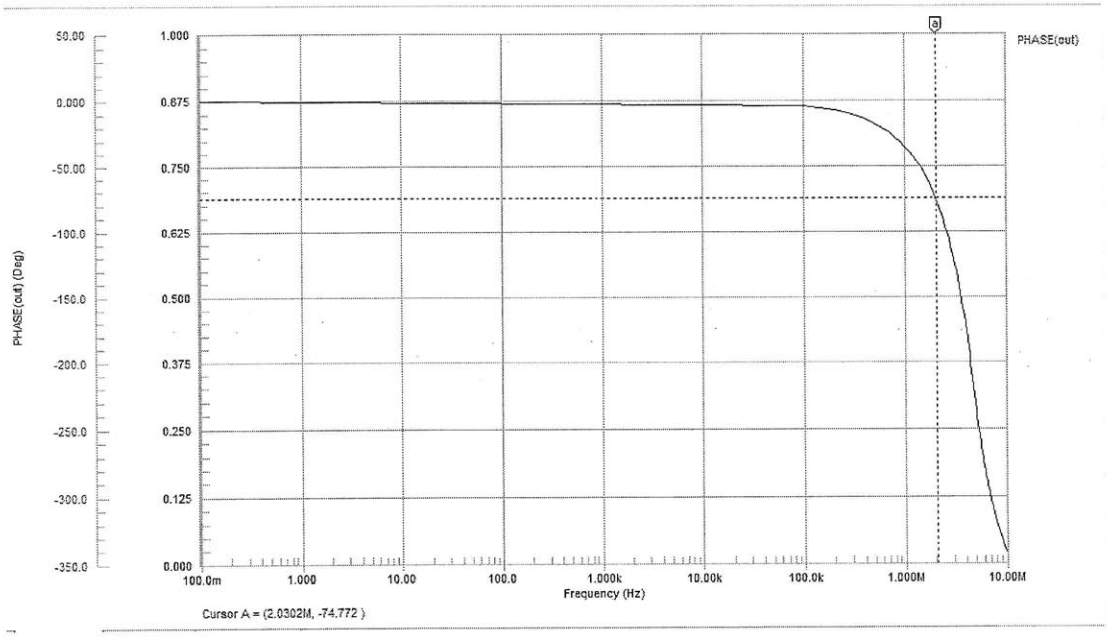

Figure 9-9: Phase bode plot of the output of the simulated circuit.

9.8 Circuit Fabrication and Testing

After simulation and getting a good estimate of the bandwidth of the photo detector amplifier circuit design, we proceeded to layout the circuit for fabrication.

The layout is made to be as small as possible. The entire circuit is routed into a 2 layer printed circuit board (PCB) that is 2cm by 2cm.

The PCB layout is routed so that the traces between the leads of the quadrant photodiode are as near to the first stage transimpedance amplifiers as possible. This is to reduce the potential of noise that is attributed to long copper traces. Decoupling capacitor are also placed right beside the supply pins of all operational amplifiers, instrumentation amplifiers and precision voltage reference. This is to ensure that noise contributed by the positive and negative power supply is reduced to a minimum.

All unused PCB area is also flooded with a ground polygon plane on both the layers so that external noise interference can be reduced as a large ground plane forms a small coupling between itself and neighboring traces, thereby reducing high-frequency energy. Figures 9-10 and 9-11 are the top and bottom layer layout of the PCB respectively. The supplier is Sunstone Circuits Inc. and the address is included in appendix B.

The 5 way connector of the PCB circuit includes the external positive and negative 15V input (red and yellow wires), ground (black wire), top and bottom output signal from the first stage transimpedance amplifiers (white and green wires) and the top minus bottom signal from the instrumentation amplifier (white wire). Figure 9-12 is shows the actual assembled circuit that is used in the optical subsystem.

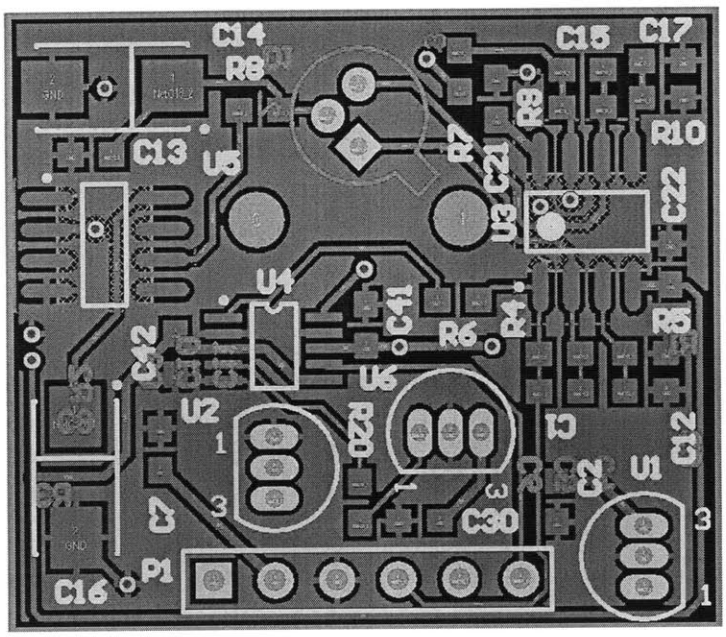

Figure 9-10: Top layer of the printed circuit board layout.

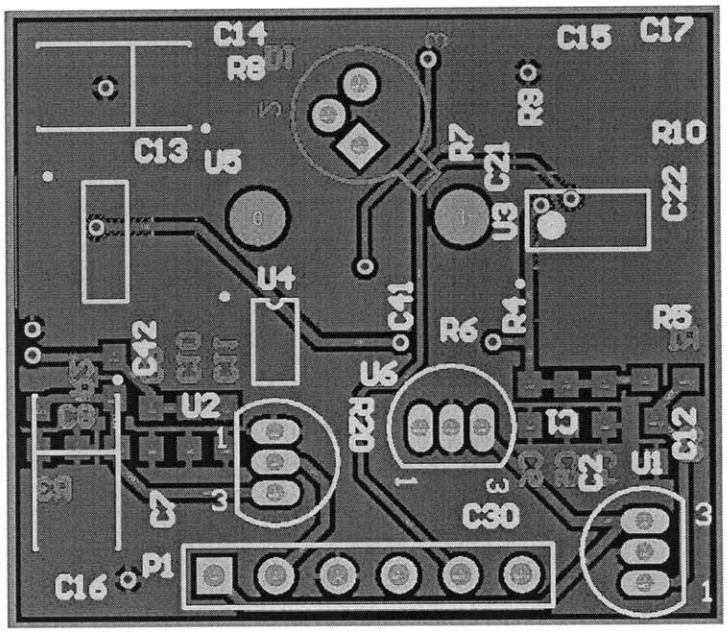

Figure 9-11: Bottom layer of the printed circuit board layout.

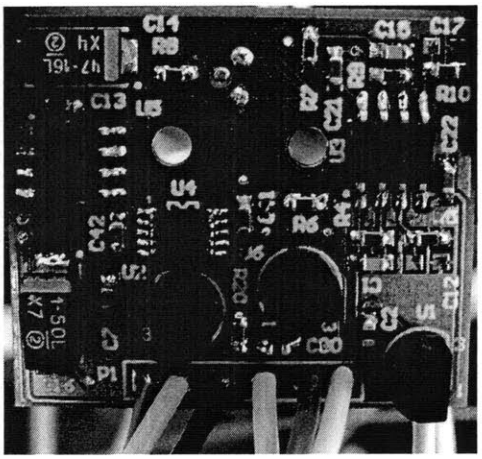

Figure 9-12: Actual assembled circuit of the photodetector design.

9.9 Summary

In this chapter, we presented a quadrant photodiode detector circuit that has a high 2MHz bandwidth. This high bandwidth is required since we are using small cantilevers with resonance frequency of approximately 2 MHz. Typical resonance frequency of standard cantilevers are in the range of hundred of KHz.

A simulation of the circuit is carried out and presented and the fabrication, testing and deployment of the circuit is also documented.

Chapter 10

Experimental Results

10.1 Introduction

This chapter will describe the experiments that are carried out and the setup needed. The range and dynamics of the integrated optical subassembly and the X-Y scanner, optical sensitivity, thermal tune, error sensitivity, and imaging are presented.

10.2 Scanner Range

The scanner range experiment shows how far the scanner can move in the X and Y directions. This result determines the size of the image that we can scan.

The range experiment for the X-Y scanner that is integrated with the optical subassembly is conducted by measuring the maximum displacement of the X-Y scanner (i.e. integrated with optical subassembly) when the scanner is in operation.

The range is measured with an interferometer with a 0.1nm resolution in the X axis and the Y axis. The range for both the X and Y axes are the same.

Figure 10-1 shows the range of the integrated X-Y scanner and optical subassembly. The voltage applied to the scanner piezos are from 0 to 150 volts. This X-Y scanner moves a total range of 16 microns. The reduced range is due to the larger

central stage. The central stage is enlarged to accommodate the optical subassembly.

After taking the range for the integrated scanner and optical subassembly, we then take the range for just the scanner.

The optical subassembly is then taken apart from the X-Y scanner and the range of the scanner only is taken again. The experiment shows that the range of the X-Y scanner by itself is also 16 microns.

This means that the lever based optical subassembly does not affect the range of the X-Y scanner when the optical subassembly is integrated into the X-Y scanner.

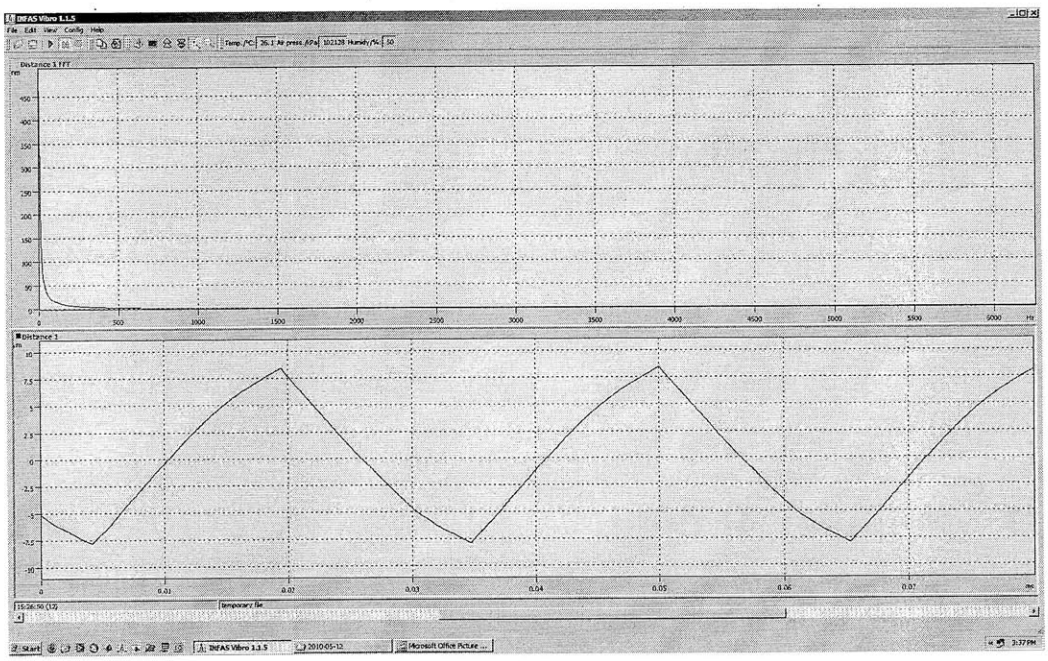

Figure 10-1: Range of scanner measured with interferometer.

10.3 Scanner Dynamics

The scanner dynamics experiment shows how the X-Y scanner range is affected by different input frequencies. This result determines how fast we can scan an image.

To identify the dynamics of the X-Y scanner for the X-Y scanner that is integrated with the optical subassembly, experiments were conducted by measuring its range while the X-Y scanner is in operation. Using the system identification toolbox in Matlab, we fit a model to represent the frequency response of the integrated AFM.

Similar to the range experiment, we use an interferometer with a 0.1nm resolution.

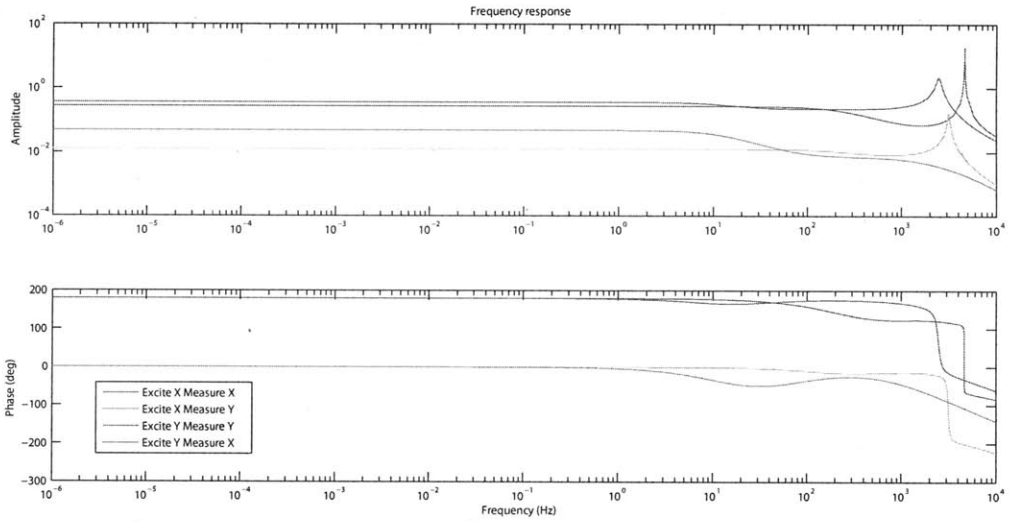

Figure 10-2: Bode plot of the range of the X-Y scanner as a function of frequency.

The results of the scanner dynamics are shown in figure 10-2. For the amplitude plot, the Y axis is amplitude and the X axis is the frequency in hertz. The dotted line and the solid line at the top of the amplitude plot are the amplitude bode plots of the X and Y axis when the scanner is excited in the X and Y directions respectively. The dashed and the dashed and dotted lines at the bottom are the amplitude bode plots of the X and Y axis when the scanner is excited in the Y and X directions respectively. Similarly, the phase of the corresponding lines are shown in the phase

bode plots.

From the bode plot of the dynamics of the scanner integrated with the optical subassembly, it shows that the dynamics of the scanner is not affected by the optical subassembly. This is because the bode plot shows no resonance at frequencies at and below 1KHz, which is the speed that the X-Y scanner will operate at.

10.4 Optical Sensitivity

The optical sensitivity is how sensitive the optical subsystem is to a change in the deflection of the cantilever. The optical sensitivity will determine the quality of the image taken by the integrated optical subassembly and the X-Y scanner.

To conduct the optical sensitivity experiment, we lowered the integrated optical subassembly and the X-Y scanner to approach the sample by controlling the stepper motor of the approach mechanism. When the cantilever has approached the sample, the Z topography piezos is extended by 1.4 microns and the deflection of the cantilever is captured by the photodiode detector. The output is a voltage from the photodiode detector circuit. The force distance curve is done using the force distance curve function provided in the Anfatec controller. This produces the force distance curve plot and is used to determine the optical sensitivity.

The optical sensitivity of the optical subassembly is shown in Figure 10-3. From the results, we can see that the optical sensitivity is 1.14 microns per volt.

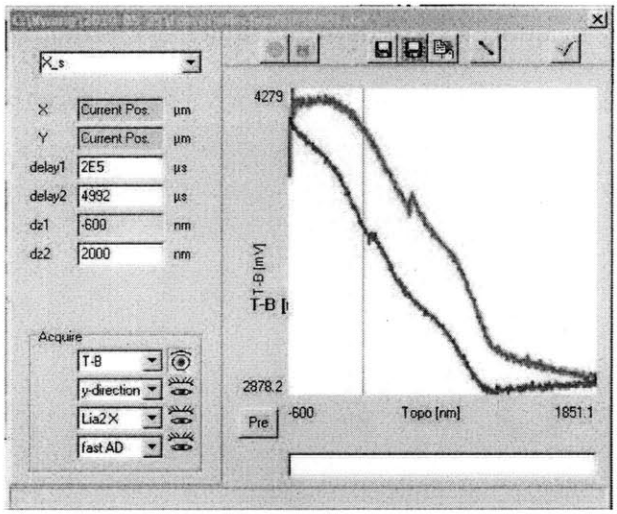

Figure 10-3: Force distance curve of the optical subassembly.

10.5 Thermal Tune

A thermal tune is an experiment conducted to find out the thermal noise that exists when the cantilever is not oscillating and the X-Y scanner is not scanning. The experiment is conducted over a short period of time and the amplitude of the signal is read from the optical subassembly. A fourier transform for the short period of signal recorded previously is carried out and a plot of the amplitude versus the frequency is presented in a graph. This result will show how susceptible the optical subassembly is to noise.

To perform the thermal tune experiment, the integrated optical subassembly and the X-Y scanner is retracted and the cantilever is lifted from the sample. This ensures that the cantilever is not in contact with the sample. The thermal tune function provided in the Anfatec controller software allows us to conduct a thermal tune of the optical subassembly and the cantilever as described in the previous paragraph.

Figure 10-4 is a thermal tune of the optical subassembly taken with the Anfatec controller. As can be seen from figure 10-4, the amplitude is approximately 116.8

microvolts (root-mean-square) and the frequencies are around 162.5KHz. It is near to the resonance frequency of the cantilever that was mounted (i.e. 150 KHz) [14].

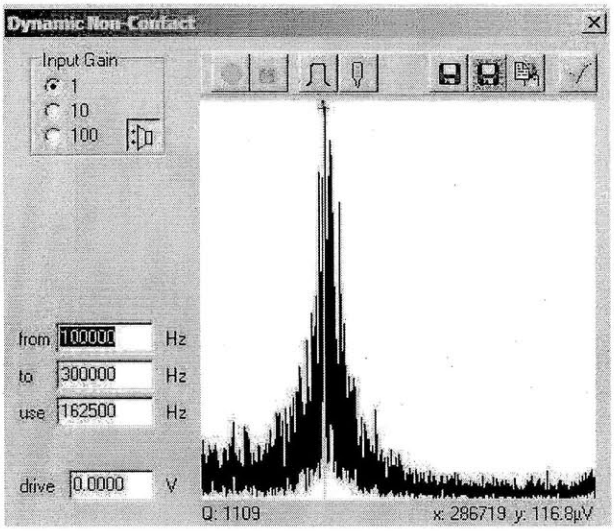

Figure 10-4: Thermal tune of the optical subassembly.

10.6 Error Sensitivity

The error sensitivity is how susceptible to error the optical subassembly is when the optical subassembly tilts. This can be captured by taking the tuning curve of the cantilever at various positions of the entire range of the X-Y scanner.

In this error sensitivity test, we perform 2 experiments (i.e. static error sensitivity and dynamic error sensitivity).

In the static error sensitivity experiment, the scanner is moved, in steps of 5 microns, from the center position to the full range of the X-Y scanner (i.e. $\pm$ 25 microns in both the X and Y directions.) The $\pm$ 25 microns makes a total of 50 microns (i.e. the full range of the scanner).

In the dynamic error sensitivity experiment, we first obtain a good tuning curve of the resonance frequency of the cantilever using the Anfatec controller. While the Anfatec controller is continuously taking the tuning curve of the cantilever, we start

the scanning (i.e. the X-Y scanner moves in both the X and Y directions) to conduct the dynamics error sensitivity experiment.

If the laser spot falls onto the back of the cantilever (i.e. the error sensitivity is acceptable), the tuning curve will not change significantly when the scanner is in operation .

In the static error sensitivity experiment, the tuning curve is plotted as the scanner is moved in steps of 5 microns.

The results shown are the tunning curve of the cantilever as the scanner is moved to different positions, in steps of 5 microns (e.g. 5, 10, 15, 20, 25 microns), of the 50 micron scanner range statically. The results show that the cantilever is tracked successfully and the amplitude and frequency of the cantilever is captured.

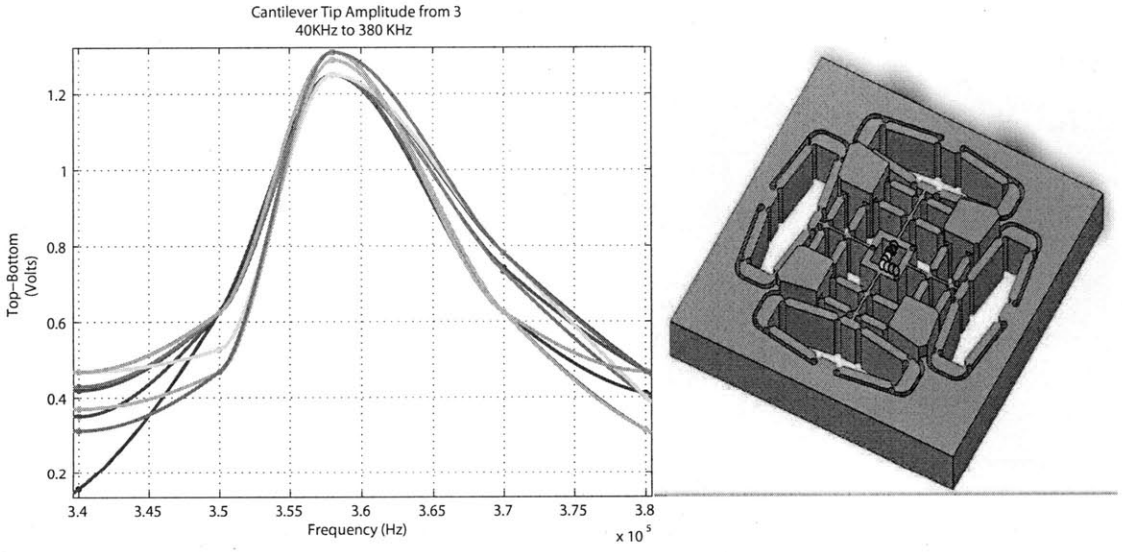

Figure 10-5: Tuning curve of the cantilever at various X and Y coordinates of the scanner.

The previous experiment shows the error sensitivity of the integrated optical sub-assembly and the X-Y scanner in static steps. The next experiment shows the tuning curve of the scanner as the scanner is in operation (i.e. X-Y scanner moves in the X and Y direction in a raster fashion).

Figure 10-6 shows the tuning curve of the cantilever taken with the Anfatec software. From figure 10-6, we can see that the tuning curve of the cantilever does not change when the X-Y scanner is in operation.

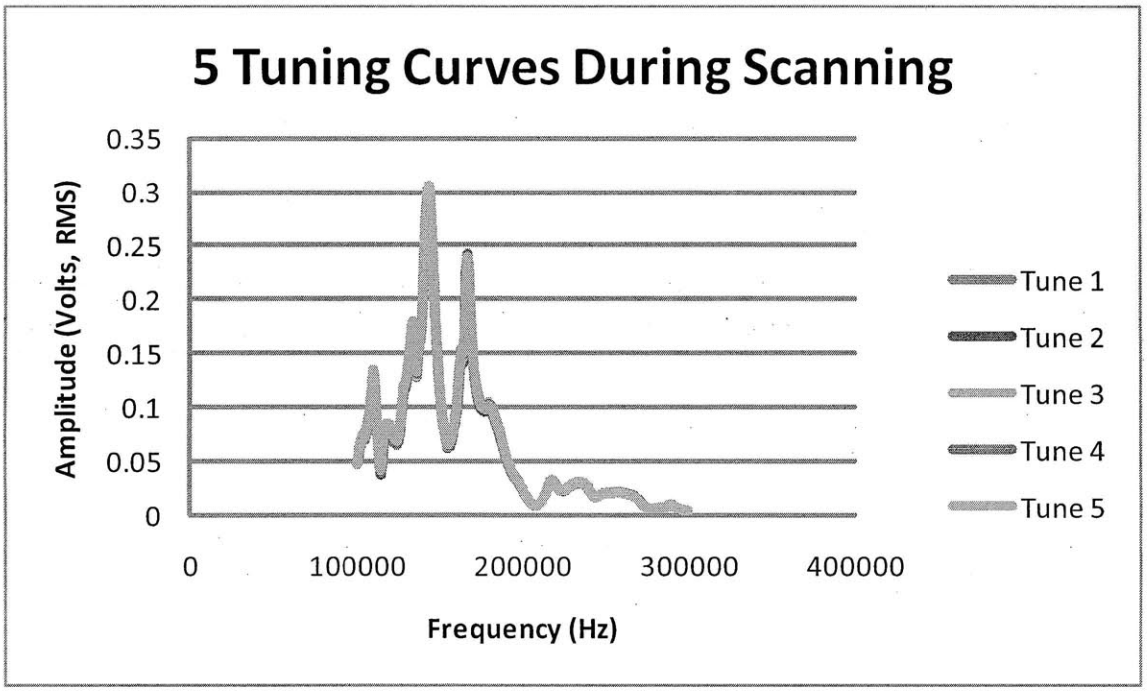

Figure 10-6: Tuning curve of cantilever when scanner is scanning.

10.7 Imaging Results

The imaging experimental setup of the optical subassembly integrated with the X-Y scanner is shown in figure 10-7. This experimental setup also includes the approach mechanism which allows the scanner to be lowered to the sample to be scanned in nanometer steps.

For the imaging experiment, we connect the Anfactec controller to the AFM scanner and optical subassembly. The Anfatec controller provides the input signals to command the X-Y scanner to scan the sample in the X and Y directions. The quadrant photodiode detector signal that is output from the photodiode detector circuit is feedback into the Anfatec controller.

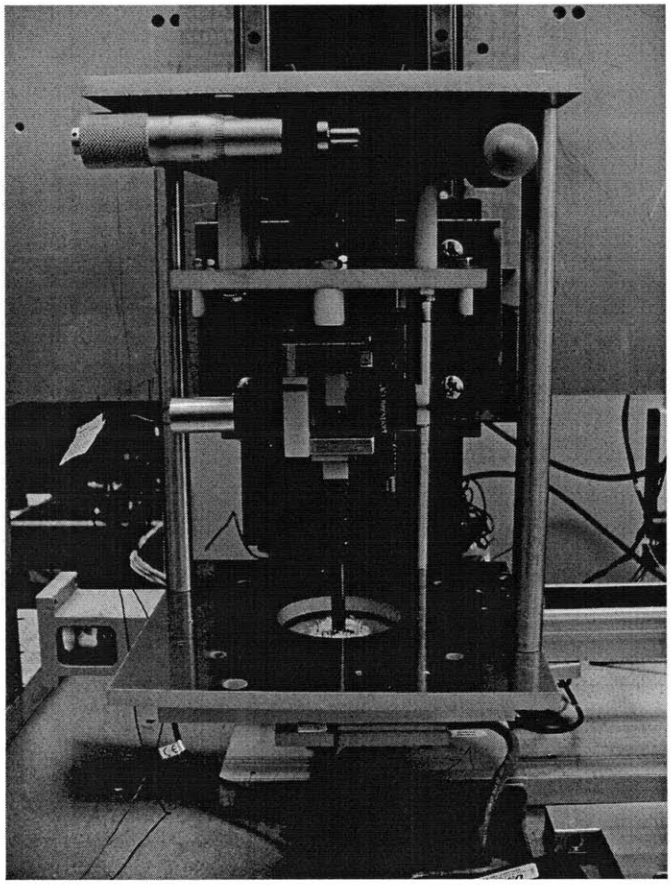

Figure 10-7: Integrated optical subassembly and X-Y scanner mounted on approach mechanism for imaging.

Finally, we used the integrated optical subassembly and the X-Y scanner to take an image of a triangular grating. The grating that we imaged has a 3 micron step pitch and a 1.8 micron step height.

Figure 10-8 is the image that is taken with our AFM. The range of the scanner is set to 8 microns and the image that is shown is the topography of the grating.

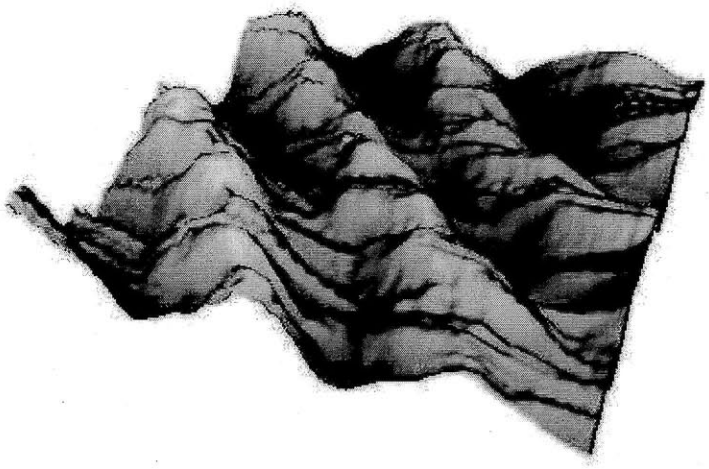

Figure 10-8: Image of a grating.

10.8 Summary

This chapter summarizes the experimental procedure and presents the experimental results that are obtained. From the results, we have shown that the cantilever is tracked successfully as the scanner is scanning. This can be accomplished because the laser spot is small enough to fall on the cantilever tip and the optical subassembly has acceptable error sensitivity and optical sensitivity. It shows that this design is acceptable and has an error sensitivity and optical sensitivity that is suitable for our application.

Chapter 11

Conclusions and Closing Remarks

11.1 Introduction

This chapter summarizes the entire thesis and suggest future work that can be done.

11.2 Problem Statement

The main challenge of this optical deflection sensing system is the tracking of a cantilever mounted on an AFM X-Y scanner that is scanning at 1kHz and at a large range of 50 microns.

In addition to the large range and high speed, we also need to be able to focus a laser spot size that is under 10 microns onto the back of the cantilever. This is because we are using cantilevers that are only 10 microns in width.

Furthermore, there is a need to facilitate initial adjustment of the laser focus point whenever a new cantilever is mounted. The range for initial adjustment needs to be sufficient for initial adjustment setup.

The above mentioned requirements are conflicting and a trade-off must be made to satisfy all these requirements simultaneously.

11.3 Thesis Contributions

The contributions of this thesis are the design of 2 novel optical cantilever tracking methods and the development of a high bandwidth quadrant photodiode detector circuit.

For the lever method, we conducted the range, statics, dynamics, error sensitivity and optical sensitivity experiments to show that the lever method of tracking the cantilever is achieved. The lever method also allows initial adjustment of the laser spot onto the back of the cantilever when a new cantilever is mounted.

For the fiber collimator method, we showed that we are able to track the cantilever and also adjust the cantilever holder instead of adjusting the optical subassembly during initial setup.

Both methods proved to be feasible and can be explored further to optimize the designs.

11.4 Future Work for Lever and Fiber Collimator Method

This section discuses future work that can be carried out to improve the current setup and is divided into four subsections (i.e. Optics, Initial Adjustment and Photodetector and Circuit Design). These suggestions are applicable to both the lever method and the fiber collimator method.

11.4.1 Optics

To make the optical subassembly lighter, we need to reduce the weight of the adjustment mechanisms. The precision adjustment mechanisms for aligning the optics contribute most to the weight of the optical subassembly. To reduce the overall

weight of the optical subassembly, we can either make these precision adjustment mechanisms smaller or totally eliminate these mechanisms by eliminating the need for optics alignment (e.g. pre-aligning the optics components and bonding them together).

11.4.2 Initial Adjustment

There is always a need to adjust both the optical subassembly and the photodiode detector whenever a new cantilever is mounted. This process is repetitive and tedious.

To automate this initial adjustment process, we can make use of piezos to replace these heavy precision adjustment mechanisms and automatically adjust the connected optics components (i.e. laser source and photodiode detector) so that the focused laser beam fall onto the cantilever and the reflected laser beam from the cantilever is centered about the photodiode detector. This can be applied both to the lever method and the fiber collimator method.

11.4.3 Photodetector

To eliminate the adjustment mechanism of the photodiode detector, we propose the use of an array of small photodetectors in series. The array of photodetectors allow the automatic centering of the reflected laser spot by averaging the intensity of the array of linear photodetectors.

Another suggestion is to incorporate a summing operational amplifier to output the sum of the intensity of the quadrant photodiode and the normalized signal of the top minus bottom signal (i.e. by dividing the top minus bottom signal by the sum signal). The normalized signal of the top minus bottom signal may provide a better measure of the cantilever deflection.

11.5 Summary

This chapter summarizes the implementation of 2 novel methods to track a cantilever mechanically (i.e. lever method and fiber collimator method). We solved various problems that we faced in optics, mechanical design for alignment and adjustment, decoupling the resonances of the optics subassembly from the resonances of the scanner and designed a quadrant detector circuit that has a high bandwidth.

Both methods are able to the track the cantilever dynamically and the system has acceptable error sensitivity and optical sensitivity. An image of a grating is taken with the integrated X-Y scanner and optical subassembly for the lever method.

Finally, we listed the improvements that can be made on the existing system to obtain a better performance.

Appendix A

Drawings

This section contains selected drawings for the parts manufactured.

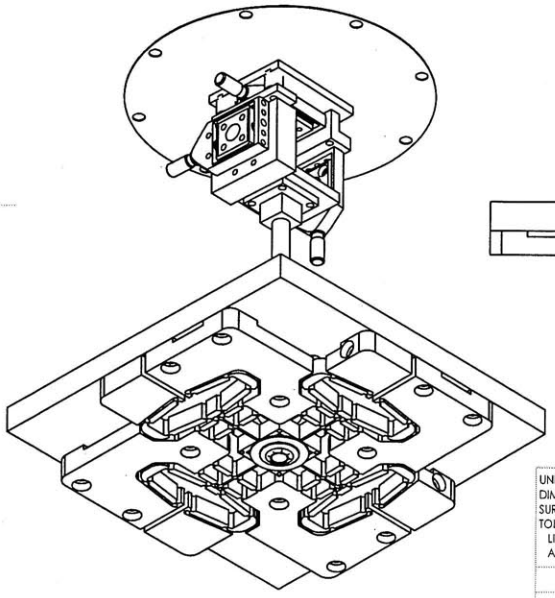

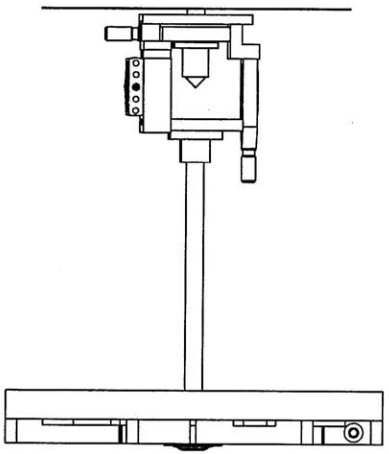

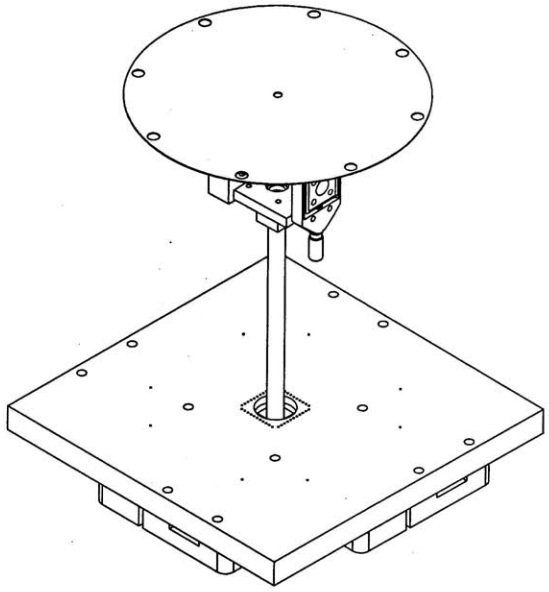

UNLESS OTHERWISE SPECIFIED: DIMENSIONS ARE IN MILLIMETERS SURFACE FINISH: TOLERANCES: LINEAR: ANGULAR:	FINISH:	DEBUR AND BREAK SHARP EDGES	DO NOT SCALE DRAWING / REVISION

	NAME	SIGNATURE	DATE
DRAWN			
CHK'D			
APPV'D			
MFG			
Q.A			

MATERIAL:

WEIGHT:

TITLE:

DWG NO. Assem01

A4

SCALE:1:5

SHEET 1 OF 1

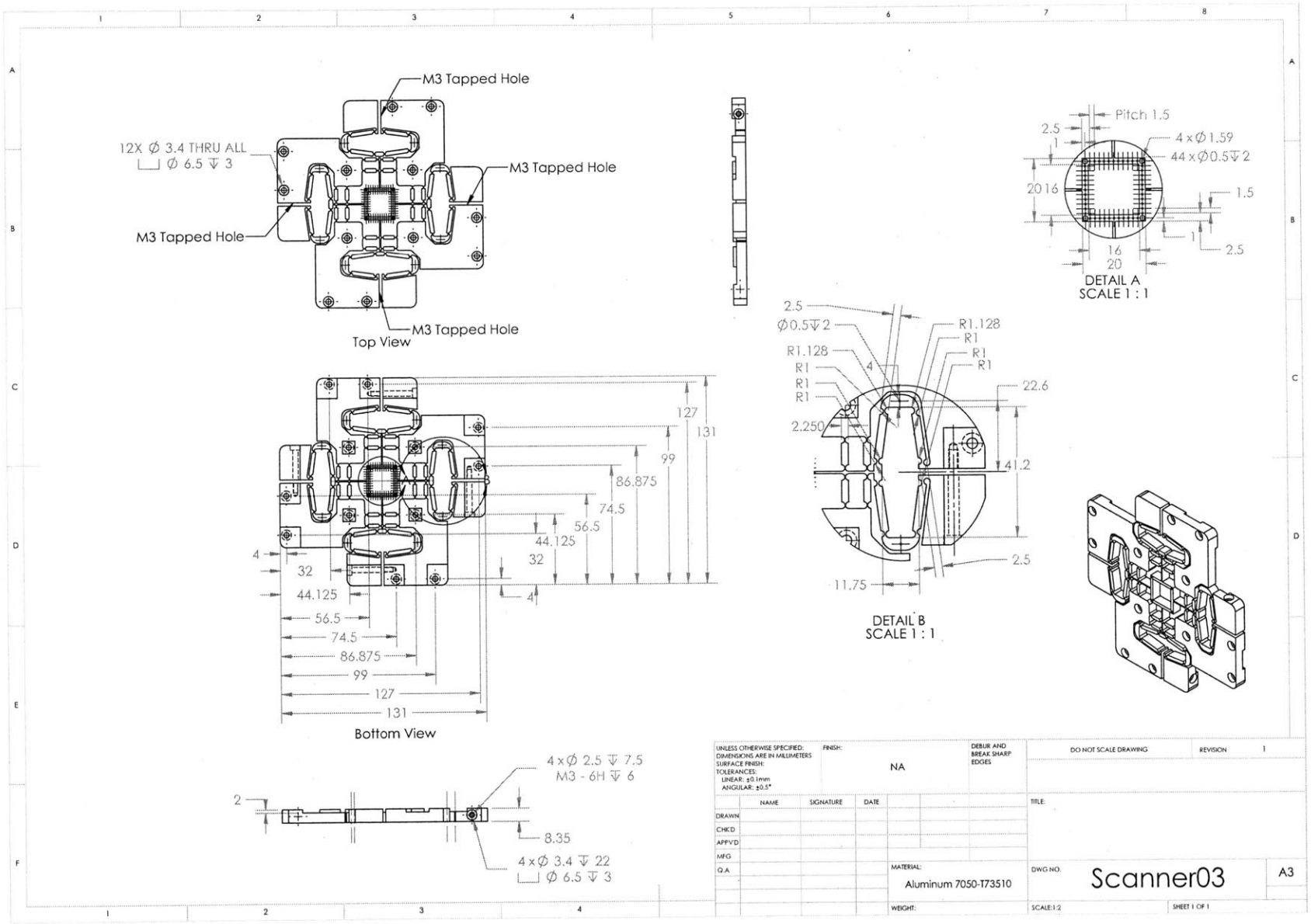
M3 Tapped Hole
12X Ø 3.4 THRU ALL
⌴ Ø 6.5 ↧ 3
M3 Tapped Hole
M3 Tapped Hole
M3 Tapped Hole
Top View
Pitch 1.5
2.5
4 x Ø 1.59
44 x Ø 0.5 ↧ 2
20 16
1.5
1
2.5
16
20
DETAIL A
SCALE 1 : 1
2.5
Ø 0.5 ↧ 2
R1.128
R1
R1
R1
R1
R1.128
R1
R1
4
22.6
2.250
41.2
2.5
11.75
DETAIL B
SCALE 1 : 1
127
131
99
86.875
74.5
56.5
44.125
32
4
4
32
44.125
56.5
74.5
86.875
99
127
131
Bottom View
4 x Ø 2.5 ↧ 7.5
M3 - 6H ↧ 6
2
8.35
4 x Ø 3.4 ↧ 22
⌴ Ø 6.5 ↧ 3
UNLESS OTHERWISE SPECIFIED:
DIMENSIONS ARE IN MILLIMETERS
SURFACE FINISH:
TOLERANCES:
LINEAR: ±0.1mm
ANGULAR: ±0.5°
FINISH:
NA
DEBUR AND BREAK SHARP EDGES
DO NOT SCALE DRAWING
REVISION 1
NAME
SIGNATURE
DATE
DRAWN
CHK'D
APPV'D
MFG
Q.A
TITLE:
MATERIAL:
Aluminum 7050-T73510
WEIGHT:
DWG NO.
Scanner03
A3
SCALE:1:2
SHEET 1 OF 1

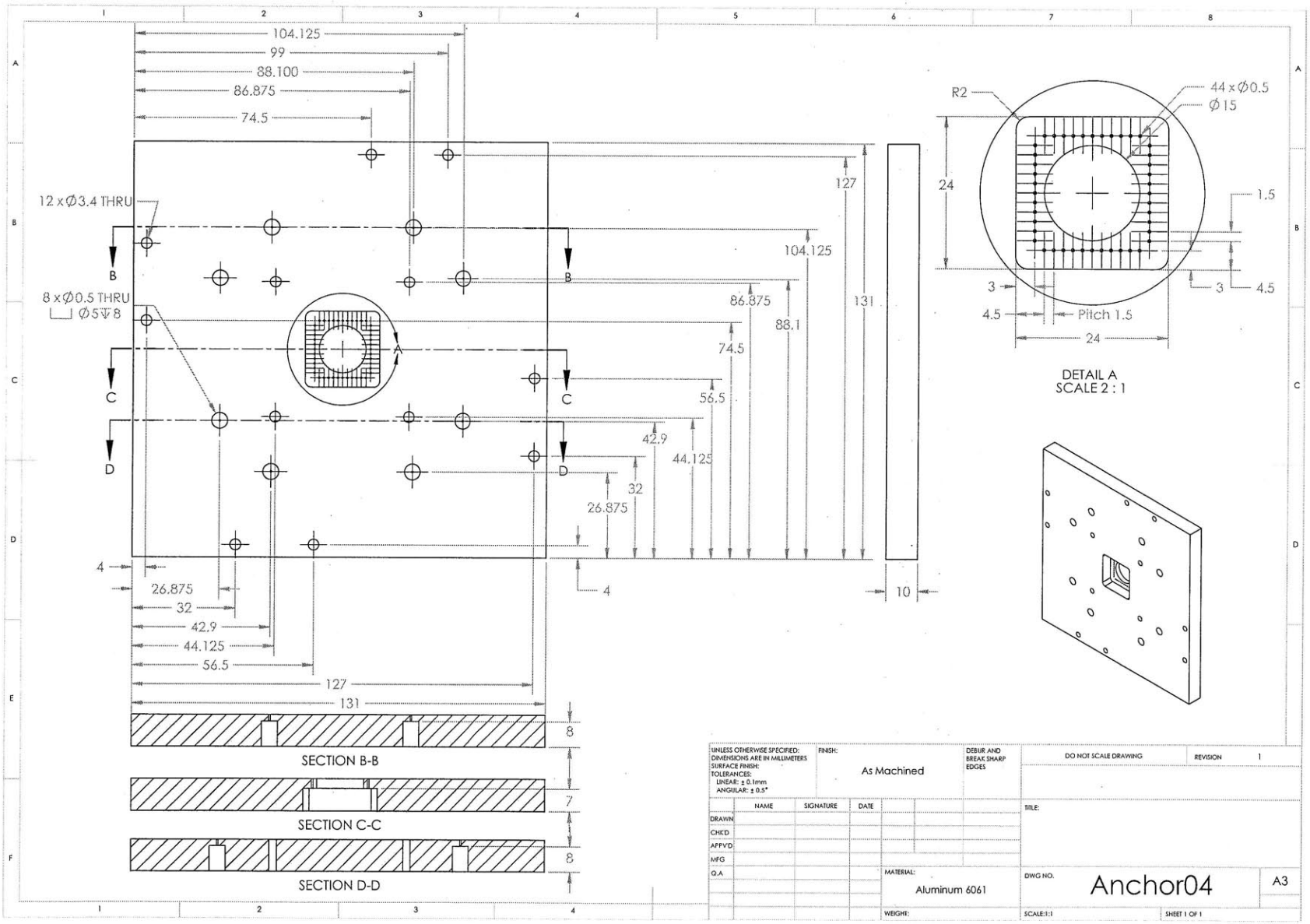
104.125
99
88.100
86.875
74.5
12 x Ø3.4 THRU
8 x Ø0.5 THRU
⌴ Ø5↧8
B
C
D
A
127
104.125
86.875
88.1
74.5
56.5
42.9
44.125
32
26.875
131
4
10
R2
44 x Ø0.5
Ø15
24
1.5
3
4.5
Pitch 1.5
DETAIL A
SCALE 2 : 1
SECTION B-B
SECTION C-C
SECTION D-D
8
7
UNLESS OTHERWISE SPECIFIED:
DIMENSIONS ARE IN MILLIMETERS
SURFACE FINISH:
TOLERANCES:
LINEAR: ± 0.1mm
ANGULAR: ± 0.5°
FINISH:
As Machined
DEBUR AND BREAK SHARP EDGES
DO NOT SCALE DRAWING
REVISION 1
NAME
SIGNATURE
DATE
DRAWN
CHK'D
APPV'D
MFG
Q.A
MATERIAL:
Aluminum 6061
WEIGHT:
TITLE:
DWG NO.
Anchor04
A3
SCALE:1:1
SHEET 1 OF 1

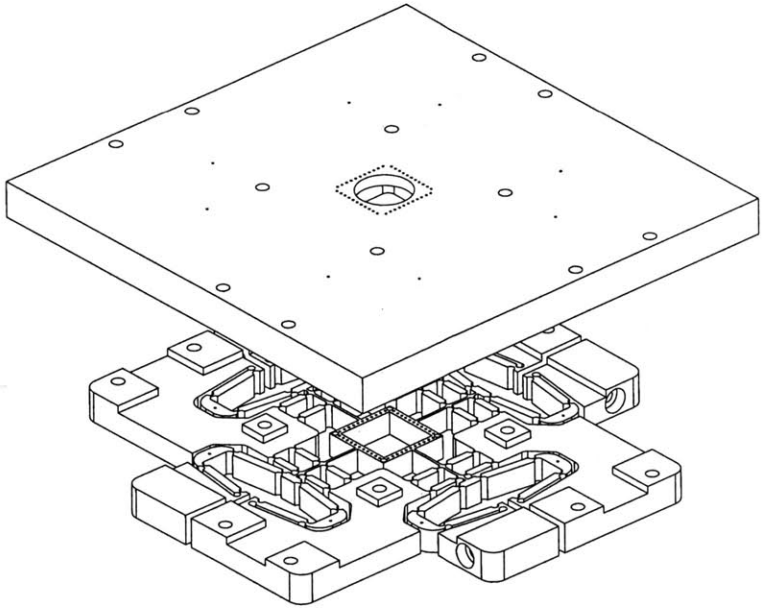

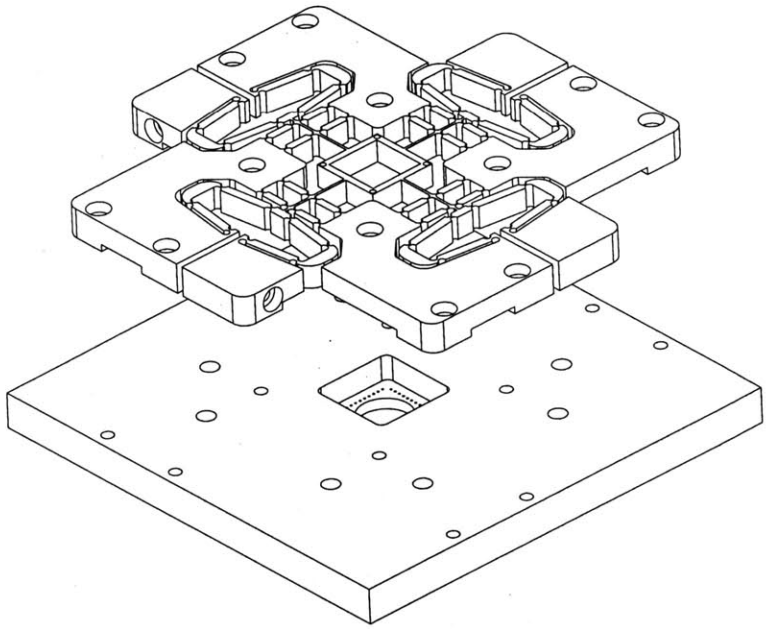

UNLESS OTHERWISE SPECIFIED: DIMENSIONS ARE IN MILLIMETERS SURFACE FINISH: TOLERANCES: LINEAR: ANGULAR:		FINISH:			DEBUR AND BREAK SHARP EDGES	DO NOT SCALE DRAWING	REVISION
	NAME	SIGNATURE	DATE			TITLE:	
DRAWN							
CHK'D							
APPV'D							
MFG							
Q.A				MATERIAL:		DWG NO. Assem3	A3
				WEIGHT:		SCALE:1:2	SHEET 1 OF 1

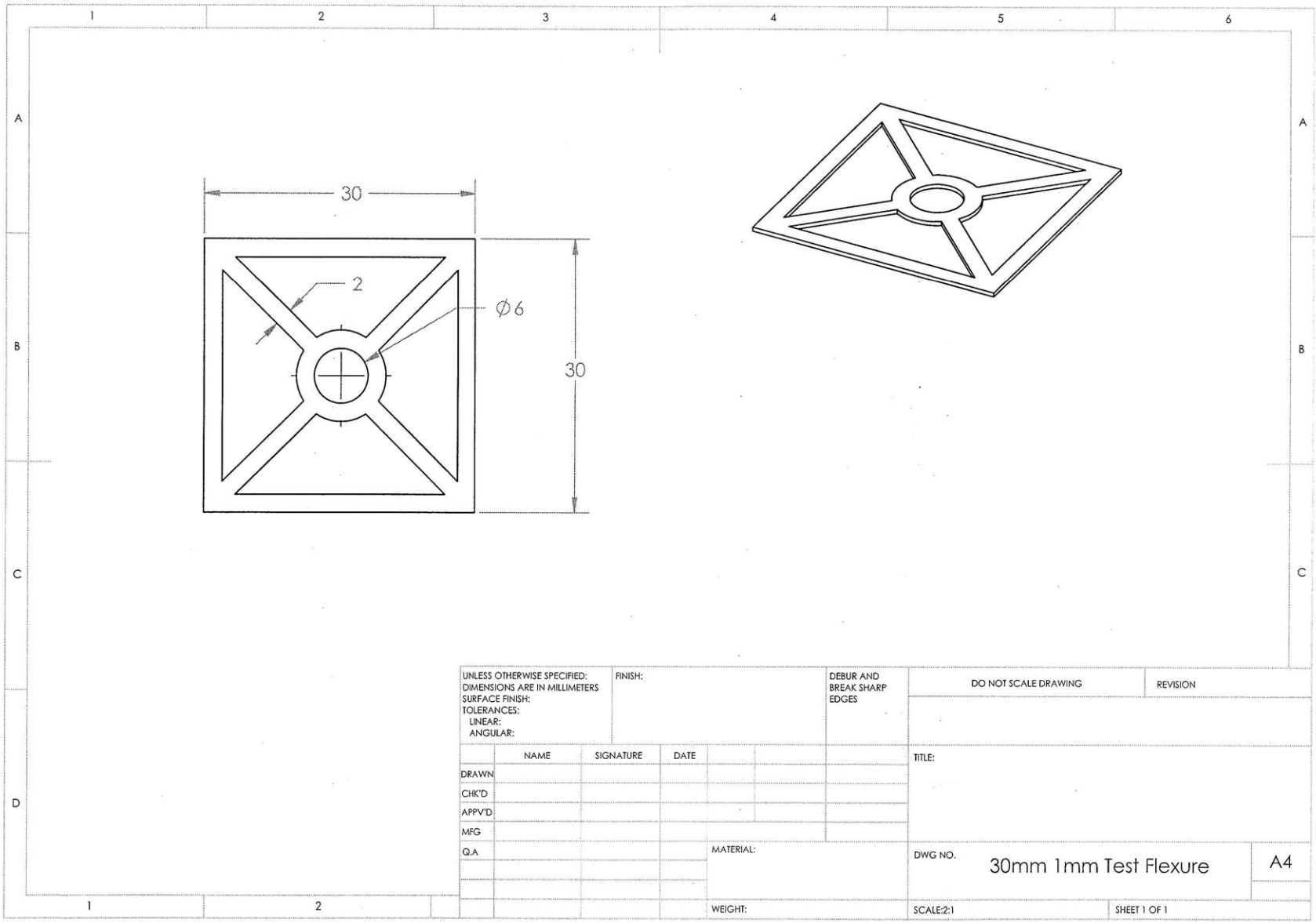
1
2
3
4
5
6
A
B
C
D
30
2
Ø6
30
UNLESS OTHERWISE SPECIFIED:
DIMENSIONS ARE IN MILLIMETERS
SURFACE FINISH:
TOLERANCES:
LINEAR:
ANGULAR:
FINISH:
DEBUR AND BREAK SHARP EDGES
DO NOT SCALE DRAWING
REVISION
NAME
SIGNATURE
DATE
DRAWN
CHK'D
APPV'D
MFG
Q.A
MATERIAL:
WEIGHT:
TITLE:
DWG NO.
30mm 1mm Test Flexure
A4
SCALE:2:1
SHEET 1 OF 1

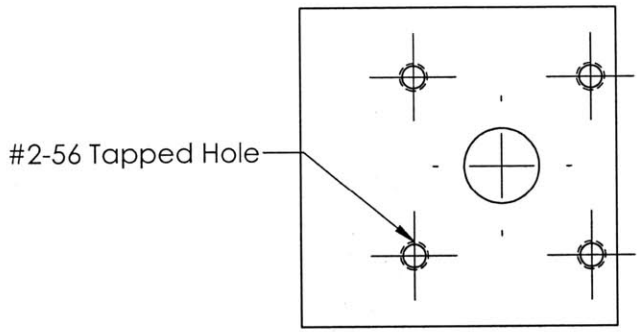

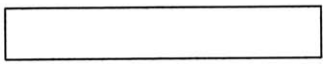

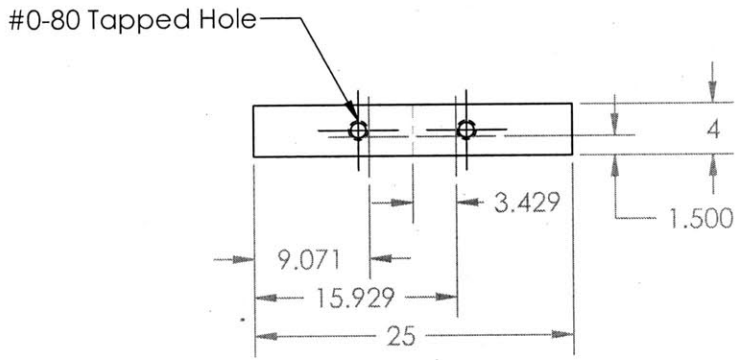

		UNLESS OTHERWISE SPECIFIED:		NAME	DATE
		DIMENSIONS ARE IN INCHES TOLERANCES: FRACTIONAL ± ANGULAR: MACH ± BEND ± TWO PLACE DECIMAL ± THREE PLACE DECIMAL ±	DRAWN		.
			CHECKED		
			ENG APPR.		
			MFG APPR.		
		INTERPRET GEOMETRIC TOLERANCING PER:	Q.A.		
		MATERIAL	COMMENTS:		
NEXT ASSY	USED ON	FINISH			
APPLICATION		DO NOT SCALE DRAWING			

TITLE:

SIZE	DWG. NO.	REV
A	Bottom Plate	
SCALE: 2:1	WEIGHT:	SHEET 1 OF 1

5 4 3 2 1

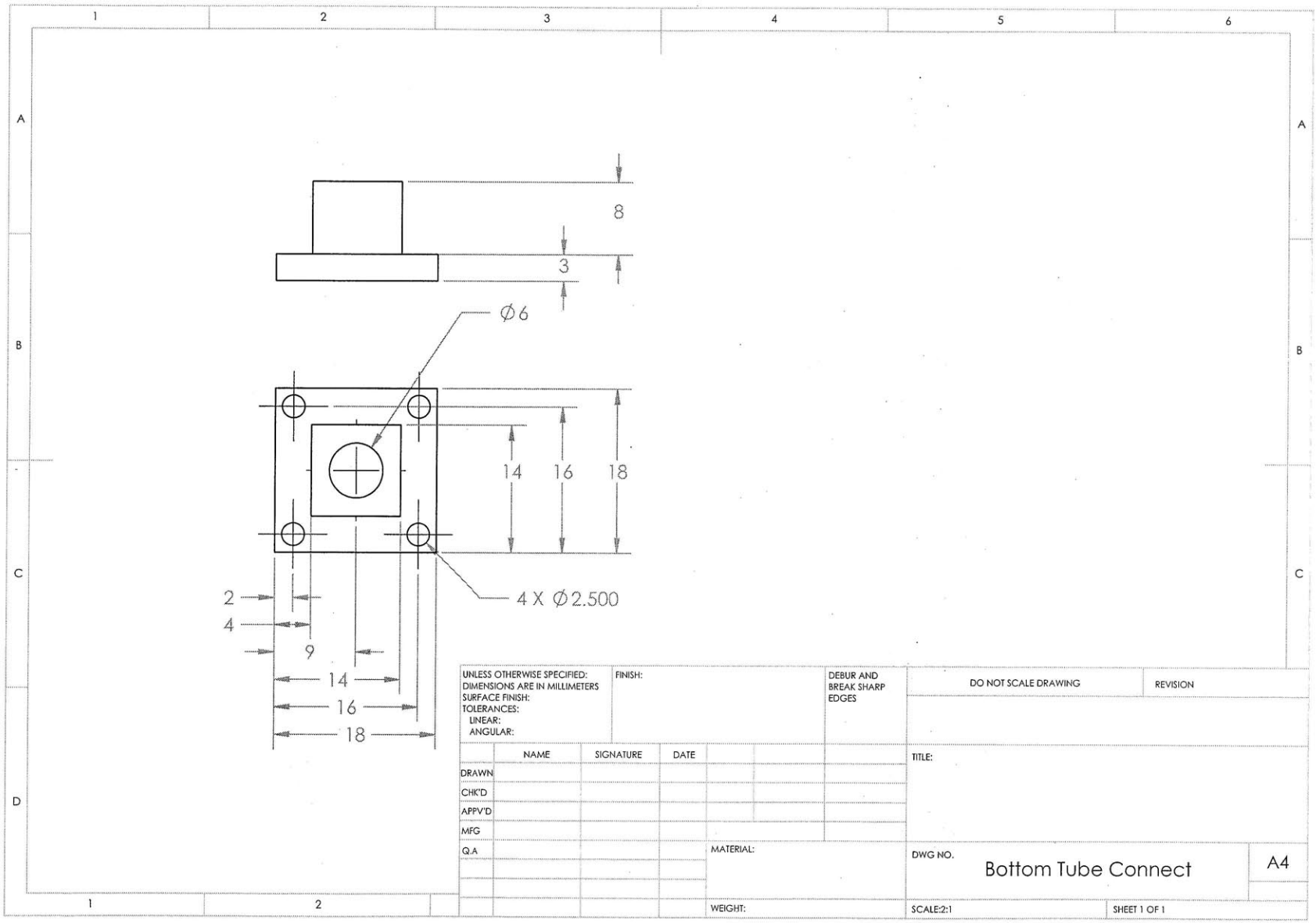
1
2
3
4
5
6
A
B
C
D
8
3
Ø6
14
16
18
2
4
9
14
16
18
4 X Ø2.500
UNLESS OTHERWISE SPECIFIED:
DIMENSIONS ARE IN MILLIMETERS
SURFACE FINISH:
TOLERANCES:
LINEAR:
ANGULAR:
FINISH:
DEBUR AND BREAK SHARP EDGES
DO NOT SCALE DRAWING
REVISION
NAME
SIGNATURE
DATE
DRAWN
CHK'D
APPV'D
MFG
Q.A
MATERIAL:
WEIGHT:
TITLE:
DWG NO.
Bottom Tube Connect
A4
SCALE:2:1
SHEET 1 OF 1

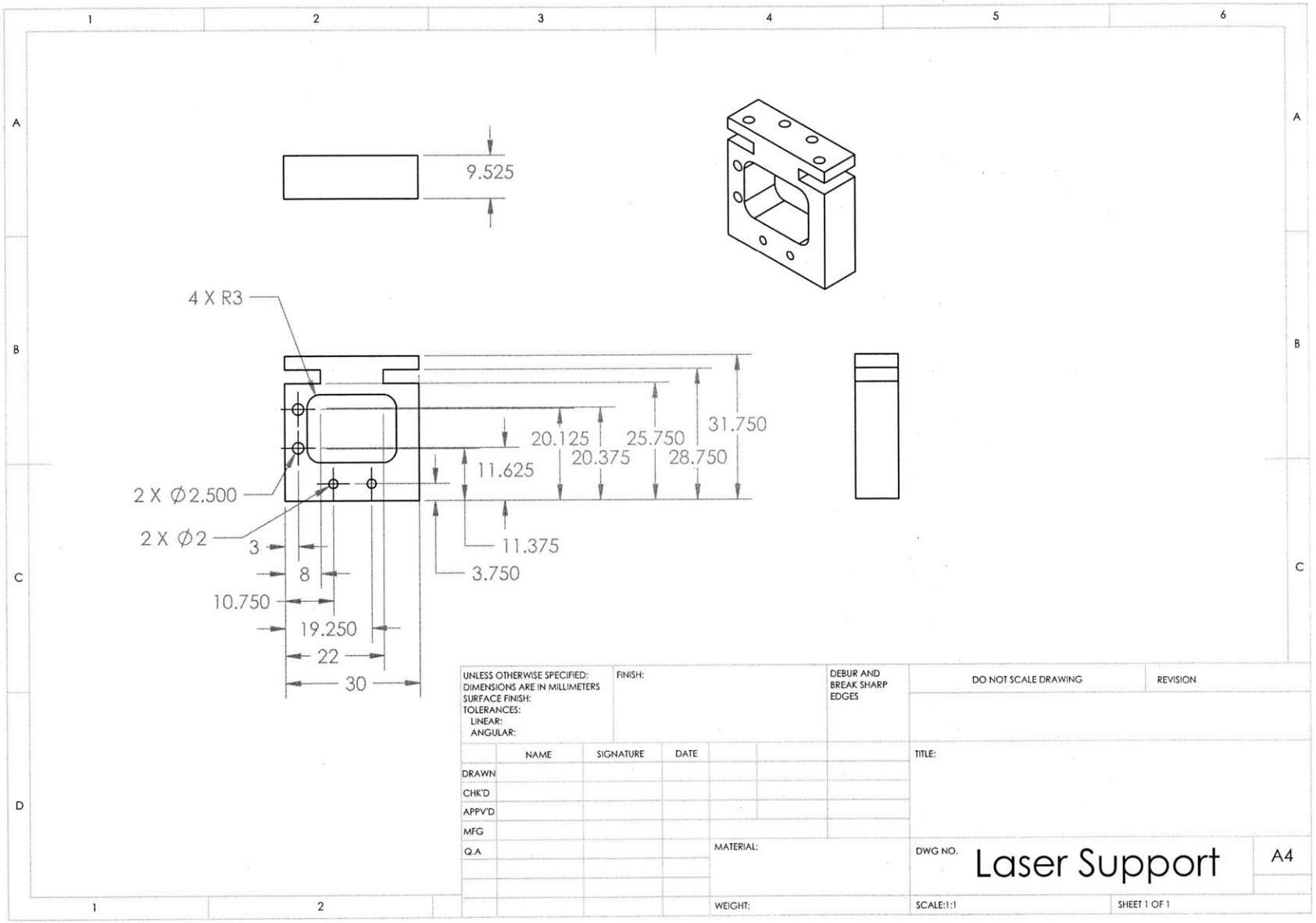
9.525
4 X R3
2 X Ø2.500
2 X Ø2
3
8
10.750
19.250
22
30
11.625
20.125
20.375
25.750
28.750
31.750
11.375
3.750
UNLESS OTHERWISE SPECIFIED:
DIMENSIONS ARE IN MILLIMETERS
SURFACE FINISH:
TOLERANCES:
LINEAR:
ANGULAR:
FINISH:
DEBUR AND BREAK SHARP EDGES
DO NOT SCALE DRAWING
REVISION
NAME
SIGNATURE
DATE
DRAWN
CHK'D
APPV'D
MFG
Q.A
MATERIAL:
WEIGHT:
TITLE:
DWG NO.
Laser Support
A4
SCALE:1:1
SHEET 1 OF 1

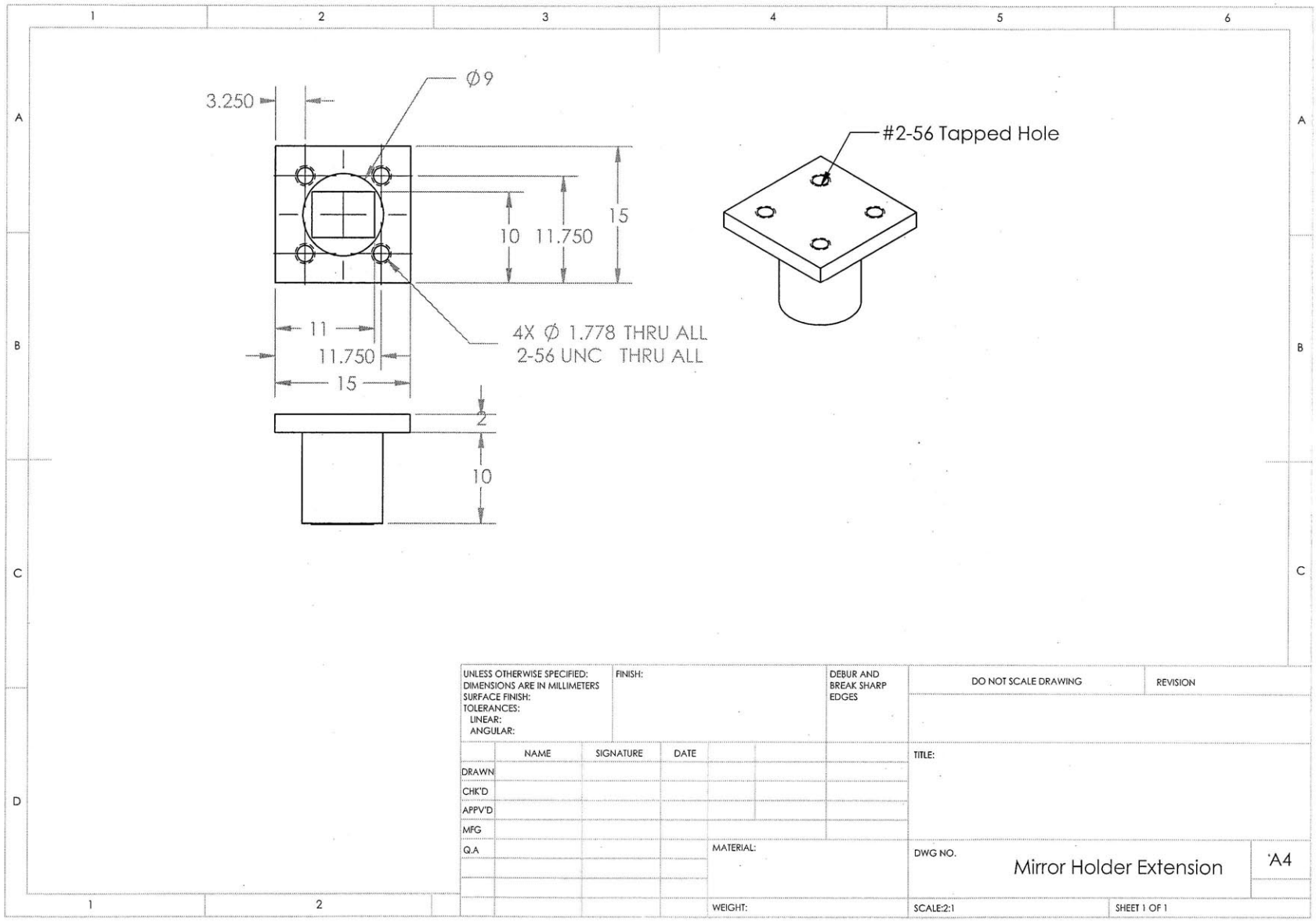
1
2
3
4
5
6
A
B
C
D
3.250
Ø9
15
10
11.750
11
11.750
15
2
10
4X Ø 1.778 THRU ALL
2-56 UNC THRU ALL
#2-56 Tapped Hole
UNLESS OTHERWISE SPECIFIED:
DIMENSIONS ARE IN MILLIMETERS
SURFACE FINISH:
TOLERANCES:
LINEAR:
ANGULAR:
FINISH:
DEBUR AND BREAK SHARP EDGES
DO NOT SCALE DRAWING
REVISION
NAME
SIGNATURE
DATE
DRAWN
CHK'D
APPV'D
MFG
Q.A
MATERIAL:
WEIGHT:
TITLE:
DWG NO.
Mirror Holder Extension
A4
SCALE:2:1
SHEET 1 OF 1

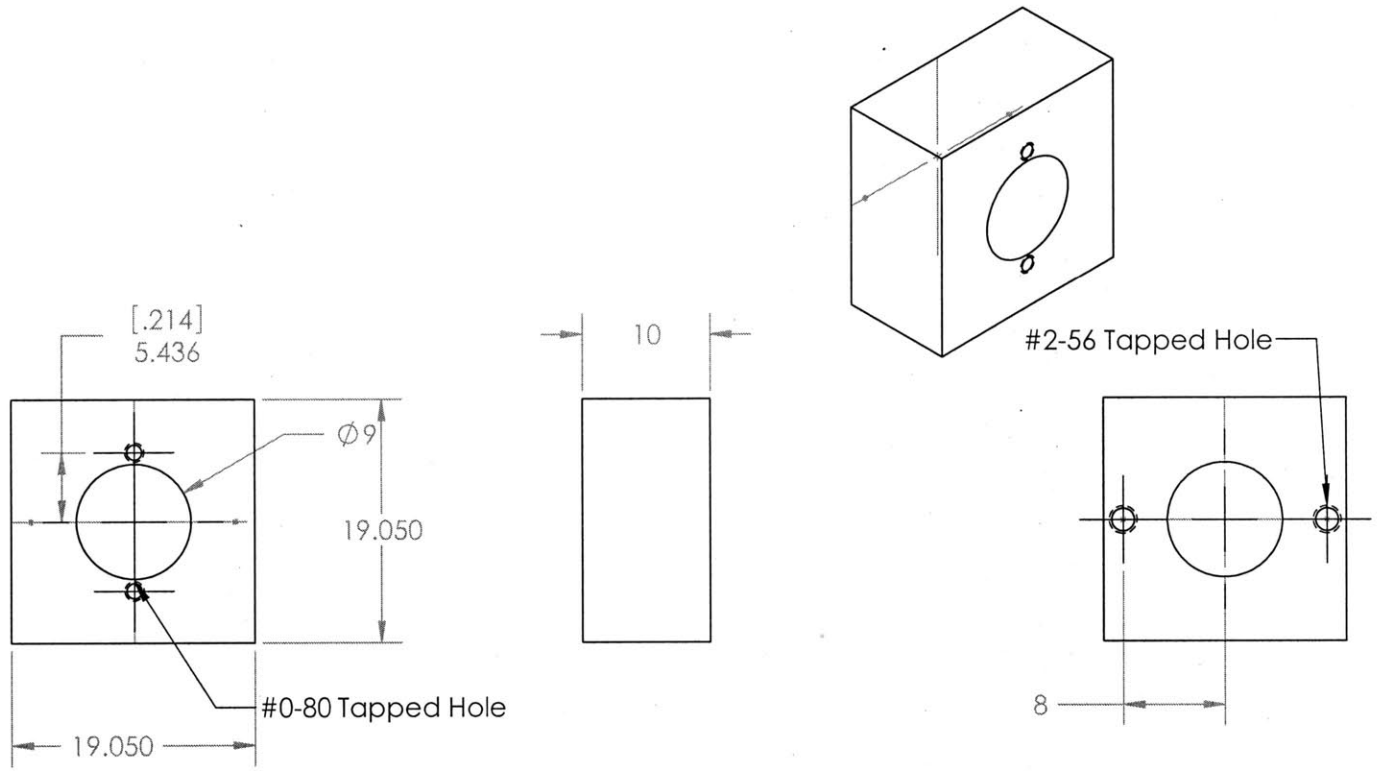

		UNLESS OTHERWISE SPECIFIED:		NAME	DATE
		DIMENSIONS ARE IN INCHES TOLERANCES: FRACTIONAL ± ANGULAR: MACH ± BEND ± TWO PLACE DECIMAL ± THREE PLACE DECIMAL ±	DRAWN		
			CHECKED		
			ENG APPR.		
			MFG APPR.		
		INTERPRET GEOMETRIC TOLERANCING PER:	Q.A.		
		MATERIAL	COMMENTS:		
NEXT ASSY	USED ON	FINISH			
APPLICATION		DO NOT SCALE DRAWING			

TITLE:

SIZE	DWG. NO.	REV
A	Photodiode Bracket	

SCALE: 2:1	WEIGHT:	SHEET 1 OF 1

5 4 3 2 1

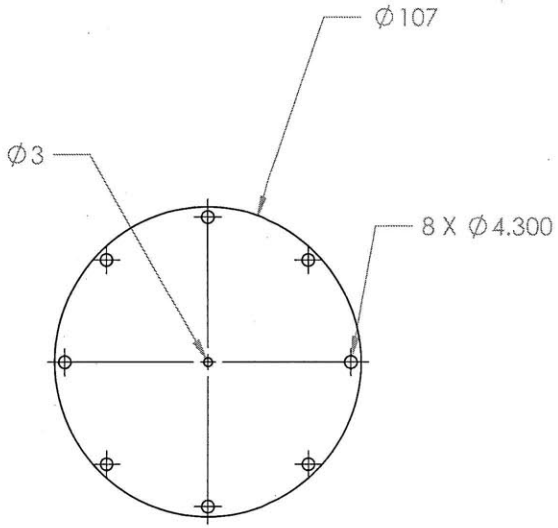

UNLESS OTHERWISE SPECIFIED: DIMENSIONS ARE IN MILLIMETERS SURFACE FINISH: TOLERANCES: LINEAR: ANGULAR:		FINISH:				DEBUR AND BREAK SHARP EDGES	DO NOT SCALE DRAWING / REVISION
	NAME	SIGNATURE	DATE				TITLE:
DRAWN							
CHK'D							
APPV'D							
MFG							
Q.A				MATERIAL:			DWG NO. Top Flexure / A4
				WEIGHT:			SCALE:1:2 / SHEET 1 OF 1

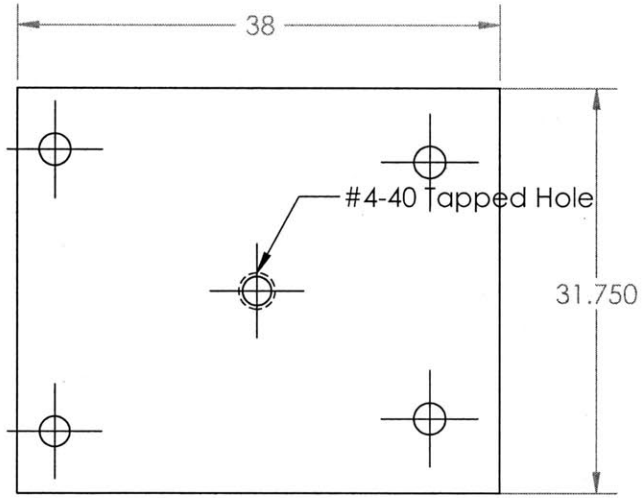

		UNLESS OTHERWISE SPECIFIED:		NAME	DATE
		DIMENSIONS ARE IN INCHES TOLERANCES: FRACTIONAL ± ANGULAR: MACH ± BEND ± TWO PLACE DECIMAL ± THREE PLACE DECIMAL ±	DRAWN		
			CHECKED		
			ENG APPR.		
			MFG APPR.		
		INTERPRET GEOMETRIC TOLERANCING PER:	Q.A.		
		MATERIAL	COMMENTS:		
NEXT ASSY	USED ON	FINISH			
APPLICATION		DO NOT SCALE DRAWING			

TITLE:

SIZE	DWG. NO.	REV
A	Top Plate	
SCALE: 2:1	WEIGHT:	SHEET 1 OF 1

5 4 3 2 1

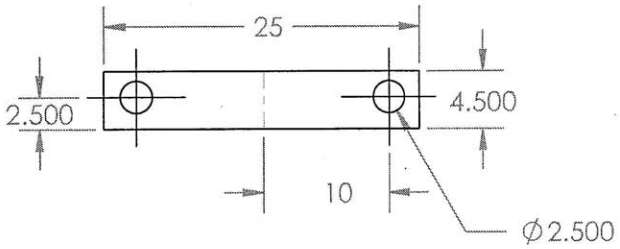

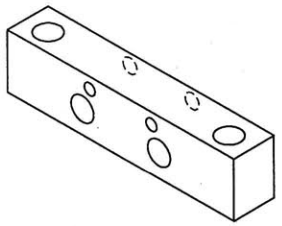

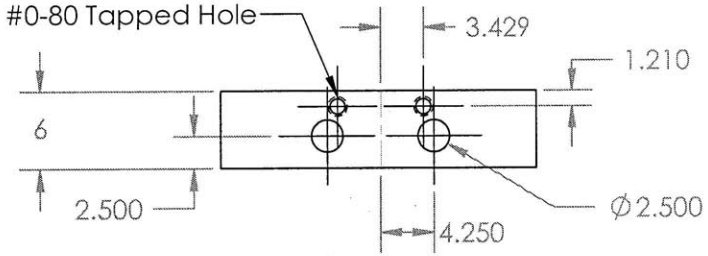

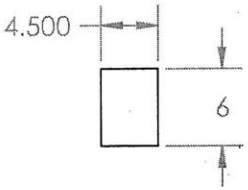

		UNLESS OTHERWISE SPECIFIED:		NAME	DATE
		DIMENSIONS ARE IN INCHES TOLERANCES: FRACTIONAL ± ANGULAR: MACH ± BEND ± TWO PLACE DECIMAL ± THREE PLACE DECIMAL ±	DRAWN		
			CHECKED		
			ENG APPR.		
			MFG APPR.		
		INTERPRET GEOMETRIC TOLERANCING PER:	Q.A.		
		MATERIAL	COMMENTS:		
NEXT ASSY	USED ON	FINISH			
APPLICATION		DO NOT SCALE DRAWING			

TITLE:

SIZE	DWG. NO.	REV
A	Top Side Support	
SCALE: 2:1	WEIGHT:	SHEET 1 OF 1

5 4 3 2 1

Appendix B

Vendors

This appendix provides the suppliers for the equipment used and purchased for this thesis

Analog Devices Inc.
ADI Sales Wilmington
831 Woburn St
Wilmington, MA 01887-4601
United States
TEL (800) 262-5645 TEL2 781-937-2384

Advanced Photonics Inc.
2925 Boardwalk
Ann Arbor, MI 48104
Main Phone: (734) 864-5600
Main Fax: (734) 998-3474

Coherent Inc.
5100 Patrick Henry Drive
Santa Clara, CA 95054 USA
Main Phone: 408-764-4000
Main Fax: 408-764-4800

Edmund Optics Inc.
101 East Gloucester Pike
Barrington, NJ 08007 USA
Phone: 1-856-573-6250
Toll-Free: 1-800-363-1992
Fax: 1-856-573-6295

Newport Corporation
1791 Deere Avenue
Irvine CA 92606
USA
Tel: (949)-863-3144
Fax: (949)-253-1680

PI (Physik Instrumente) L.P.
16 Albert St.
Auburn, MA 01501
Tel: +1 (508) 832 3456
Fax: +1 (508) 832 0506
Email: info@pi-usa.us

Silicon Lightwave Technology, Inc.
16 Technology Drive, Suite 168
Irvine, CA 92618
Ph: (949) 753-0421
Fx: (949) 753-8033
Email: info@slwti.com

Sunstone Circuits
13626 S. Freeman Road
Mulino, OR 97042
Phone: 503-829-9109
Fax: 503-829-6657
Email: support@sunstone.com

Thorlabs - Newton, New Jersey
435 Route 206 North
Newton, NJ 07860
Phone: 1-973-579-7227
Fax: 1-973-300-3600
Email: sales@thorlabs.com

Appendix C

Datasheet

This appendix provides the specification sheets for the equipment used and purchased for this thesis.

Low Cost, 80 MHz *FastFET* Op Amps

AD8033/AD8034

FEATURES

- FET input amplifier
  - 1 pA typical input bias current
- Very low cost
- High speed
  - 80 MHz, −3 dB bandwidth (G = +1)
  - 80 V/µs slew rate (G = +2)
- Low noise
  - 11 nV/√Hz (f = 100 kHz)
  - 0.7 fA/√Hz (f = 100 kHz)
- Wide supply voltage range: 5 V to 24 V
- Low offset voltage: 1 mV typical
- Single-supply and rail-to-rail output
- High common-mode rejection ratio: −100 dB
- Low power: 3.3 mA/amplifier typical supply current
- No phase reversal
- Small packaging: 8-lead SOIC, 8-lead SOT-23, and 5-lead SC70

APPLICATIONS

- Instrumentation
- Filters
- Level shifting
- Buffering

GENERAL DESCRIPTION

The AD8033/AD8034 *Fast*FET™ amplifiers are voltage feedback amplifiers with FET inputs, offering ease of use and excellent performance. The AD8033 is a single amplifier and the AD8034 is a dual amplifier. The AD8033/AD8034 *Fast*FET op amps in Analog Devices, Inc., proprietary XFCB process offer significant performance improvements over other low cost FET amps, such as low noise (11 nV/√Hz and 0.7 fA/√Hz) and high speed (80 MHz bandwidth and 80 V/µs slew rate).

With a wide supply voltage range from 5 V to 24 V and fully operational on a single supply, the AD8033/AD8034 amplifiers work in more applications than similarly priced FET input amplifiers. In addition, the AD8033/AD8034 have rail-to-rail outputs for added versatility.

Despite their low cost, the amplifiers provide excellent overall performance. They offer a high common-mode rejection of −100 dB, low input offset voltage of 2 mV maximum, and low noise of 11 nV/√Hz.

CONNECTION DIAGRAMS

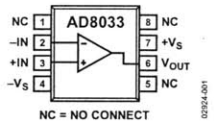

Figure 1. 8-Lead SOIC (R)

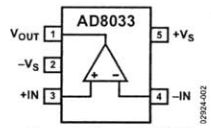

Figure 2. 5-Lead SC70 (KS)

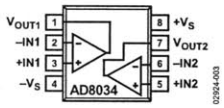

Figure 3. 8-Lead SOIC (R) and 8-Lead SOT-23 (RJ)

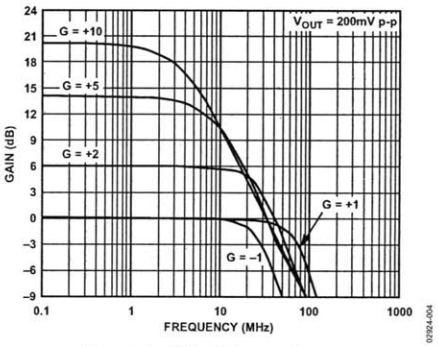

Figure 4. Small Signal Frequency Response

The AD8033/AD8034 amplifiers only draw 3.3 mA/amplifier of quiescent current while having the capability of delivering up to 40 mA of load current.

The AD8033 is available in a small package 8-lead SOIC and a small package 5-lead SC70. The AD8034 is also available in a small package 8-lead SOIC and a small package 8-lead SOT-23. They are rated to work over the industrial temperature range of −40°C to +85°C without a premium over commercial grade products.

Rev. D

One Technology Way, P.O. Box 9106, Norwood, MA 02062-9106, U.S.A.
Tel: 781.329.4700 www.analog.com
Fax: 781.461.3113

TABLE OF CONTENTS

REVISION HISTORY

9/08—Rev. C to Rev. D

Deleted Usable Input Range Parameter, Table 1 ... 3
Deleted Usable Input Range Parameter, Table 2 ... 4
Deleted Usable Input Range Parameter, Table 3 ... 5

4/08—Rev. B to Rev. C

Changes to Format ... Universal
Changes to Features and General Description ... 1
Changes to Figure 13 Caption and Figure 14 Caption ... 8
Changes to Figure 22 and Figure 23 ... 9
Changes to Figure 25 and Figure 28 ... 10
Changes to Input Capacitance Section ... 18
Changes to Active Filters Section ... 21
Changes to Outline Dimensions ... 23
Changes to Ordering Guide ... 24

2/03—Rev. A to Rev. B

Changes to Features ... 1
Changes to Connection Diagrams ... 1
Changes to Specifications ... 2
Changes to Absolute Maximum Ratings ... 4
Replaced TPC 31 ... 11
Changes to TPC 35 ... 11
Changes to Test Circuit 3 ... 12
Updated Outline Dimensions ... 19

8/02—Rev. 0 to Rev. A

Added AD8033 ... Universal
V_{OUT} = 2 V p-p Deleted from Default Conditions ... Universal
Added SOIC-8 (R) and SC70 (KS) ... 1
Edits to General Description Section ... 1
Changes to Specifications ... 2
New Figure 2 ... 5
Edits to Maximum Power Dissipation Section ... 5
Changes to Ordering Guide ... 5
Change to TPC 3 ... 6
Change to TPC 6 ... 6
Change to TPC 9 ... 7
New TPC 16 ... 8
New TPC 17 ... 8
New TPC 31 ... 11
New TPC 35 ... 11
New Test Circuit 9 ... 13
SC70 (KS) Package Added ... 19

SPECIFICATIONS

T_A = 25°C, V_S = ±5 V, R_L = 1 kΩ, gain = +2, unless otherwise noted.

Table 1.

Parameter	Conditions	Min	Typ	Max	Unit
DYNAMIC PERFORMANCE					
−3 dB Bandwidth	G = +1, V_{OUT} = 0.2 V p-p	65	80		MHz
	G = +2, V_{OUT} = 0.2 V p-p		30		MHz
	G = +2, V_{OUT} = 2 V p-p		21		MHz
Input Overdrive Recovery Time	−6 V to +6 V input		135		ns
Output Overdrive Recovery Time	−3 V to +3 V input, G = +2		135		ns
Slew Rate (25% to 75%)	G = +2, V_{OUT} = 4 V step	55	80		V/µs
Settling Time to 0.1%	G = +2, V_{OUT} = 2 V step		95		ns
	G = +2, V_{OUT} = 8 V step		225		ns
NOISE/HARMONIC PERFORMANCE					
Distortion	f_C = 1 MHz, V_{OUT} = 2 V p-p				
Second Harmonic	R_L = 500 Ω		−82		dBc
	R_L = 1 kΩ		−85		dBc
Third Harmonic	R_L = 500 Ω		−70		dBc
	R_L = 1 kΩ		−81		dBc
Crosstalk, Output-to-Output	f = 1 MHz, G = +2		−86		dB
Input Voltage Noise	f = 100 kHz		11		nV/√Hz
Input Current Noise	f = 100 kHz		0.7		fA/√Hz
DC PERFORMANCE					
Input Offset Voltage	V_{CM} = 0 V		1	2	mV
	T_{MIN} − T_{MAX}			3.5	mV
Input Offset Voltage Match				2.5	mV
Input Offset Voltage Drift			4	27	µV/°C
Input Bias Current			1.5	11	pA
	T_{MIN} − T_{MAX}		50		pA
Open-Loop Gain	V_{OUT} = ± 3 V	89	92		dB
INPUT CHARACTERISTICS					
Common-Mode Input Impedance			1000||2.3		GΩ||pF
Differential Input Impedance			1000||1.7		GΩ||pF
Input Common-Mode Voltage Range					
FET Input Range			−5.0 to +2.2		V
Common-Mode Rejection Ratio	V_{CM} = −3 V to +1.5 V	−89	−100		dB
OUTPUT CHARACTERISTICS					
Output Voltage Swing		±4.75	±4.95		V
Output Short-Circuit Current			40		mA
Capacitive Load Drive	30% overshoot, G = +1, V_{OUT} = 400 mV p-p		35		pF
POWER SUPPLY					
Operating Range		5		24	V
Quiescent Current per Amplifier			3.3	3.5	mA
Power Supply Rejection Ratio	V_S = ±2 V	−90	−100		dB

T_A = 25°C, V_S = 5 V, R_L = 1 kΩ, gain = +2, unless otherwise noted.

Table 2.

Parameter	Conditions	Min	Typ	Max	Unit
DYNAMIC PERFORMANCE					
−3 dB Bandwidth	G = +1, V_{OUT} = 0.2 V p-p	70	80		MHz
	G = +2, V_{OUT} = 0.2 V p-p		32		MHz
	G = +2, V_{OUT} = 2 V p-p		21		MHz
Input Overdrive Recovery Time	−3 V to +3 V input		180		ns
Output Overdrive Recovery Time	−1.5 V to +1.5 V input, G = +2		200		ns
Slew Rate (25% to 75%)	G = +2, V_{OUT} = 4 V step	55	70		V/µs
Settling Time to 0.1%	G = +2, V_{OUT} = 2 V step		100		ns
NOISE/HARMONIC PERFORMANCE					
Distortion	f_C = 1 MHz, V_{OUT} = 2 V p-p				
Second Harmonic	R_L = 500 Ω		−80		dBc
	R_L = 1 kΩ		−84		dBc
Third Harmonic	R_L = 500 Ω		−70		dBc
	R_L = 1 kΩ		−80		dBc
Crosstalk, Output to Output	f = 1 MHz, G = +2		−86		dB
Input Voltage Noise	f = 100 kHz		11		nV/√Hz
Input Current Noise	f = 100 kHz		0.7		fA/√Hz
DC PERFORMANCE					
Input Offset Voltage	V_{CM} = 0 V		1	2	mV
	T_{MIN} − T_{MAX}			3.5	mV
Input Offset Voltage Match				2.5	mV
Input Offset Voltage Drift			4	30	µV/°C
Input Bias Current			1	10	pA
	T_{MIN} − T_{MAX}		50		pA
Open-Loop Gain	V_{OUT} = 0 V to 3 V	87	92		dB
INPUT CHARACTERISTICS					
Common-Mode Input Impedance			1000‖2.3		GΩ‖pF
Differential Input Impedance			1000‖1.7		GΩ‖pF
Input Common-Mode Voltage Range					
FET Input Range			0 to 2.0		V
Common-Mode Rejection Ratio	V_{CM} = 1.0 V to 2.5 V	−80	−100		dB
OUTPUT CHARACTERISTICS					
Output Voltage Swing	R_L = 1 kΩ	0.16 to 4.83	0.04 to 4.95		V
Output Short-Circuit Current			30		mA
Capacitive Load Drive	30% overshoot, G = +1, V_{OUT} = 400 mV p-p		25		pF
POWER SUPPLY					
Operating Range		5		24	V
Quiescent Current per Amplifier			3.3	3.5	mA
Power Supply Rejection Ratio	V_S = ±1 V	−80	−100		dB

T_A = 25°C, V_S = ±12 V, R_L = 1 kΩ, gain = +2, unless otherwise noted.

Table 3.

Parameter	Conditions	Min	Typ	Max	Unit
DYNAMIC PERFORMANCE					
−3 dB Bandwidth	G = +1, V_{OUT} = 0.2 V p-p	65	80		MHz
	G = +2, V_{OUT} = 0.2 V p-p		30		MHz
	G = +2, V_{OUT} = 2 V p-p		21		MHz
Input Overdrive Recovery Time	−13 V to +13 V input		100		ns
Output Overdrive Recovery Time	−6.5 V to +6.5 V input, G = +2		100		ns
Slew Rate (25% to 75%)	G = +2, V_{OUT} = 4 V step	55	80		V/µs
Settling Time to 0.1%	G = +2, V_{OUT} = 2 V step		90		ns
	G = +2, V_{OUT} = 10 V step		225		ns
NOISE/HARMONIC PERFORMANCE					
Distortion	f_C = 1 MHz, V_{OUT} = 2 V p-p				
Second Harmonic	R_L = 500 Ω		−80		dBc
	R_L = 1 kΩ		−82		dBc
Third Harmonic	R_L = 500 Ω		−70		dBc
	R_L = 1 kΩ		−82		dBc
Crosstalk, Output to Output	f = 1 MHz, G = +2		−86		dB
Input Voltage Noise	f = 100 kHz		11		nV/√Hz
Input Current Noise	f = 100 kHz		0.7		fA/√Hz
DC PERFORMANCE					
Input Offset Voltage	V_{CM} = 0 V		1	2	mV
	T_{MIN} – T_{MAX}			3.5	mV
Input Offset Voltage Match				2.5	mV
Input Offset Voltage Drift			4	24	µV/°C
Input Bias Current			2	12	pA
	T_{MIN} – T_{MAX}		50		pA
Open-Loop Gain	V_{OUT} = ±8 V	88	96		dB
INPUT CHARACTERISTICS					
Common-Mode Input Impedance			1000‖2.3		GΩ‖pF
Differential Input Impedance			1000‖1.7		GΩ‖pF
Input Common-Mode Voltage Range					
FET Input Range			−12.0 to +9.0		V
Common-Mode Rejection Ratio	V_{CM} = ±5 V	−92	−100		dB
OUTPUT CHARACTERISTICS					
Output Voltage Swing		±11.52	±11.84		V
Output Short-Circuit Current			60		mA
Capacitive Load Drive	30% overshoot, G = +1		35		pF
POWER SUPPLY					
Operating Range		5		24	V
Quiescent Current per Amplifier			3.3	3.5	mA
Power Supply Rejection Ratio	V_S = ±2 V	−85	−100		dB

ABSOLUTE MAXIMUM RATINGS

Table 4.

Parameter	Rating
Supply Voltage	26.4 V
Power Dissipation	See Figure 5
Common-Mode Input Voltage	26.4 V
Differential Input Voltage	1.4 V
Storage Temperature Range	−65°C to +125°C
Operating Temperature Range	−40°C to +85°C
Lead Temperature (Soldering 10 sec)	300°C

Stresses above those listed under Absolute Maximum Ratings may cause permanent damage to the device. This is a stress rating only; functional operation of the device at these or any other conditions above those indicated in the operational section of this specification is not implied. Exposure to absolute maximum rating conditions for extended periods may affect device reliability.

MAXIMUM POWER DISSIPATION

The maximum safe power dissipation in the AD8033/AD8034 packages is limited by the associated rise in junction temperature (T_J) on the die. The plastic that encapsulates the die locally reaches the junction temperature. At approximately 150°C, which is the glass transition temperature, the plastic changes its properties. Even temporarily exceeding this temperature limit can change the stresses that the package exerts on the die, permanently shifting the parametric performance of the AD8033/AD8034. Exceeding a junction temperature of 175°C for an extended period can result in changes in silicon devices, potentially causing failure.

The still-air thermal properties of the package and PCB (θ_{JA}), ambient temperature (T_A), and the total power dissipated in the package (P_D) determine the junction temperature of the die. The junction temperature can be calculated as

$$T_J = T_A + (P_D \times \theta_{JA})$$

P_D is the sum of the quiescent power dissipation and the power dissipated in the package due to the load drive for all outputs. The quiescent power is the voltage between the supply pins (V_S) times the quiescent current (I_S). Assuming the load (R_L) is referenced to midsupply, the total drive power is $V_S/2 \times I_{OUT}$, some of which is dissipated in the package and some in the load ($V_{OUT} \times I_{OUT}$). The difference between the total drive power and the load power is the drive power dissipated in the package

$$P_D = \textit{Quiescent Power} + (\textit{Total Drive Power} - \textit{Load Power})$$

$$P_D = [V_S \times I_S] + [(V_S/2) \times (V_{OUT}/R_L)] - [V_{OUT}^2/R_L]$$

RMS output voltages should be considered. If R_L is referenced to $-V_S$, as in single-supply operation, the total drive power is $V_S \times I_{OUT}$.

If the rms signal levels are indeterminate, consider the worst case, when $V_{OUT} = V_S/4$ for R_L to midsupply

$$P_D = (V_S \times I_S) + (V_S/4)^2/R_L$$

In single-supply operation with R_L referenced to V_{S-}, worst case is $V_{OUT} = V_S/2$.

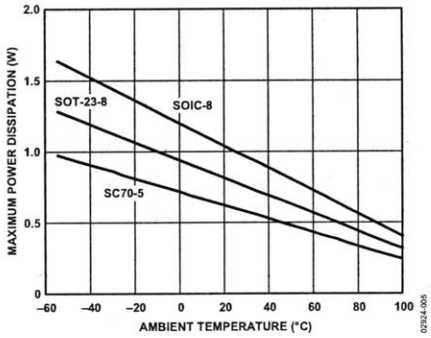

Figure 5. Maximum Power Dissipation vs. Ambient Temperature for a 4-Layer Board

Airflow increases heat dissipation, effectively reducing θ_{JA}. In addition, more metal directly in contact with the package leads from metal traces, through holes, ground, and power planes reduces the θ_{JA}. Care must be taken to minimize parasitic capacitances at the input leads of high speed op amps as discussed in the Layout, Grounding, and Bypassing Considerations section.

Figure 5 shows the maximum power dissipation in the package vs. the ambient temperature for the 8-lead SOIC (125°C/W), 5-lead SC70 (210°C/W), and 8-lead SOT-23 (160°C/W) packages on a JEDEC standard 4-layer board. θ_{JA} values are approximations.

OUTPUT SHORT CIRCUIT

Shorting the output to ground or drawing excessive current for the AD8033/AD8034 will likely cause catastrophic failure.

ESD CAUTION

ESD (electrostatic discharge) sensitive device. Charged devices and circuit boards can discharge without detection. Although this product features patented or proprietary protection circuitry, damage may occur on devices subjected to high energy ESD. Therefore, proper ESD precautions should be taken to avoid performance degradation or loss of functionality.

TYPICAL PERFORMANCE CHARACTERISTICS

Default conditions: V_S = ±5 V, C_L = 5 pF, R_L = 1 kΩ, T_A = 25°C.

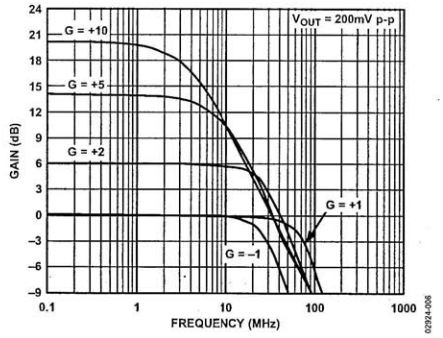

Figure 6. Small Signal Frequency Response for Various Gains

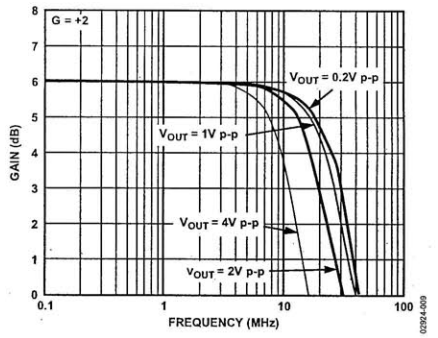

Figure 9. Frequency Response for Various Output Amplitudes (See Figure 45)

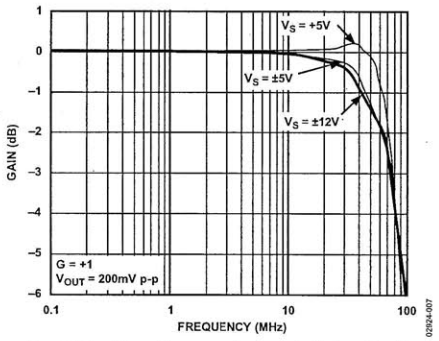

Figure 7. Small Signal Frequency Response for Various Supplies (See Figure 44)

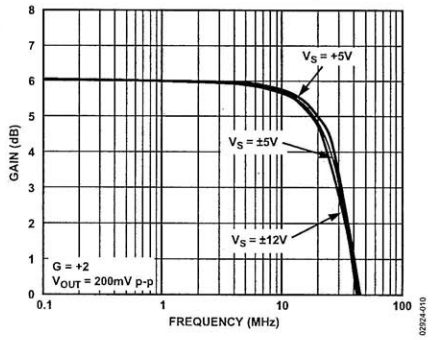

Figure 10. Small Signal Frequency Response for Various Supplies (See Figure 45)

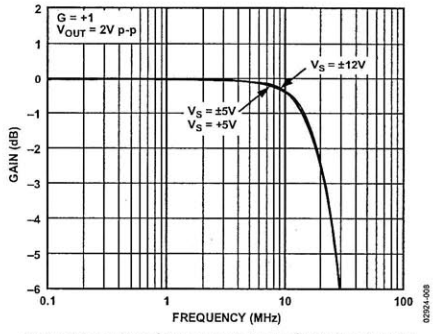

Figure 8. Large Signal Frequency Response for Various Supplies (See Figure 44)

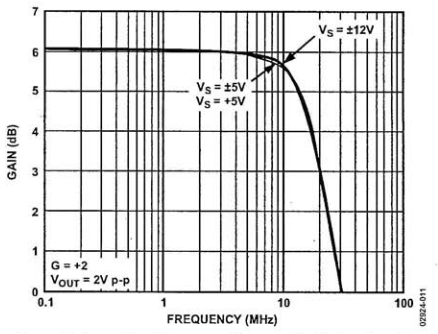

Figure 11. Large Signal Frequency Response for Various Supplies (See Figure 45)

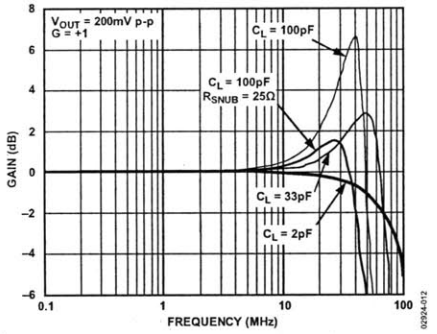

Figure 12. Small Signal Frequency Response for Various C_L (See Figure 44)

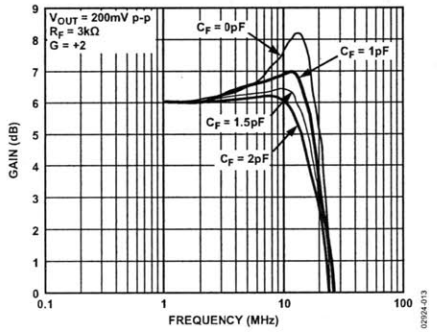

Figure 13. Small Signal Frequency Response for Various C_F (See Figure 45)

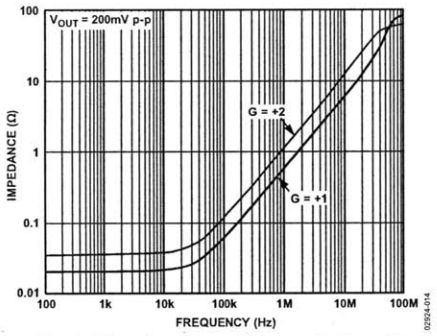

Figure 14. Output Impedance vs. Frequency (See Figure 47)

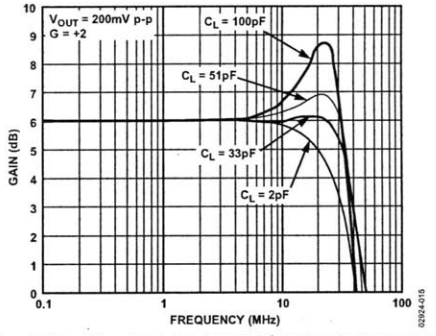

Figure 15. Small Signal Frequency Response for Various C_L (See Figure 45)

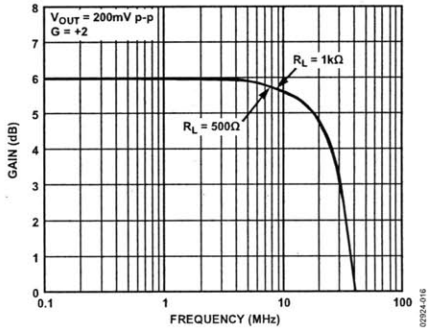

Figure 16. Small Signal Frequency Response for Various R_L (See Figure 45)

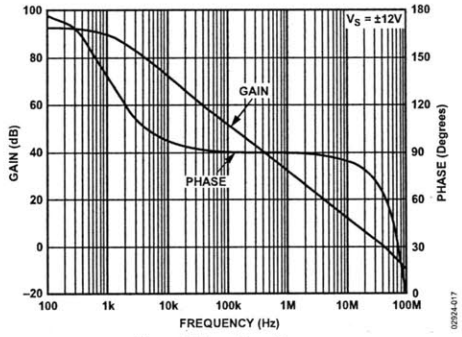

Figure 17. Open-Loop Response

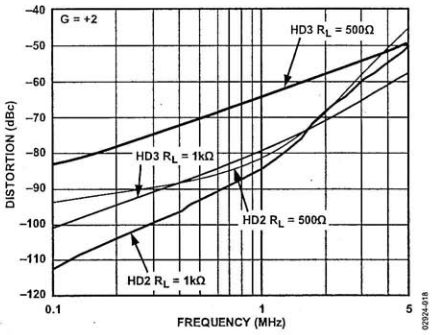

Figure 18. Harmonic Distortion vs. Frequency for Various Loads (See Figure 45)

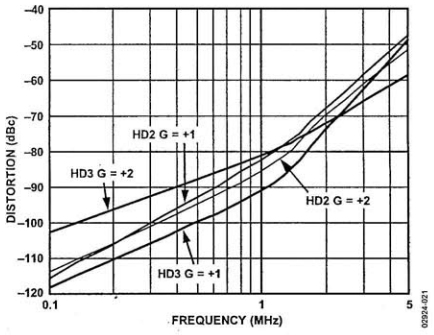

Figure 21. Harmonic Distortion vs. Frequency for Various Gains

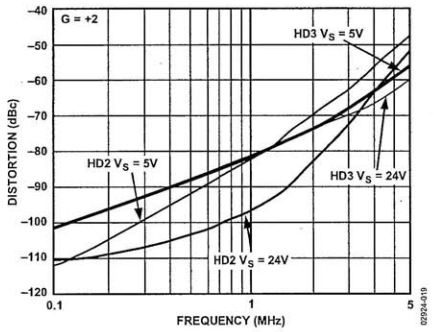

Figure 19. Harmonic Distortion vs. Frequency for Various Supply Voltages (See Figure 45)

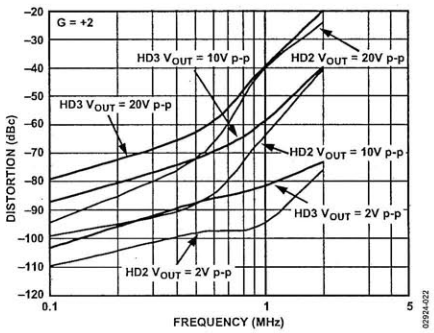

Figure 22. Harmonic Distortion vs. Frequency for Various Amplitudes (See Figure 45), V_S = 24 V

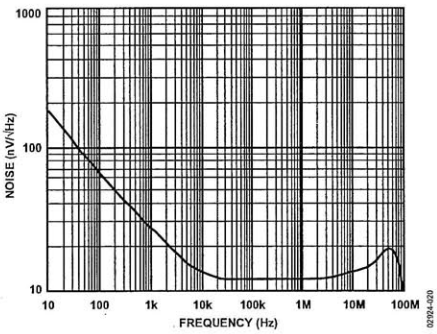

Figure 20. Voltage Noise vs. Frequency

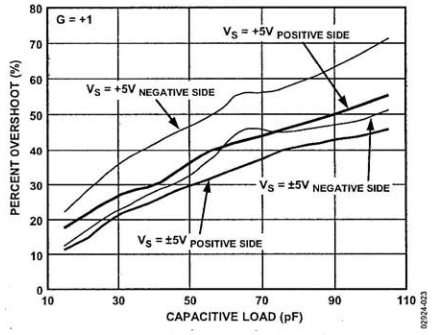

Figure 23. Percent Overshoot vs. Capacitive Load (See Figure 44)

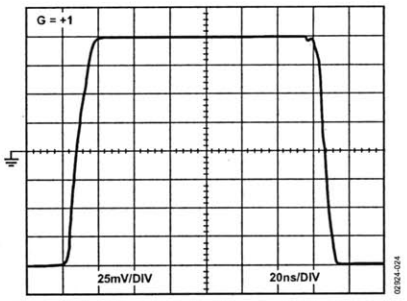

Figure 24. Small Signal Transient Response 5 V (See Figure 44)

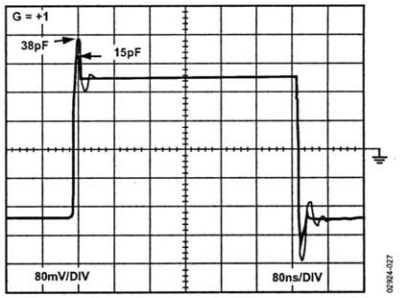

Figure 27. Small Signal Transient Response ±5 V (See Figure 44)

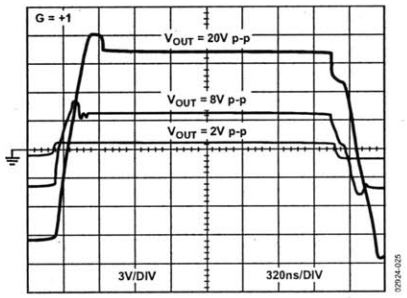

Figure 25. Large Signal Transient Response (See Figure 44)

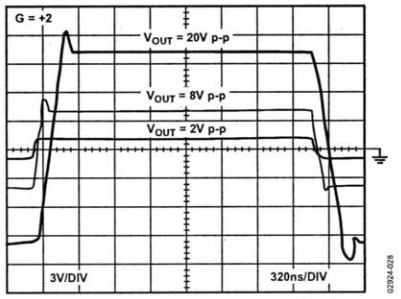

Figure 28. Large Signal Transient Response (See Figure 45)

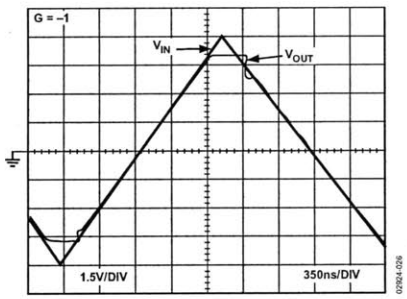

Figure 26. Output Overdrive Recovery (See Figure 46)

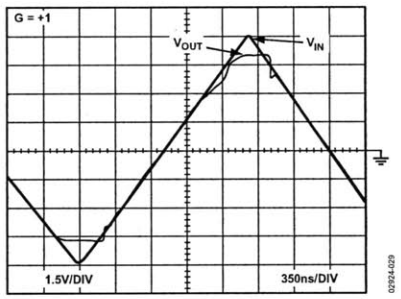

Figure 29. Input Overdrive Recovery (See Figure 44)

10 MHz, 20 V/µs, G = 1, 10, 100, 1000 *i*CMOS Programmable Gain Instrumentation Amplifier

AD8253

FEATURES

Small package: 10-lead MSOP
Programmable gains: 1, 10, 100, 1000
Digital or pin-programmable gain setting
Wide supply: ±5 V to ±15 V
Excellent dc performance
- **High CMRR: 100 dB (minimum), G = 100**
- **Low gain drift: 10 ppm/°C (maximum)**
- **Low offset drift: 1.2 µV/°C (maximum), G = 1000**

Excellent ac performance
- **Fast settling time: 780 ns to 0.001% (maximum)**
- **High slew rate: 20 V/µs (minimum)**
- **Low distortion: −110 dB THD at 1 kHz,10 V swing**
- **High CMRR over frequency: 100 dB to 20 kHz (minimum)**
- **Low noise: 10 nV/√Hz, G = 1000 (maximum)**
- **Low power: 4 mA**

APPLICATIONS

Data acquisition
Biomedical analysis
Test and measurement

GENERAL DESCRIPTION

The AD8253 is an instrumentation amplifier with digitally programmable gains that has gigaohm (GΩ) input impedance, low output noise, and low distortion, making it suitable for interfacing with sensors and driving high sample rate analog-to-digital converters (ADCs).

It has a high bandwidth of 10 MHz, low THD of −110 dB, and fast settling time of 780 ns (maximum) to 0.001%. Offset drift and gain drift are guaranteed to 1.2 µV/°C and 10 ppm/°C, respectively, for G = 1000. In addition to its wide input common voltage range, it boasts a high common-mode rejection of 100 dB at G = 1000 from dc to 20 kHz. The combination of precision dc performance coupled with high speed capabilities makes the AD8253 an excellent candidate for data acquisition. Furthermore, this monolithic solution simplifies design and manufacturing and boosts performance of instrumentation by maintaining a tight match of internal resistors and amplifiers.

The AD8253 user interface consists of a parallel port that allows users to set the gain in one of two different ways (see Figure 1 for the functional block diagram). A 2-bit word sent via a bus can be latched using the $\overline{WR}$ input. An alternative is to use transparent gain mode, where the state of logic levels at the gain port determines the gain.

FUNCTIONAL BLOCK DIAGRAM

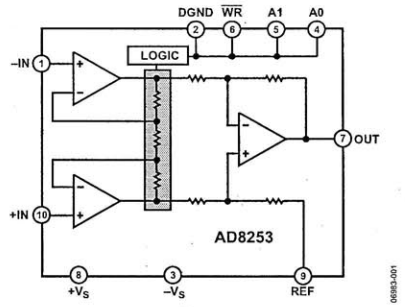

Figure 1.

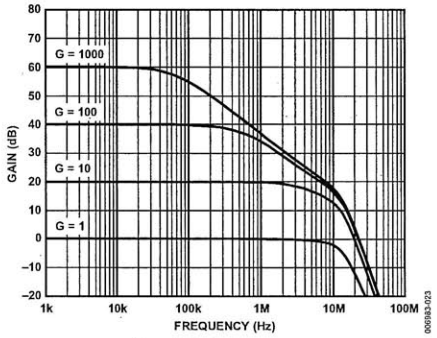

Figure 2. Gain vs. Frequency

Table 1. Instrumentation Amplifiers by Category

General Purpose	Zero Drift	Mil Grade	Low Power	High Speed PGA
AD8220[1]	AD8231[1]	AD620	AD627[1]	AD8250
AD8221	AD8553[1]	AD621	AD623[1]	AD8251
AD8222	AD8555[1]	AD524	AD8223[1]	AD8253
AD8224[1]	AD8556[1]	AD526		
AD8228	AD8557[1]	AD624		

[1] Rail-to-rail output.

The AD8253 is available in a 10-lead MSOP package and is specified over the −40°C to +85°C temperature range, making it an excellent solution for applications where size and packing density are important considerations.

Rev. A

One Technology Way, P.O. Box 9106, Norwood, MA 02062-9106, U.S.A.
Tel: 781.329.4700 www.analog.com
Fax: 781.461.3113

TABLE OF CONTENTS

REVISION HISTORY

8/08—Rev. 0 to Rev. A
Changes to Ordering Guide ... 23

7/08—Revision 0: Initial Version

SPECIFICATIONS

$+V_S$ = +15 V, $-V_S$ = −15 V, V_{REF} = 0 V @ T_A = 25°C, G = 1, R_L = 2 kΩ, unless otherwise noted.

Table 2.

Parameter	Conditions	Min	Typ	Max	Unit
COMMON-MODE REJECTION RATIO (CMRR)					
CMRR to 60 Hz with 1 kΩ Source Imbalance	+IN = −IN = −10 V to +10 V				
G = 1		80	100		dB
G = 10		96	120		dB
G = 100		100	120		dB
G = 1000		100	120		dB
CMRR to 20 kHz[1]	+IN = −IN = −10 V to +10 V				
G = 1		80			dB
G = 10		96			dB
G = 100		100			dB
G = 1000		100			dB
NOISE					
Voltage Noise, 1 kHz, RTI					
G = 1				45	nV/√Hz
G = 10				12	nV/√Hz
G = 100				11	nV/√Hz
G = 1000				10	nV/√Hz
0.1 Hz to 10 Hz, RTI					
G = 1				2.5	µV p-p
G = 10				1	µV p-p
G = 100				0.5	µV p-p
G = 1000				0.5	µV p-p
Current Noise, 1 kHz			5		pA/√Hz
Current Noise, 0.1 Hz to 10 Hz			60		pA p-p
VOLTAGE OFFSET					
Offset RTI V_{OS}	G = 1, 10, 100, 1000			±150 + 900/G	µV
Over Temperature	T = −40°C to +85°C			±210 + 900/G	µV
Average TC	T = −40°C to +85°C			±1.2 + 5/G	µV/°C
Offset Referred to the Input vs. Supply (PSR)	V_S = ±5 V to ±15 V			±5 + 25/G	µV/V
INPUT CURRENT					
Input Bias Current			5	50	nA
Over Temperature[2]	T = −40°C to +85°C	40		60	nA
Average TC	T = −40°C to +85°C			400	pA/°C
Input Offset Current			5	40	nA
Over Temperature	T = −40°C to +85°C			40	nA
Average TC	T = −40°C to +85°C			160	pA/°C
DYNAMIC RESPONSE					
Small-Signal −3 dB Bandwidth					
G = 1		10			MHz
G = 10		4			MHz
G = 100		550			kHz
G = 1000		60			kHz
Settling Time 0.01%	ΔOUT = 10 V step				
G = 1				700	ns
G = 10				680	ns
G = 100				1.5	µs
G = 1000				14	µs

Parameter	Conditions	Min	Typ	Max	Unit
Settling Time 0.001%	ΔOUT = 10 V step				
G = 1				780	ns
G = 10				880	ns
G =100				1.8	µs
G = 1000				1.8	µs
Slew Rate					
G = 1		20			V/µs
G = 10		20			V/µs
G = 100		12			V/µs
G = 1000		2			V/µs
Total Harmonic Distortion + Noise	f = 1 kHz, R_L = 10 kΩ, ±10 V, G = 1, 10 Hz to 22 kHz band-pass filter		−110		dB
GAIN					
Gain Range	G = 1, 10, 100, 1000	1		1000	V/V
Gain Error	OUT = ±10 V				
G = 1				0.03	%
G = 10, 100, 1000				0.04	%
Gain Nonlinearity	OUT = −10 V to +10 V				
G = 1	R_L = 10 kΩ, 2 kΩ, 600 Ω			5	ppm
G = 10	R_L = 10 kΩ, 2 kΩ, 600 Ω			3	ppm
G = 100	R_L = 10 kΩ, 2 kΩ, 600 Ω			18	ppm
G = 1000	R_L = 10 kΩ, 2 kΩ, 600 Ω			110	ppm
Gain vs. Temperature	All gains		3	10	ppm/°C
INPUT					
Input Impedance					
Differential			4‖1.25		GΩ‖pF
Common Mode			1‖5		GΩ‖pF
Input Operating Voltage Range	V_S = ±5 V to ±15 V	$-V_S$ + 1		$+V_S$ − 1.5	V
Over Temperature[3]	T = −40°C to +85°C	$-V_S$ + 1.2		$+V_S$ − 1.7	V
OUTPUT					
Output Swing		−13.7		+13.6	V
Over Temperature[4]	T = −40°C to +85°C	−13.7		+13.6	V
Short-Circuit Current			37		mA
REFERENCE INPUT					
R_{IN}			20		kΩ
I_{IN}	+IN, −IN, REF = 0			1	µA
Voltage Range		$-V_S$		$+V_S$	V
Gain to Output			1 ± 0.0001		V/V
DIGITAL LOGIC					
Digital Ground Voltage, DGND	Referred to GND	$-V_S$ + 4.25	0	$+V_S$ − 2.7	V
Digital Input Voltage Low	Referred to GND	DGND		1.2	V
Digital Input Voltage High	Referred to GND	1.5		$+V_S$	V
Digital Input Current			1		µA
Gain Switching Time[5]				325	ns
t_{SU}	See Figure 3 timing diagram	15			ns
t_{HD}		30			ns
$t_{\overline{WR}\text{-LOW}}$		20			ns
$t_{\overline{WR}\text{-HIGH}}$		15			ns

Parameter	Conditions	Min	Typ	Max	Unit
POWER SUPPLY					
Operating Range		±5		±15	V
Quiescent Current, $+I_S$			4.6	5.3	mA
Quiescent Current, $-I_S$			4.5	5.3	mA
Over Temperature	T = −40°C to +85°C			6	mA
TEMPERATURE RANGE					
Specified Performance		−40		+85	°C

[1] See Figure 20 for CMRR vs. frequency for more information on typical performance over frequency.
[2] Input bias current over temperature: minimum at hot and maximum at cold.
[3] See Figure 30 for input voltage limit vs. supply voltage and temperature.
[4] See Figure 32, Figure 33, and Figure 34 for output voltage swing vs. supply voltage and temperature for various loads.
[5] Add time for the output to slew and settle to calculate the total time for a gain change.

TIMING DIAGRAM

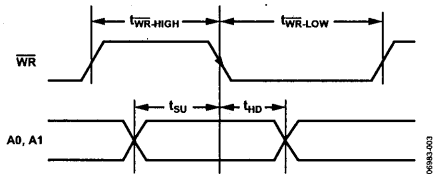

Figure 3. Timing Diagram for Latched Gain Mode (See the Timing for Latched Gain Mode Section)

ABSOLUTE MAXIMUM RATINGS

Table 3.

Parameter	Rating
Supply Voltage	±17 V
Power Dissipation	See Figure 4
Output Short-Circuit Current	Indefinite[1]
Common-Mode Input Voltage	$\pm V_S$
Differential Input Voltage	$\pm V_S$
Digital Logic Inputs	$\pm V_S$
Storage Temperature Range	−65°C to +125°C
Operating Temperature Range[2]	−40°C to +85°C
Lead Temperature (Soldering 10 sec)	300°C
Junction Temperature	140°C
θ_{JA} (4-Layer JEDEC Standard Board)	112°C/W
Package Glass Transition Temperature	140°C

[1] Assumes the load is referenced to midsupply.
[2] Temperature for specified performance is −40°C to +85°C. For performance to +125°C, see the Typical Performance Characteristics section.

Stresses above those listed under Absolute Maximum Ratings may cause permanent damage to the device. This is a stress rating only; functional operation of the device at these or any other conditions above those indicated in the operational section of this specification is not implied. Exposure to absolute maximum rating conditions for extended periods may affect device reliability.

MAXIMUM POWER DISSIPATION

The maximum safe power dissipation in the AD8253 package is limited by the associated rise in junction temperature (T_J) on the die. The plastic encapsulating the die locally reaches the junction temperature. At approximately 140°C, which is the glass transition temperature, the plastic changes its properties. Even temporarily exceeding this temperature limit can change the stresses that the package exerts on the die, permanently shifting the parametric performance of the AD8253. Exceeding a junction temperature of 140°C for an extended period can result in changes in silicon devices, potentially causing failure.

The still-air thermal properties of the package and PCB (θ_{JA}), the ambient temperature (T_A), and the total power dissipated in the package (P_D) determine the junction temperature of the die. The junction temperature is calculated as

$$T_J = T_A + (P_D \times \theta_{JA})$$

The power dissipated in the package (P_D) is the sum of the quiescent power dissipation and the power dissipated in the package due to the load drive for all outputs. The quiescent power is the voltage between the supply pins (V_S) times the quiescent current (I_S). Assuming the load (R_L) is referenced to midsupply, the total drive power is $V_S/2 \times I_{OUT}$, some of which is dissipated in the package and some of which is dissipated in the load ($V_{OUT} \times I_{OUT}$).

The difference between the total drive power and the load power is the drive power dissipated in the package.

$$P_D = \textit{Quiescent Power} + (\textit{Total Drive Power} - \textit{Load Power})$$

$$P_D = (V_S \times I_S) + \left(\frac{V_S}{2} \times \frac{V_{OUT}}{R_L}\right) - \frac{V_{OUT}^2}{R_L}$$

In single-supply operation with R_L referenced to $-V_S$, the worst case is $V_{OUT} = V_S/2$.

Airflow increases heat dissipation, effectively reducing θ_{JA}. In addition, more metal directly in contact with the package leads from metal traces through holes, ground, and power planes reduces the θ_{JA}.

Figure 4 shows the maximum safe power dissipation in the package vs. the ambient temperature on a 4-layer JEDEC standard board.

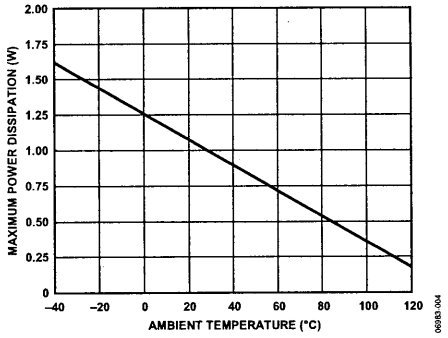

Figure 4. Maximum Power Dissipation vs. Ambient Temperature

ESD CAUTION

ESD (electrostatic discharge) sensitive device. Charged devices and circuit boards can discharge without detection. Although this product features patented or proprietary protection circuitry, damage may occur on devices subjected to high energy ESD. Therefore, proper ESD precautions should be taken to avoid performance degradation or loss of functionality.

PIN CONFIGURATION AND FUNCTION DESCRIPTIONS

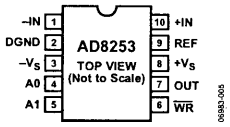

Figure 5. 10-Lead MSOP (RM-10) Pin Configuration

Table 4. Pin Function Descriptions

Pin No.	Mnemonic	Description
1	–IN	Inverting Input Terminal. True differential input.
2	DGND	Digital Ground.
3	$-V_S$	Negative Supply Terminal.
4	A0	Gain Setting Pin (LSB).
5	A1	Gain Setting Pin (MSB).
6	$\overline{WR}$	Write Enable.
7	OUT	Output Terminal.
8	$+V_S$	Positive Supply Terminal.
9	REF	Reference Voltage Terminal.
10	+IN	Noninverting Input Terminal. True differential input.

TYPICAL PERFORMANCE CHARACTERISTICS

T_A @ 25°C, $+V_S$ = +15 V, $-V_S$ = −15 V, R_L = 10 kΩ, unless otherwise noted.

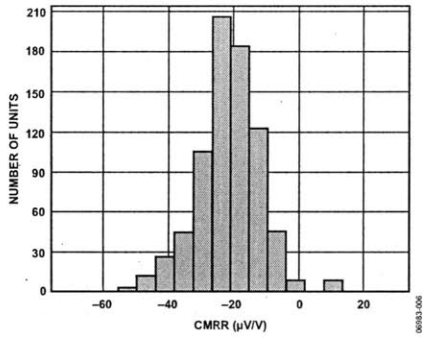

Figure 6. Typical Distribution of CMRR, G = 1

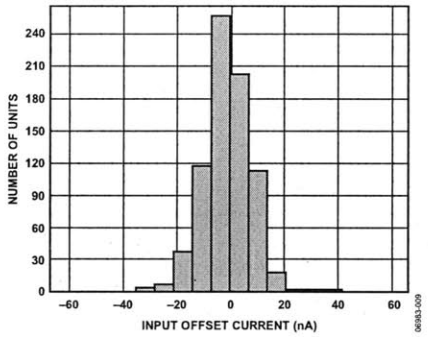

Figure 9. Typical Distribution of Input Offset Current

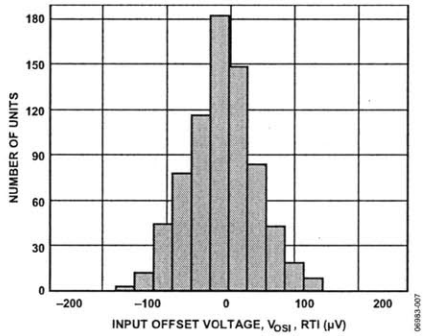

Figure 7. Typical Distribution of Offset Voltage, V_{OSI}

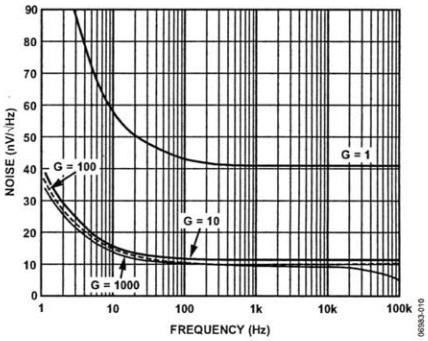

Figure 10. Voltage Spectral Density Noise vs. Frequency

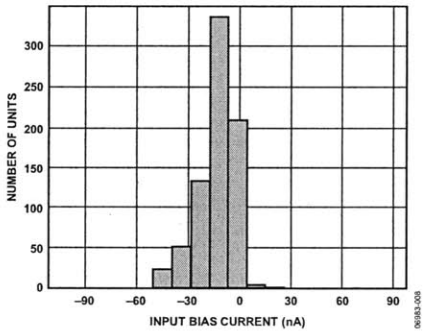

Figure 8. Typical Distribution of Input Bias Current

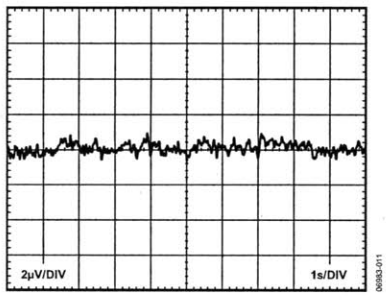

Figure 11. 0.1 Hz to 10 Hz RTI Voltage Noise, G = 1

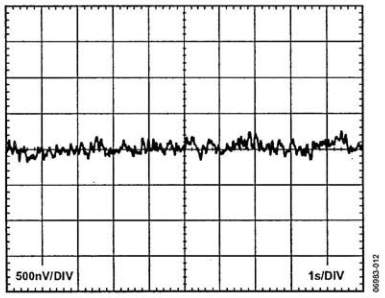

Figure 12. 0.1 Hz to 10 Hz RTI Voltage Noise, G = 1000

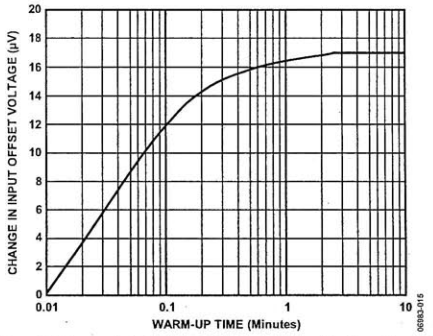

Figure 15. Change in Input Offset Voltage vs. Warm-Up Time, G = 1000

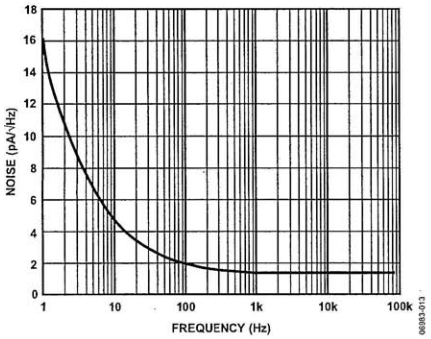

Figure 13. Current Noise Spectral Density vs. Frequency

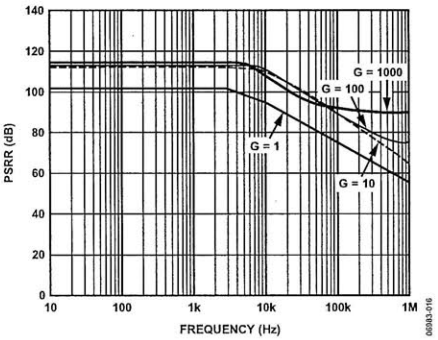

Figure 16. Positive PSRR vs. Frequency, RTI

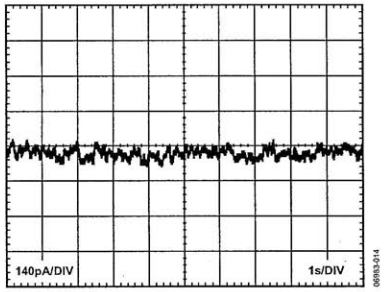

Figure 14. 0.1 Hz to 10 Hz Current Noise

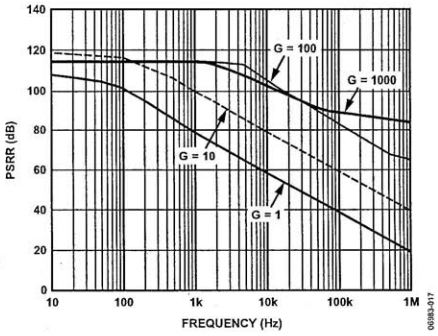

Figure 17. Negative PSRR vs. Frequency, RTI

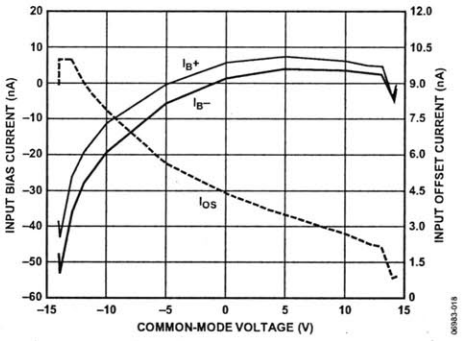

Figure 18. Input Bias Current and Offset Current vs. Common-Mode Voltage

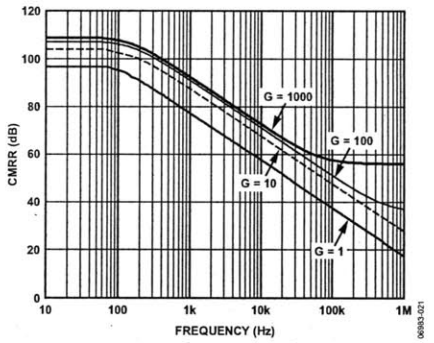

Figure 21. CMRR vs. Frequency, 1 kΩ Source Imbalance

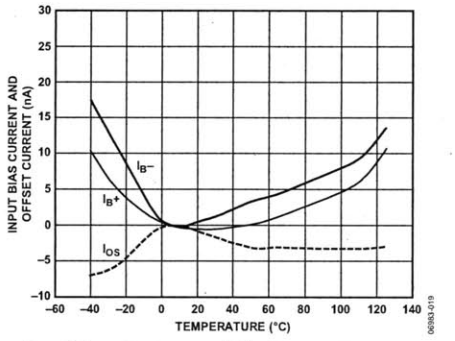

Figure 19. Input Bias Current and Offset Current vs. Temperature

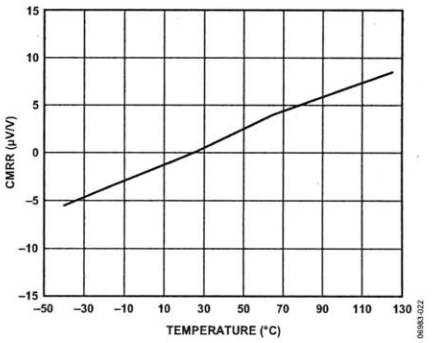

Figure 22. CMRR vs. Temperature, G = 1

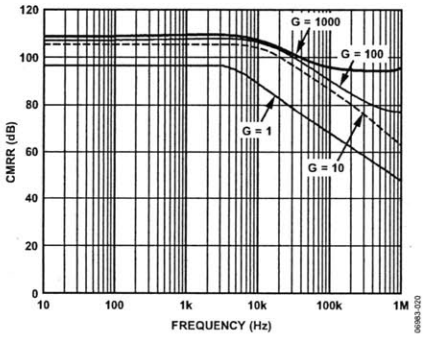

Figure 20. CMRR vs. Frequency

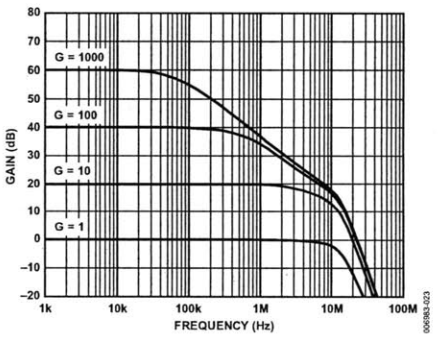

Figure 23. Gain vs. Frequency

API
Advanced Photonix, Inc.

Red Enhanced Quad Cell Silicon Photodiode

SD 085-23-21-021

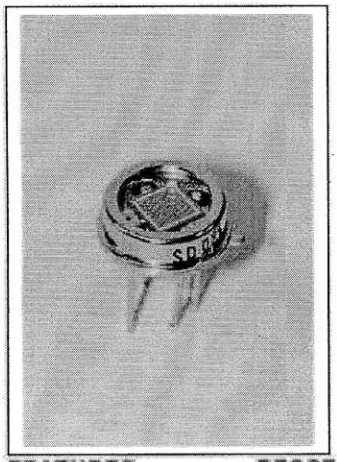

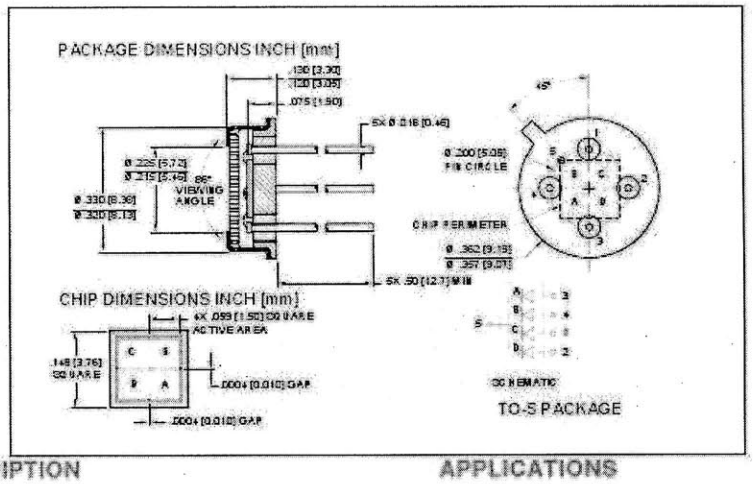

FEATURES

- Low noise
- Red enhanced
- High shunt resistance
- High response

DESCRIPTION

The **SD 085-23-21-021** is a red enhanced quad-cell silicon photodiode used for nulling, centering, or measuring small positional changes packaged in a hermetic TO-5 metal package.

APPLICATIONS

- Emitter Alignment
- Position sensing
- Medical and Industrial

ABSOLUTE MAXIMUM RATING (TA= 23°C UNLESS OTHERWISE NOTED

SYMBOL	PARAMETER	MIN	MAX	UNITS
V_{BR}	Reverse Voltage		50	V
T_{STG}	Storage Temperature	-55	+150	°C
T_O	Operating Temperature	-40	+125	°C
T_S	Soldering Temperature*		+240	°C

* 1/16 inch from case for 3 seconds max.

SPECTRAL RESPONSE

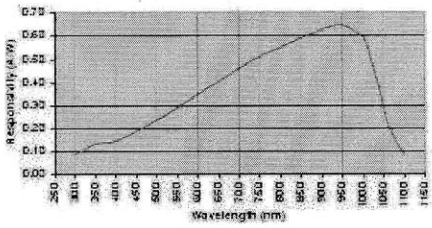

ELECTRO-OPTICAL CHARACTERISTICS RATING (TA= 23°C UNLESS OTHERWISE NOTED

SYMBOL	CHARACTERISTIC	TEST CONDITIONS	MIN	TYP	MAX	UNITS
I_D	Dark Current	V_R = 5 V		0.6	3.5	nA
R_{SH}	Shunt Resistance	V_R = 10 mV	350			MΩ
C_J	Junction Capacitance	V_R = 0 V, f = 1 MHz		45		pF
		V_R = 5 V, f = 1 MHz		9		
λrange	Spectral Application Range	Spot Scan	350		1100	nm
R	Responsivity	λ = 633nm, V_R = 0 V	0.32	0.36		A/W
		λ = 900nm, V_R = 0 V	0.50	0.55		
V_{BR}	Breakdown Voltage	I = 10 μA		50		V
NEP	Noise Equivalent Power	V_R = 0V @ λ = 950nm		2.5×10^{-13}		W/√Hz
t_r	Response Time**	RL = 50 Ω, V_R = 0 V		190		nS
		RL = 50 Ω, V_R = 10 V		13		

**Response time of 10% to 90% is specified at 660nm wavelength light.

Advanced Photonix Inc. 1240 Avenida Acaso, Camarillo CA 93012 • Phone (805) 987-0146 • Fax (805) 484-9935 • www.advancedphotonix.com

Bibliography

[1] Digital Instruments. Scanning Probe Microscopy Training Notebook, Version 3.0, 2000.

[2] Abramovitch Daniel Y. Andersson Sean B. Pao Lucy Y. Shitter Georg. A Tutorial on the Mechanisms, Dynamics, and Control of Atomic Force Microscopes. In Proceedings of American Controls Conference. June, 2007.

[3] Shilpiekandula Vijay. Design Methodology. Ph.D. Thesis, Massachusetts Institute of Technology, Cambridge, MA, 2009.

[4] Prater Craig, Su Chanmin, Phan Nghi, Markakis J.M., Cusworth Craig, Shi Jian, Kindt J.H., Nagle S.F., Fan Wenjun. Fast Scanning APM and Method of Operating Same, 2009. U.S. Patent No. 2009/0032706 A1.

[5] Hwang Ing-Shouh, Hung Shao-Kang, Fu Li-Chen, Lin Ming-Yen. Beam Tracking System for Scanning-Probe Type Atomic Force Microscope, 2007. U.S. Patent No. 7249494 B2.

[6] Nabil M. Amer, Gerbard Meyer. Atomic Force Microscopy, 1992. U.S. Patent No. 5144833.

[7] Jonathan B. Hopkins. 2.994 Flexure lecture notes. Lecture 2, slide 32, 2010.

[8] Silicon Lightwave, Inc. 16 Technology Drive, Suite 168 Irvine, CA 92618, http://www.slwti.com/, 2010.

[9] Graeme Jerald G. Photodiode Amplifiers : op amp solutions. Boston, Massachusetts. McGraw Hill, 1996.

[10] Advanced Photonix, Inc. 2925 Boardwalk Ann Arbor, MI 48104, http://www.advancedphotonix.com/, 2010.

[11] Anfatec Instruments AG. Anfatec SPM Controller Manual. Melanchthonstr. 28 08606 Oelsnitz (V), Germany, 2009.

[12] Automation Creations, Inc. 2020 Kraft Drive, Suite 3000 Blacksburg, VA 24060, http://www.matweb.com/, 2010.

[13] Coherent Inc. 5100 Patrick Henry Drive, Santa Clara, CA 95054, http://www.coherent.com/, 2010.

[14] Ohler Ben, Force Resolution in Force Spectroscopy Experiments: Thermal Noise and the Effect of Measurement Bandwidth. Veeco Instruments, 2007.